

Au Atomic Wires on Silicon: Spin Order and Phase Transitions in Low-Dimensional Systems



Christian Braun
The Department of Physics
Paderborn University

A dissertation submitted for the degree of
Doctor rerum naturalium (Dr. rer. nat.)

Paderborn, Germany
February 2021

© 2021 – Christian Braun

This work is licensed under the Creative Commons BY-NC-ND 4.0 International License.

Promotionskommission

Vorsitzender: Prof. Dr. Jörg Lindner
(Universität Paderborn)

Erstgutachter: Prof. Dr. Wolf Gero Schmidt
(Universität Paderborn)

Zweitgutachter: Prof. Dr. Simone Sanna
(Universität Gießen)

Vertreter des Mittelbaus: Dr. Matthias Reichelt
(Universität Paderborn)

Diese Dissertation ist meinen Eltern Maria und Eduard gewidmet, die für die bestmögliche Bildung sorgten und mich stets ermutigt und unterstützt haben.

Acknowledgements

I would like to begin this dissertation by bringing recognition and gratitude to those who contributed significantly to this work, both directly and indirectly. First and foremost, I would like to thank God for giving me a personal relationship with Him through the sacrifice of Jesus Christ. Nothing is more precious to me and nothing more encouraging than to know that I am loved by Him. It has always been my understanding that the laws of nature we seek to understand have an order because God has given them that order.

My deepest gratitude goes to my supervisor Prof. Dr. Wolf Gero Schmidt, who made this work possible in the first place. You were never short of encouragement and gave my research a little push in the right direction whenever a push was needed. I am especially grateful that you provided me with all the resources necessary to carry out the research.

I would like to acknowledge Dr. Uwe Gerstmann for his support and the fruitful discussions we had. Your deep understanding of computational material science greatly helped me plan and carry out the calculations during my time as a PhD candidate.

This dissertation would have had considerably more rough edges if Dr. Agnieszka Kozub had not helped to round them off. Thank you for the dozens of hours of proofreading and the many pieces of advice that were a great help to me.

Another thanks goes to Prof. Dr. Simone Sanna, who contributed significantly to my scientific education over the past decade. Even though our paths have parted to some extent due to your appointment at the University of Giessen in 2017, I am grateful for the ongoing fruitful collaboration and the resulting scientific work.

Moreover, I am grateful for the support of my colleagues Sergej Neufeld, Isaac Azahel Ruiz Alvarado, Adriana Bocchini, Maximilian Kulke, Sabuhi Badalov, Dr. Hazem Aldahak, and Dr. Timur Biktagirov. Not only were you an enrichment to our regular lunch breaks, but you were also always willing to answer my questions and discuss the topics of my research. I would also like to thank our secretary Simone Lange, who is always ready to lend a helping hand when someone needs it.

Getting through my doctorate required more than academic support, and I have many friends who have provided a welcome distraction from work and have enriched my life. Though there are many to name, I would like to especially mention Jonas Esau, Tobias Hamm, Richard Huck, and Tobias Tews. Our regular meetings on Tuesday evenings and your supportive prayers have been very empowering to me.

My deepest thanks go to my parents Maria and Eduard Braun. For the sake of your children, you decided to leave behind everything you had built in order to provide a better future for my sister and me. This dissertation would not have been possible without your devotion, love, and constant support.

Last but not least, I would like to thank my beloved wife, Esther. This dissertation has more date nights on its conscience than some might suspect. Many hours and evenings that you would have preferred to spend with me, you have willingly left me to complete this dissertation. You never complained but instead supported me, took most of the housework off my hands, and, more importantly, prayed for me. For that I am deeply grateful. I love you, and I am happy to be married to you.

Abstract

Miniaturization is at the heart of technical progress in the semiconductor industry. As electronic components approach the atomic limit, quantum physical effects increasingly come to the fore, which may lead to fundamentally different electronic and thermal properties. Gold deposited on stepped silicon surfaces self-assembles into one or two-atom-wide atomic wires, whose structural, electronic, and thermal properties are investigated here using the examples of the Si(553)-Au and Si(557)-Au surfaces.

One of the practical problems of miniaturization is the contamination by impurity atoms. As a first and important step to understand the influence of such imperfections, the influence of oxygen on the electronic transport properties at room temperature is investigated in the framework of *ab initio* density-functional theory in the present work. Thereby, different oxygen adsorption sites are identified for the two structurally similar surfaces. In the case of Si(557)-Au, the associated band structures exhibit drastic modifications upon oxygen adsorption, such as an increased effective mass or a band gap opening. Both mechanisms explain the experimentally observed rapid decline in conductivity. A similar modification of the conduction channels is absent in Si(553)-Au, which displays a much smaller decrease in conductivity. Based on these band structures, it is further demonstrated that the upper and lower energy limit of the electron-hole excitation spectrum is directly related to the plasmon dispersion in the case of quasi-one-dimensional systems. More specifically, it is shown that the measured plasmon dispersion and the lower limit of the electron-hole excitation spectrum obtained from density-functional theory allow inferring a general trend of the unoccupied bands. However, small band gaps are not resolved.

A substantial part of this dissertation then addresses fundamental problems of these atomic wires such as one-dimensional spin order and phase transitions. It is demonstrated that a diamagnetic step-edge configuration is responsible for the experimentally observed symmetry breaking of Si(553)-Au at low temperature. In this configuration, every third step edge atom undergoes an $sp^3 \rightarrow sp^2 + p_z$ rehybridization, resulting in an empty dangling bond. Compared to the generally accepted spin-chain model, the rehybridized model is energetically more stable and better accounts for the experimental observations. In contrast, Si(557)-Au favors a spin-polarized surface configuration due to an enhanced spin-spin exchange interaction.

Based on the rehybridized model, the phase transition of Si(553)-Au is examined utilizing *ab initio* molecular dynamics simulations. It is identified as an order-disorder transition, where fluctuations of the step-edge atoms destroy the $\times 3$ order of the surface. A soft Au-chain phonon mode drives the phase transition by transient modifications of the electron chemical potential, which leads to a self-doping of the step-edge dangling bonds. With rising temperatures, also the $\times 2$ order of the Au chains is lost. The order-disorder phase transition well explains previous low-energy electron diffraction, scanning tunneling microscopy, and electronic transport measurements. It is further corroborated by the comparison of surface phonon modes obtained from Raman measurements with calculated vibrational modes within the frozen-phonon approximation. The mechanism of phonon-induced self-doping presented here can be considered to be relevant beyond the scope of self-assembled atomic wires.

Zusammenfassung

Die Miniaturisierung steht im Mittelpunkt des technischen Fortschritts in der Halbleiterindustrie. Mit der Annäherung elektronischer Bauteile an atomare Größen treten zunehmend quantenphysikalische Effekte in den Vordergrund, die zu grundlegend anderen elektronischen und thermischen Eigenschaften führen können. Auf gestufte Siliziumoberflächen abgeschiedenes Gold assembliert sich zu ein oder zwei Atome breite Drähte, deren strukturelle, elektronische und thermische Eigenschaften hier am Beispiel von Si(553)-Au und Si(557)-Au untersucht werden.

Zu den praktischen Problemen der Miniaturisierung gehört die Kontamination durch Fremdatome. Als erster und wichtiger Schritt, um den Einfluss solcher Imperfektionen zu verstehen, wird daher in der vorliegenden Arbeit zunächst der Einfluss von Sauerstoff auf die elektronischen Transporteigenschaften bei Raumtemperatur im Rahmen der Dichtefunktionaltheorie untersucht. Dabei werden unterschiedliche Sauerstoff-Adsorptionsstellen für die beiden strukturell ähnlichen Oberflächen identifiziert. Im Fall von Si(557)-Au weisen die zugehörigen Bandstrukturen drastische Veränderungen durch die Sauerstoffadsorption auf, wie z.B. eine erhöhte effektive Masse und die Öffnung einer Bandlücke. Beide Mechanismen liefern einen Beitrag zu dem experimentell beobachteten starken Abfall der Leitfähigkeit. Ähnliche Modifikationen der Leitungskanäle fehlen bei Si(553)-Au, welches eine wesentlich geringere Reduktion der Leitfähigkeit aufweist. Basierend auf diesen Bandstrukturen wird außerdem gezeigt, dass im Fall von quasi-eindimensionalen Systemen die obere und untere Grenze des Elektron-Loch-Anregungsspektrums direkt mit der Plasmonendispersion zusammenhängt. Insbesondere wird gezeigt, dass die gemessene Plasmonendispersion und die innerhalb der Dichtefunktionaltheorie berechnete untere Grenze des Elektron-Loch-Anregungsspektrums Rückschlüsse auf die unbesetzten Bänder erlauben. Allerdings werden kleine Bandlücken nur begrenzt wiedergegeben.

Ein wesentlicher Teil dieser Arbeit beschäftigt sich anschließend mit fundamentalen Problemen dieser atomaren Drähte wie eindimensionale Spinordnung und Phasenübergänge. Im Fall von Si(553)-Au wird gezeigt, dass eine diamagnetische Stufenkante für die experimentell beobachtete Symmetriebrechung bei tiefen Temperaturen verantwortlich ist. Dabei findet an jedem dritten Stufenkantenatom eine $sp^3 \rightarrow sp^2 + p_z$ Rehybridisierung statt, die zu einer leeren ungesättigten Bindung führt. Verglichen mit dem allgemein akzeptierten Spin-Chain-Modell ist das rehybridisierte Modell energetisch stabiler und erklärt die experimentellen Beobachtungen besser. Im Gegensatz dazu bevorzugt Si(557)-Au eine spinpolarisierter Oberflächenkonfiguration aufgrund einer stärkeren Spin-Spin-Austauschwechselwirkung.

Basierend auf dem rehybridisierten Modell wird der Phasenübergang von Si(553)-Au mit Hilfe von *ab initio* Molekulardynamik-Simulationen untersucht. Dieser wird als ein Ordnungs-Unordnungs-Übergang identifiziert, bei dem Stufenkantenfluktuationen die $\times 3$ Ordnung der Oberfläche zerstören. Eine weiche Phononenmode der Au-Kette treibt den Phasenübergang durch temporäre Änderungen des chemischen Elektronenpotentials an, was zu einer Selbstdotierung der ungesättigten Stufenkantenbindungen führt. Mit steigender Temperatur geht auch die $\times 2$ Ordnung der Au-Ketten verloren. Der Ordnungs-Unordnungs-Phasenübergang liefert eine Erklärung für frühere Rastertunnelmikroskopie-, elektronische Transport-

und niederenergetische Elektronenbeugungsexperimente. Er wird außerdem durch den Vergleich von Oberflächenphononenmoden aus Raman-Messungen mit berechneten Schwingungsmoden innerhalb der *Frozen-Phonon*-Approximation bestätigt. Der hier vorgestellte Mechanismus der phononeninduzierten Selbstdotierung kann weit über den Bereich der selbstassemblierten atomaren Drähte hinaus als relevant angesehen werden.

Contents

Acknowledgements	v
Abstract	vii
Notation	xiii
1 Introduction	1
2 Theory	3
2.1 A Brief Introduction to Luttinger Liquid Theory	3
2.1.1 Fermi Liquid Theory	3
2.1.2 Breakdown of Fermi Liquid Theory in 1D	6
2.2 Peierls Instability	8
2.3 The Mermin-Wagner Theorem	9
2.4 Nosé-Hoover Thermostat	14
3 Self-Assembled Au Atomic Wires on Vicinal Si(111) Surfaces	17
3.1 Silicon Surfaces	17
3.2 Au on Si(111)	19
3.2.1 Au on Vicinal Si(111) Surfaces	19
3.3 Au on Si(553)	22
3.3.1 Atomic Structure	22
3.3.2 Electronic Structure	25
3.3.3 Phase Transition	29
3.4 Au on Si(557)	32
3.4.1 Atomic Structure	32
3.4.2 Electronic Structure	33
3.4.3 Phase Transition	34
4 Electronic Properties of Clean and Oxidized Si(hhk)-Au Surfaces	35
4.1 Influence of Oxygen Adsorption on the Conductivity of Si(553)-Au and Si(557)-Au	36
4.1.1 Structural Changes Induced by Oxygen Adsorption	36
4.1.2 Transport Properties of the Clean and Oxygen-Adsorbed Surfaces	37
4.1.3 Adsorption Sites of Molecular Oxygen	39
4.1.4 Band-Structure Changes Induced by Oxygen Adsorption	43
4.1.5 Analysis of the Transport Data	45
4.2 Probing Quasi-1D Electronic Excitation Spectra by DFT-Aided Plasmon Spectroscopy	46
4.2.1 Plasmon spectroscopy	46
4.2.2 Electronic Excitation Spectrum of Clean and Oxidized Si(557)-Au	48
4.2.3 Electronic Excitation Spectrum of Clean Si(755)-Au	52
5 Low-Temperature Structure of Si(553)-Au	55
5.1 Structure Determination	56
5.1.1 Methodology	56
5.1.2 The Rehybridized Model	56

5.2	Influence of the Exchange-Correlation Functional on the Stability	58
5.3	Comparison with the Experiment	59
5.3.1	Calculated Band Structures and ARPES	60
5.3.2	Simulated and Experimental STM	61
5.4	Transferability of the Rehybridized Model to Si(557)-Au	62
6	Phase Transition of Si(553)-Au	63
6.1	A Transition Scenario Analyzed by Total-Energy Calculations	63
6.1.1	Potential Energy Surface	64
6.1.2	Vibrational Free-Energy Correction	64
6.1.3	Band Modifications	65
6.2	Ab Initio Molecular Dynamics Simulation	68
6.2.1	Methodology	68
6.2.2	Structural Analysis of the Step Edge and Au Chain	68
6.2.3	Transient Magnetic States	71
6.3	Comparison with Experimental Results	72
6.3.1	Raman Spectroscopy	72
6.3.2	SPA-LEED	73
7	Conclusion and Outlook	75
Appendix A	Molecular Dynamics Simulations	79
A.1	Velocity Distribution	79
A.2	Structural Details	80
Bibliography		83
List of Figures		93
List of Tables		95
List of Publications		97

Notation

Abbreviations

1D	one-dimensional or one dimension
2D	two-dimensional or two dimension
3D	three-dimensional or three dimension

Experimental Methods

2PPE	two-photon photoemission
4PP	four-point probe
ARPES	angle-resolved photoemission spectroscopy
EEL	electron energy loss
EELS	electron energy loss spectroscopy
LEED	low-energy electron diffraction
SPA-LEED	spot-profile analysis LEED
STM	scanning tunneling microscopy
STS	scanning tunneling spectroscopy
XRD	X-ray diffraction

Other Acronyms

AIMD	<i>ab initio</i> molecular dynamics
BZ	Brillouin zone
CDW	charge-density wave
DB	dangling bond
DC	direct current
DFT	density-functional theory
DOS	density of states
FS	Fermi surface
e-h	electron-hole
FWHM	full width at half maximum
GGA	generalized gradient approximation
HCC	honeycomb chain
HSE	Heyd, Scuseria and Ernzerhof—the inventors of the HSE06 hybrid XC functional

<i>I</i> - <i>V</i>	current-voltage
K	Krawiec
LDA	local-density approximation
LT	low temperature
MIT	metal-insulator transition
ML	monolayer
NFEG	nearly free electron gas
PAW	projector-augmented wave
PBE	Perdew-Burke-Ernzerhof—an XC functional based on GGA
PBEsol	A PBE derivative optimized to improve lattice parameters of bulk solids and their surfaces
PES	potential energy surface
R	rehybridized
SC	spin-chain
SCL	space charge layer
VASP	Vienna <i>ab initio</i> simulation package
XC	exchange-correlation

Elements

Li	lithium
O	oxygen
Na	sodium
Si	silicon
Ca	calcium
Rb	rubidium
Ag	silver
In	indium
Au	gold
Pb	lead

I am awaiting the day when people remember the fact that discovery does not work by deciding what you want and then discovering it.

N. David Mermin

1

Introduction

In his 1884 novella *Flatland*¹, Edwin A. Abbot describes a two-dimensional (2D) world that is populated by polygons. On a journey of the protagonist *A Square* to the one-dimensional (1D) *Lineland*, he comes to realize that the points inhabiting this land neither perceive nor are willing to acknowledge the existence of a 2D world. Ironically, the protagonist himself does not believe in the existence of a three-dimensional (3D) world, but eventually changes his mind after a controversial discussion with a sphere and a visit to *Sphereland*. Likewise, the sphere is indignant about *A Square*'s idea of a possible world whose dimension exceeds that of a 3D world. One after another, the characters in this novel must realize that there are other worlds of higher dimensions of which they have not been aware.

Interestingly, mankind seems to have traveled a very similar path: Since the discovery of the theory of relativity in 1910², the knowledge of a four-dimensional spacetime has settled in our minds. While it has helped us raise our eyes to the things above and improved our understanding of the universe, it also—figuratively speaking—diverted our attention from the things below at our feet: Only later was it discovered that low-dimensional systems possess properties that are exclusive to these dimensions.

In solid-state physics—long before the crystalline structure of many materials was proved by X-ray scattering³—the focus has been primarily on bulk materials. It was not until later in the 1960s that surfaces also grew in relevance due to improved ultra-high vacuum technology, the availability of single-crystalline samples, and the discoveries made in the field of electron-solid interactions⁴. However, it took another 50 years and a Nobel Prize awarded to Geim and Novoselov before the importance of 2D systems was recognized by a broader scientific community. Although most of the theory was developed earlier⁵, it was the discovery of graphene with its exotic properties that significantly pushed the advance of 2D physics⁶.

The scientific community engaged in 1D physics finds itself in a similar state of tension: In the 1950s, Tomonaga and Luttinger laid the foundation for the theoretical description of 1D objects^{7,8}. These possess a variety of exotic properties, such as spin-charge separation. Consequently, charge and spin waves are distinctive excitations of a Luttinger liquid material. However, due to the inherent instability of 1D systems, finding materials that actually behave as Luttinger liquids is challenging⁹. To this day, scientists are working on the realization of 1D systems where at least some of these exotic properties can be observed.

One family of structures with a 1D topology are gold nanowires grown on silicon surfaces. These atomic wires self-assemble on Si(111) and its vicinal surfaces, forming regions of equidistant, parallel Au chains¹⁰. These systems have been extensively investigated for characteristics that can be attributed to 1D physics. Although initially it seemed that one of these systems exhibited spin-charge separation¹¹, further investigations have shown that the system behaves neither like a Luttinger liquid nor like a classical Peierls system¹². However, it was suggested that several properties of two respective vicinal surfaces—namely Si(553)-Au and Si(557)-Au—could be explained by an antiferromagnetic spin chain ordering¹³. The formation of spin chains in the absence of magnetic materials is a largely unexplored field. Among their possible applications are the realization of high-density storage devices¹⁴ or spin-shift registers¹⁵. A detailed investigation of these spin chains is part of this dissertation.

Furthermore, the Si(553)-Au surface exhibits a complex phase transition. This is reflected very differently in the structural, electronic, and transport properties, e.g., in the measured transition temperature¹⁶. Therefore, an important aspect of this dissertation is the study of this phase transition.

Another critical aspect is the ongoing miniaturization in semiconductor manufacturing. The year 2020 marked the milestone at which 5 nm manufacturing entered volume production¹⁷. In contrast, the self-assembled gold wires on the vicinal Si(111) surfaces consist of one to two gold atoms in width, corresponding to an effective width of the transport channel as low as 0.6 nm¹⁸. A better understanding of self-assembled nanowires could, therefore, play a significant role in future miniaturization.

N. D. Mermin's quote at the beginning of this introduction is a good reminder that science often holds treasures that one did not expect to find. One digs in hope for a particular discovery and stumbles upon quite another. This dissertation was no different: In search of an explanation for the complex phase transition of Si(553)-Au in the context of spin chains, my supervisor Prof. Dr. W. G. Schmidt and I not only stumbled upon a new structural model that eliminates the need for spin chains; we also found a novel mechanism for the self-doping of dangling bond nanostructures. This mechanism is facilitated by transient changes of the electronic chemical potential by coupling to a low-frequency phonon mode.

This dissertation is structured as follows: Chapter 2 lays the theoretical foundations of 1D systems. This includes a brief summary of Fermi liquid theory and its failure in one dimension as well as a concise outline of Luttinger liquid theory. Later, the Peierls instability and Mermin-Wagner theorem are described. Subsequently, the Nosé-Hoover thermostat is discussed, which is a fundamental building block of the *ab initio* molecular dynamics simulations presented in this dissertation. Chapter 3 introduces self-assembled metallic wires with a focus on gold wires on silicon surfaces. A summary of the results of Si(553)-Au—and in a shorter form of Si(557)-Au—published to this day are collected and discussed.

Starting with chapter 4, the results of this dissertation are presented. This chapter deals in particular with the influence of oxygen on the electronic properties of Si(553)-Au and Si(557)-Au. Besides determining the oxygen adsorption sites, the different influence of O₂ on both surfaces is analyzed. Furthermore, a theory for predicting unoccupied bands based on experimental plasmon dispersions and calculated occupied bands is tested. The spin-chain model for Si(553)-Au and Si(557)-Au is examined in more detail in chapter 5. Thereby, a new structural model for Si(553)-Au is introduced and compared with the spin-chain model based on available experimental data. Chapter 6 focuses on the phase transition of the Si(553)-Au surface. Finally, *ab initio* molecular dynamics simulations are used to investigate the phase transition, and the obtained results are validated against experimental data.

*This proving of such and such I found to be almost like cheating.
You start somewhere, and then you go into a dark tunnel, and
then you come out at another place. You find that you have
proved what you wanted to prove, but in the tunnel, you don't
see anything.*

Werner Heisenberg

2

Theory

This chapter discusses the theoretical background that largely supplements the findings in this dissertation. Sections 2.1–2.3 cover the specifics of 1D systems, why they are fundamentally different from higher-dimensional^a materials, and the particular challenges such as the Peierls instability and the Mermin-Wagner theorem. Section 2.4 then discusses the Nosé-Hoover thermostat used in chapter 6 for the *ab initio* molecular dynamics simulations at finite temperatures.

2.1 A Brief Introduction to Luttinger Liquid Theory

The physics underlying one-dimensional metals is best explained by starting with the model describing their 3D counterparts: the Fermi liquid theory established by L. D. Landau^{19–22}. After a brief summary of this theory, its limited applicability to 1D systems is outlined along with a concise overview of Luttinger liquid theory. A phenomenological approach is followed here in most cases. This facilitates a brief, understandable overview without going into too much technical detail. Most of the derivations in this section are based on Refs. [23, 24], and the reader is referred to these materials for a more extensive analysis.

2.1.1 Fermi Liquid Theory

A system consisting of N identical, noninteracting electrons in a large volume V is fully described by the momentum distribution function of the ground state $n_0(\mathbf{k})$. At $T = 0$ K, the distribution function is unity for all momenta $|\mathbf{k}| =: k < k_F$, i.e., all states up to the Fermi wavevector k_F are filled. As illustrated in Fig. 2.1(a), all other states are unoccupied at 0 K, and the distribution function has a discontinuity of size 1. This discontinuity then defines the Fermi surface. The Fermi wavevector k_F is given by²⁵

$$\frac{4\pi}{3}k_F^3 = \frac{N}{g} \frac{(2\pi)^3}{V} \quad \iff \quad k_F = \left(\frac{6\pi^2 N}{gV} \right)^{1/3}, \quad (2.1)$$

^aEverything with a dimension greater than one is considered high-dimensional here.

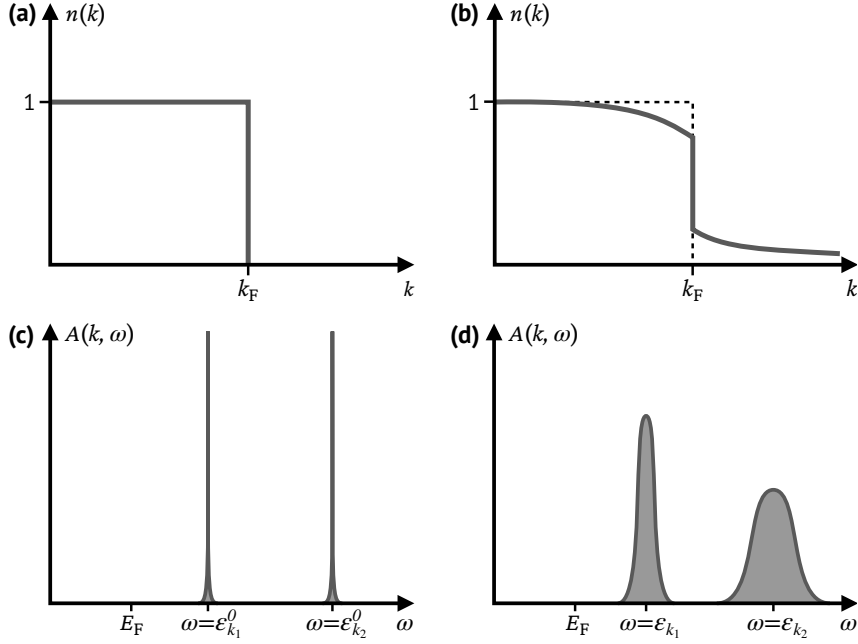


Figure 2.1: The distribution function of (a) free noninteracting electrons and (b) interacting electrons at $T = 0$ K. (c) The spectral function $A(k, \omega)$ consists of delta functions in the case of free electrons, showing well-defined excitations for $\omega = \varepsilon_k$. (d) The excitations are broadened for interacting electrons and get sharper close to the Fermi energy E_F (see text).

where g is the spin degeneracy. With the reduced Planck's constant set to unity $\hbar = 1$, the total energy of the ground state is

$$E[n_0] = \sum_{\mathbf{k}} \left(\frac{k^2}{2m} - E_F \right) n_0(\mathbf{k}) \quad \text{with} \quad E_F := \frac{k_F^2}{2m}. \quad (2.2)$$

Here, m is the mass of an electron, and E_F is the Fermi energy up to which the states are occupied.

Within the Fermi liquid theory, an excitation is defined by adding a single particle to the system. As N and V are large, the excitation is measured by $\delta n_0(\mathbf{k}) = \tilde{n}(\mathbf{k}) - n_0(\mathbf{k})$. The kinetic energy of a free electron with momentum \mathbf{k} then yields

$$\varepsilon_{\mathbf{k}}^0 = \frac{\delta E[n_0]}{\delta n_0(\mathbf{k})} = \frac{k^2 - k_F^2}{2m}. \quad (2.3)$$

Since the Fermi sea is filled up to the Fermi energy E_F at zero temperature, the Pauli principle ensures that electrons are added at energies $\varepsilon_{\mathbf{k}}^0 > E_F$ with $\delta n_0 > 0$ (and holes at $\varepsilon_{\mathbf{k}}^0 < E_F$ with $\delta n_0 < 0$). The excitations are eigenstates of the Hamiltonian and thus have an infinite lifetime. More specifically, the retarded Green's function of a free electron is given by²⁶

$$G_{\text{ret}}(\mathbf{k}, \omega) = \lim_{\eta \rightarrow 0^+} \frac{1}{\varepsilon_{\mathbf{k}}^0 - \omega + i\eta}. \quad (2.4)$$

The excitations are characterized by the spectral function

$$A(\mathbf{k}, \omega) = -\frac{1}{\pi} \text{Im} G_{\text{ret}}(\mathbf{k}, \omega), \quad (2.5)$$

which gives the probability of finding a state with frequency ω and momentum \mathbf{k} ²³. For free particles, the spectral function is a delta distribution with $A(\mathbf{k}, \omega) = \delta(\omega - \varepsilon_{\mathbf{k}}^0)$, see Fig. 2.1(c). According to the Heisenberg uncertainty, the sharp energy corresponds to an infinite lifetime of the excitations. This is consistent with the fact that these excitations are eigenstates of the Hamiltonian.

In the case of interacting particles, treating the Coulomb interaction is difficult because it has the same order of magnitude as the kinetic energy. This makes it unsuitable for perturbation theory. One of the key aspects of the Fermi liquid theory is that most macroscopic properties rely on excitations close to the Fermi energy²⁴. L. D. Landau proposed an ansatz where the interaction is adiabatically switched on, i.e., slowly, on an infinite timescale. In this way, the excited states near the Fermi energy cannot make a transition to other states²¹. The bare particles gradually change to quasiparticles that dress themselves with density fluctuations²³. These quasiparticles are in a one-to-one correspondence with the bare particles and stay fermionic with the same quantum numbers. Close to the Fermi energy, the phase space is strongly limited: Only a few states exist with which the quasiparticles can scatter, and most particles are frozen in the Fermi sea²⁴. Therefore, these considerations remain valid for low temperatures. Compared to the Fermi temperature, which is ~ 10.000 K for metals, the temperatures can almost always be considered “low”²³.

Same as with noninteracting particles, the system is specified by the momentum distribution function $n(\mathbf{k})$, which retains its discontinuity at E_F . However, its discontinuity is renormalized by the particle interaction²⁶, as illustrated in Fig. 2.1(b). The difference to the distribution function of the bare electrons is measured by $\delta n(\mathbf{k}) = n(\mathbf{k}) - n_0(\mathbf{k})$. A second-order expansion of the energy change δE then yields

$$\delta E[n] = \sum_{\mathbf{k}} \varepsilon_{\mathbf{k}}^0 \delta n(\mathbf{k}) + \frac{1}{2} \sum_{\mathbf{k}, \mathbf{k}'} f(\mathbf{k}, \mathbf{k}') \delta n(\mathbf{k}) \delta n(\mathbf{k}'), \quad (2.6)$$

and therefore

$$\varepsilon_{\mathbf{k}} = \frac{\delta E[n]}{\delta n(\mathbf{k})} = \varepsilon_{\mathbf{k}}^0 + \frac{1}{2} \sum_{\mathbf{k}'} f(\mathbf{k}, \mathbf{k}') \delta n(\mathbf{k}'), \quad (2.7)$$

where $f(\mathbf{k}, \mathbf{k}')$ is the second-order functional derivative of $E[n]$ and the quasiparticle interaction. Because the Fermi liquid is isotropic, the same must hold for the quasiparticle interaction so that

$$\nabla_{\mathbf{k}} \varepsilon_{\mathbf{k}} = \frac{\mathbf{k}}{m} + \frac{1}{2} \nabla_{\mathbf{k}} \sum_{\mathbf{k}'} f(\mathbf{k}, \mathbf{k}') \delta n(\mathbf{k}') \propto \mathbf{k}. \quad (2.8)$$

For $\mathbf{k} = \mathbf{k}_F$, the constant of proportionality can be identified with an inverse effective mass $1/m^*$. While many of the bare particle’s static properties are retained, the dynamical properties of the quasiparticles, such as the effective mass, are renormalized. More formally, the Green’s function of an interacting electron can be written as

$$G(\mathbf{k}, \omega) = \frac{1}{\varepsilon_{\mathbf{k}}^0 - \omega - \Sigma(\mathbf{k}, \omega)}, \quad (2.9)$$

where $\Sigma(\mathbf{k}, \omega)$ is the complex self-energy containing all the many-body effects²⁴. Following Eq. 2.5, the spectral function of the quasiparticles yields

$$A(\mathbf{k}, \omega) = -\frac{1}{\pi} \frac{\text{Im } \Sigma(\mathbf{k}, \omega)}{[\varepsilon_{\mathbf{k}}^0 - \omega - \text{Re } \Sigma(\mathbf{k}, \omega)]^2 + [\text{Im } \Sigma(\mathbf{k}, \omega)]^2}. \quad (2.10)$$

The excitations of the quasiparticles are no sharp delta peaks but rather Lorentz distributions, which are shifted by the real part and broadened by the imaginary part of the self-energy. Consequently, the quasiparticles have a finite lifetime related to $[\text{Im } \Sigma(\mathbf{k}, \omega)]^{-1}$. Since $\text{Im } \Sigma$ decreases as $\propto (E_F - \omega)^2$, the excitations become sharper close to the Fermi energy and are well-defined only there²⁶, see Fig. 2.1(d). The quasiparticles are not the exact eigenstates of the Hamiltonian but rather a superposition of many exact stationary states. These accumulate in narrow energy ranges and form the individual quasiparticles²³.

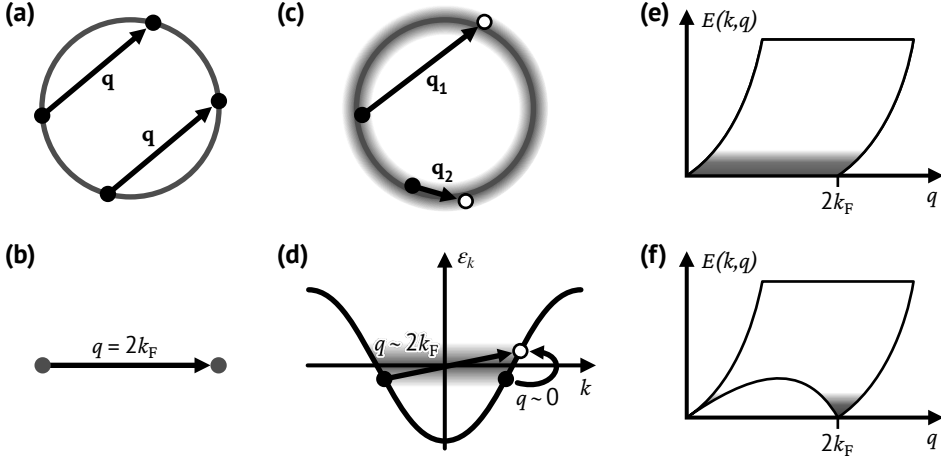


Figure 2.2: (a) In high-dimensional space, the nesting condition for a momentum $|\mathbf{q}| \leq 2k_F$ is satisfied only for a limited set of points. The gray circle indicates the Fermi surface of radius k_F . (b) Perfect nesting is accomplished in 1D for $q = 2k_F$ due to the distinctive shape of the Fermi surface given by two (gray) points. (c, e) Low-energetic (shaded area) e-h excitations are possible for all $|\mathbf{q}| \leq 2k_F$ in high-dimensional space. (d, f) In 1D, low-energetic e-h excitations are limited to wavevectors $q \sim 0$ and $q \sim 2k_F$.

2.1.2 Breakdown of Fermi Liquid Theory in 1D

The Fermi surface in 1D is fundamentally different from the Fermi surfaces in higher dimensions: In 3D and 2D, the ideal Fermi surface is given by a sphere and a circle. Both topologies are connected spaces. In contrast, the 1D Fermi surface consists of two disjoint points separated by $2k_F$, as illustrated in Fig. 2.2(a)–(b). For a small perturbation

$$H_{\text{pert}}(t) = \int d\mathbf{x} \nu(\mathbf{x}, t) \hat{\rho}(\mathbf{x}), \quad (2.11)$$

with a weak potential $\nu(\mathbf{x}, t)$ and electron density operator $\hat{\rho}(\mathbf{x})$, the linear response function of the electron density in reciprocal space within the Lindhard approximation²⁷ is given by²³

$$\chi(\mathbf{q}, \omega) = \lim_{\eta \rightarrow 0^+} \frac{1}{V} \sum_{\mathbf{k}} \frac{f_F(\epsilon_{\mathbf{k}}) - f_F(\epsilon_{\mathbf{k}+\mathbf{q}})}{\omega + \epsilon_{\mathbf{k}} - \epsilon_{\mathbf{k}+\mathbf{q}} + i\eta}. \quad (2.12)$$

Here, $f_F(\epsilon_{\mathbf{k}}) = (\exp(\epsilon_{\mathbf{k}} \beta) + 1)^{-1}$ is the Fermi-Dirac distribution function, $\beta = \frac{1}{k_B T}$ is the inverse temperature, and k_B is the Boltzmann constant.

In the static case ($\omega = 0$), the sum in Eq. 2.12 is well-defined for most \mathbf{q} . An exception exists for a wavevector \mathbf{q} that connects a set of points on the Fermi surface (called nesting) with $\epsilon(\mathbf{k}) \rightarrow 0^+$ and $\epsilon(\mathbf{k} + \mathbf{q}) \rightarrow 0^-$ or vice versa. In this case, a singularity is introduced due to the discontinuity of the Fermi-Dirac distribution at $T = 0$ K. More generally, if a wavevector \mathbf{q} satisfies the relation $\epsilon_{\mathbf{k}+\mathbf{q}} = -\epsilon_{\mathbf{k}}$ for a finite domain \mathbb{D} of \mathbf{k} vectors, the real part of the summands in Eq. 2.12 transforms according to

$$\text{Re} \frac{f_F(\epsilon_{\mathbf{k}}) - f_F(\epsilon_{\mathbf{k}+\mathbf{q}})}{\epsilon_{\mathbf{k}} - \epsilon_{\mathbf{k}+\mathbf{q}} + i\eta} \xrightarrow{\mathbf{k} \in \mathbb{D}} -\frac{\tanh(\beta \epsilon_{\mathbf{k}}/2)}{2\epsilon_{\mathbf{k}}}. \quad (2.13)$$

As the temperature approaches 0 K, these linear response terms become singular at the Fermi surface.

It is impossible to satisfy the nesting condition except for a few single points for higher dimensions, see Fig. 2.2(a). These singularities are thus smoothed out by the summation (or integration for $V \rightarrow \infty$) over a large number of wavevectors. However, they become significant in $\nabla_{\mathbf{q}} \chi(\mathbf{q})$ and are responsible for the

Friedel oscillation and the Kohn anomaly²³. In 1D, however, Fermi nesting for $q = 2k_F$ is rather the rule than an exception. This can be seen by linearizing the single-particle energies near k_F :

$$\left. \begin{aligned} \varepsilon_k &\simeq \frac{k_F}{m^*} (k - k_F), & k \sim k_F \\ \varepsilon_k &\simeq \frac{k_F}{m^*} (-k - k_F), & k \sim -k_F \end{aligned} \right\} \Rightarrow \varepsilon_{k+2k_F} = -\varepsilon_k \quad (2.14)$$

As a result, the real part of the linear response function (for $V \rightarrow \infty$) diverges in temperature as

$$\text{Re } \chi(2k_F, \omega = 0) = - \int d\varepsilon N(\varepsilon) \frac{\tanh(\beta\varepsilon/2)}{2\varepsilon} \propto -\log(\xi\beta), \quad (2.15)$$

where $N(\varepsilon)$ is the density of states per unit volume and ξ is some ultraviolet cutoff of similar size as the energy range over which the nesting condition holds²³. This singularity is regularized by the temperature. A similar regularization is obtained by a finite frequency²³ $\omega > 0$. The singularity leads to a breakdown of Fermi liquid theory in 1D: The coupling of quasiparticles to collective excitations is small in 2D or 3D but large in 1D for excitations close to the Fermi energy—regardless of the size of the perturbation²⁸.

In fact, the situation is even more complicated: Instabilities of a similar form occur upon the creation or destruction of particle pairs and electron-hole (e-h) pairs. The former is related to the Bardeen-Cooper-Schrieffer superconducting instability²³. These singularities push the system to—mostly competing—phases, of which a Luttinger liquid and a Peierls condensate (see section 2.2) are two examples²⁹.

The Luttinger liquid theory relies on the narrow window of allowed low-energetic e-h excitations in 1D: In higher dimensions, low-energetic excitations are possible for a continuum of wavevectors with $|\mathbf{q}| < 2k_F$. In contrast, the Fermi surface in 1D consists only of two points. Therefore, the same excitations are only possible for $q \sim 0$ and $q \sim 2k_F$, as illustrated in Fig. 2.2(c)–(f). For excitations with $q \sim 0$ and a quadratic dispersion (cf. Eq. 2.3), the e-h excitation energy is given by

$$E_{\text{eh}}(k, q) = \varepsilon_{k+q}^0 - \varepsilon_k^0 = \frac{kq}{m} + \frac{q^2}{2m}. \quad (2.16)$$

The average excitation energy $E_{\text{eh}}(q) = \langle E_{\text{eh}}(k, q) \rangle$ and energy dispersion $\delta E_{\text{eh}}(q) = \max(E_{\text{eh}}(k, q)) - \min(E_{\text{eh}}(k, q))$ in the interval $k \in [k_F - q, k_F]$ are²³

$$E_{\text{eh}}(q) = \frac{k_F q}{m} \quad \text{and} \quad \delta E_{\text{eh}}(q) = \frac{q^2}{m}. \quad (2.17)$$

These two relations show that an e-h excitation has a well-defined momentum q and energy E_{eh} in 1D near k_F : The energy uncertainty $\delta E_{\text{eh}}(q)$ decreases faster than the energy $E_{\text{eh}}(q)$ when approaching the Fermi surface. This situation is similar to the quasiparticles in the Fermi liquid, i.e., e-h excitations are well-defined “particles” that replace the dressed electrons of Fermi liquid theory.

Because an e-h excitation consists of two spin-1/2 particles, it can be treated as a boson. S. Tomonaga showed that this is strictly valid only in 1D due to the almost linear, narrow energy-momentum dispersion relation close to the Fermi surface⁷ (see Fig. 2.2(f)). This forces the electron and hole to travel with the same group velocity³⁰. Based on this idea, he proposed a new model for 1D metals by utilizing the principle of *bosonization*. Luttinger then reformulated this model in terms of Bloch waves and removed several unnecessary constraints made by Tomonaga⁸. He showed that these systems can be described by two types of massless noninteracting bosons. These consist of a large collection of e-h excitations and can be identified with charge and spin waves. These travel with different group velocities, which give rise to the spin-charge separation only present in 1D metals.

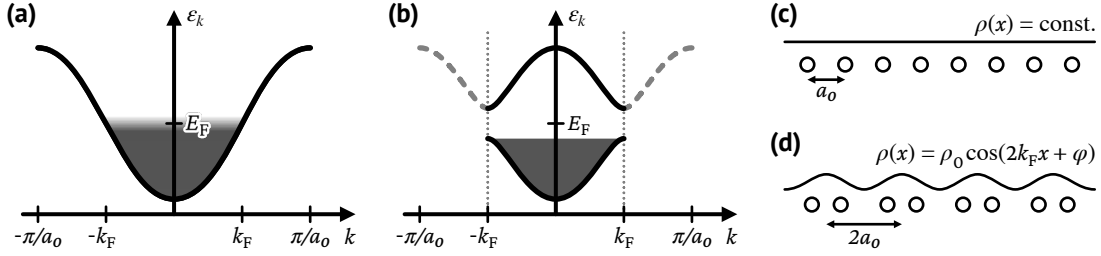


Figure 2.3: The dispersion of a half-filled band **(a)** before and **(b)** after the Peierls distortion. The black solid curve and the dark shading indicate the band and its filling up to the Fermi energy E_F . Gray dashed lines illustrate the unfolded part of the band extending beyond the new BZ boundary, denoted by gray dotted lines. The approximately constant charge density $\rho(x)$ of the equidistant 1D chain in **(c)** is periodically modulated by the Peierls distortion, leading to a CDW.

2.2 Peierls Instability

In 1955, R. E. Peierls showed that a 1D chain of metallic atoms is subject to a metal-insulator transition (MIT)⁹. He argued that metallic atoms having a single valence electron lead to a half-filled band with $k_F = \frac{\pi}{2a_0}$, where a_0 is the distance between two atoms. A small distortion of wavevector $2k_F = \frac{\pi}{a_0}$, e.g., by a phonon, then leads to a period-doubling lattice distortion. This period doubling corresponds to a bisection of the Brillouin zone (BZ), which leads to a backfolding of the half-filled band, as illustrated in Fig. 2.3(a)–(b). The intersection of the band with its backfolded counterpart at the new BZ boundary leads to a band gap that reduces the energy of the system. The periodic lattice distortion is accompanied by a charge-density wave (CDW), i.e., a periodic modulation of the charge density shown in Fig. 2.3(c)–(d).

The Peierls instability is not restricted to a single valence electron per atom or a period doubling. Instead, it can be extended to arbitrary electron fillings. For fillings of $1/n$ with $n \in \mathbb{N}$, the associated CDWs and n -periodic lattice distortions are commensurate with the underlying lattice³¹.

More precisely, the Peierls instability is tightly connected to the Lindhard susceptibility in Eq. 2.12. The corresponding charge modulation in reciprocal space is then given by $\delta\rho(k, \omega) = \chi(k, \omega)v(k, \omega)$. Because of the instability of $\chi(k, \omega)$ at $k = 2k_F$, the charge modulation also peaks at $k = 2k_F$. It can be approximated in real space (neglecting any time dependency) by $\delta\rho(x) \simeq \cos(2k_F x)$. A periodic lattice distortion of the same wavevector $k = 2k_F$ stabilizes this CDW. Although it has been theorized that a CDW could exist in the absence of a periodic lattice distortion³², J. Friedel provided several physical arguments why this is rather unlikely³³. So far, both have only been observed as a pair³¹.

The Peierls instability precludes the existence of a freestanding 1D atomic wire. However, bulk crystalline materials with extraordinary quasi-1D anisotropy^{34,35}, self-assembled atomic wires³⁶ and, more recently, 2D topological insulators with spin-momentum-locked 1D edge states^{37–40} are considered as candidates for the observation of 1D electron physics⁴¹. Interestingly, it is the coupling to higher dimensions that stabilize the Peierls-induced CDW at finite temperatures. Otherwise, the Peierls condensate would be stable only at $T = 0 \text{ K}$ ³⁶.

A Peierls transition and Luttinger liquid behavior are mutually exclusive and depend on the coupling to higher dimensions. In the case of a Peierls-induced MIT, the band gap opening precludes any low-energetic collective excitations, which is the basis of Luttinger liquid theory. In contrast, the density of states (DOS) at the Fermi level in a Luttinger liquid is diluted due to the strong interaction and collective excitations. Therefore, the single-particle picture and thus the Peierls argument is not valid anymore³⁶.

2.3 The Mermin-Wagner Theorem

In 1996, P. C. Hohenberg showed that conventional superfluid or superconducting ordering is prohibited in 1D and 2D systems⁴². Inspired by conversations with Hohenberg, N. D. Mermin and H. Wagner proved that the same argument extends to magnetic ordering⁴³. In the original paper, the Mermin-Wagner theorem states that “*at any nonzero temperature, a one- or two-dimensional isotropic spin- S Heisenberg model with finite-range exchange interaction can be neither ferromagnetic nor antiferromagnetic.*”⁴³ The proof given here closely follows the line of argument in Ref. [44].

The Bogoliubov Inequality

Both the Mermin-Wagner theorem⁴³ and the theorem by Hohenberg⁴² are based on the Bogoliubov inequality⁴⁵, which is a rather general inequality concerning two arbitrary operators \hat{A} and \hat{C} in the context of a physical system described by the Hamiltonian \hat{H} . It is based on the Schwarz inequality and yields

$$\frac{1}{2}\beta \langle \{\hat{A}, \hat{A}^\dagger\} \rangle \langle [[\hat{C}, \hat{H}], \hat{C}^\dagger] \rangle \geq |\langle [\hat{C}, \hat{A}] \rangle|^2, \quad (2.18)$$

where $\langle \cdots \rangle$, $[\cdots]$ and $\{\cdots\}$ denote the expectation value, the commutator and the anticommutator.

Let $|n\rangle$ and E_n be the eigenstates and eigenenergies of \hat{H} with

$$E_n = \langle n | \hat{H} | n \rangle; \quad \langle \cdots \rangle = \sum_n W_n \langle n | \cdots | n \rangle \quad \text{with} \quad W_n = \frac{e^{-\beta E_n}}{\text{Tr}(e^{-\beta \hat{H}})}. \quad (2.19)$$

The Bogoliubov inequality is then derived by the definition of a new scalar product

$$(\hat{A}, \hat{B}) = \sum_{n,m}^{E_n \neq E_m} \langle n | \hat{A}^\dagger | m \rangle \langle m | \hat{B} | n \rangle \frac{W_m - W_n}{E_n - E_m}. \quad (2.20)$$

This scalar product is positive semidefinite because it satisfies the following conditions:

i *Linearity* in the second argument: Let $\alpha_1, \alpha_2 \in \mathbb{C}$, then

$$(\hat{A}, \alpha_1 \hat{B}_1 + \alpha_2 \hat{B}_2) = \alpha_1 (\hat{A}, \hat{B}_1) + \alpha_2 (\hat{A}, \hat{B}_2). \quad (2.21)$$

ii *Conjugate symmetry*: Because $(\langle n | \hat{B}^\dagger | m \rangle \langle m | \hat{A} | n \rangle)^* = \langle n | \hat{A}^\dagger | m \rangle \langle m | \hat{B} | n \rangle$ is a complex number and $(W_m - W_n)/(E_n - E_m)$ is a real number, (\hat{A}, \hat{B}) is also a complex number with

$$(\hat{A}, \hat{B}) = (\hat{B}, \hat{A})^*. \quad (2.22)$$

iii *Positive semidefiniteness*: As $(W_m - W_n)/(E_n - E_m) \geq 0$ and $\langle n | \hat{A}^\dagger | m \rangle \langle m | \hat{A} | n \rangle = |\langle m | \hat{A} | n \rangle|^2$, it holds that

$$(\hat{A}, \hat{A}) \geq 0. \quad (2.23)$$

As a consequence, from $\hat{A} = 0$ it follows that $(\hat{A}, \hat{A}) = 0$, but the opposite is not true. For instance, $(\hat{H}, \hat{H}) = 0$ for $\hat{H} \neq 0$. The same holds for any other operator \hat{O} that commutes with \hat{H} .

For the specific choice $\hat{B} = [\hat{C}^\dagger, \hat{H}]$, the scalar product (\hat{A}, \hat{B}) yields

$$\begin{aligned} (\hat{A}, \hat{B}) &= \sum_{n,m}^{E_n \neq E_m} \langle n | \hat{A}^\dagger | m \rangle \langle m | [\hat{C}^\dagger, \hat{H}] | n \rangle \frac{W_m - W_n}{E_n - E_m} \\ &= \sum_{n,m} \langle n | \hat{A}^\dagger | m \rangle \langle m | \hat{C}^\dagger | n \rangle (W_m - W_n). \end{aligned} \quad (2.24)$$

We can include the diagonal terms $E_n = E_m$ in the second line due to the removable discontinuity in the denominator and $(W_m - W_n) = 0$ for $m = n$. Using the completeness relation and the definition of W_n in Eq. 2.19, it follows

$$\begin{aligned} (\hat{A}, \hat{B}) &= \sum_m W_m \langle m | \hat{C}^\dagger \hat{A}^\dagger | m \rangle - \sum_n W_n \langle n | \hat{A}^\dagger \hat{C}^\dagger | n \rangle \\ &= \langle [\hat{C}^\dagger, \hat{A}^\dagger] \rangle. \end{aligned} \quad (2.25)$$

Substituting $\hat{A} = \hat{B} = [\hat{C}^\dagger, \hat{H}]$, the scalar product yields

$$(\hat{B}, \hat{B}) = \langle [\hat{C}^\dagger, [\hat{H}, \hat{C}]] \rangle \geq 0. \quad (2.26)$$

As the last step, we estimate the scalar product (\hat{A}, \hat{A}) with the help of the following relation:

$$\begin{aligned} 0 &< \frac{W_m - W_n}{E_n - E_m} \\ &= \frac{1}{E_n - E_m} \frac{e^{-\beta E_m} + e^{-\beta E_n}}{\text{Tr}(e^{-\beta \hat{H}})} \frac{e^{-\beta E_m} - e^{-\beta E_n}}{e^{-\beta E_m} + e^{-\beta E_n}} \\ &= \frac{W_m + W_n}{E_n - E_m} \tanh\left(\frac{\beta}{2}(E_n - E_m)\right) \\ &\leq \frac{\beta}{2}(W_m + W_n) \end{aligned} \quad (2.27)$$

In the last line, we used that $\tanh(x)/x \leq 1$ for $\forall x \in \mathbb{R}$. Now, we can estimate (\hat{A}, \hat{A}) by

$$\begin{aligned} (\hat{A}, \hat{A}) &\leq \frac{\beta}{2} \sum_{n,m}^{E_n \neq E_m} \langle n | \hat{A}^\dagger | m \rangle \langle m | \hat{A} | n \rangle (W_m + W_n) \\ &\leq \frac{\beta}{2} \sum_{n,m} \langle n | \hat{A}^\dagger | m \rangle \langle m | \hat{A} | n \rangle (W_m + W_n) \\ &\leq \frac{\beta}{2} \sum_n W_n (\langle n | \hat{A}^\dagger \hat{A} | n \rangle + \langle n | \hat{A} \hat{A}^\dagger | n \rangle) \\ &\leq \frac{\beta}{2} \langle \{\hat{A}, \hat{A}^\dagger\} \rangle. \end{aligned} \quad (2.28)$$

Substituting the Eqs. 2.24 and 2.26 as well as the inequality 2.28 into the Schwarz equation

$$(\hat{A}, \hat{A})(\hat{B}, \hat{B}) \geq |(\hat{A}, \hat{B})|^2 \quad (2.29)$$

results in the Bogoliubov inequality in the expression 2.18.

The Mermin-Wagner Theorem

The Hamiltonian of the Heisenberg model coupled to a weak magnetic field B_0 pointing in the z -direction is given by

$$\hat{H} = - \sum_{i,j} J_{ij} \hat{\mathbf{S}}_i \cdot \hat{\mathbf{S}}_j - g_J \underbrace{\frac{\mu_B}{\hbar} B_0}_{:=b} \sum_i \hat{S}_i^z e^{-i \mathbf{K} \cdot \mathbf{R}_i}, \quad (2.30)$$

where $\hat{\mathbf{S}}_i$ is the spin operator located at the lattice site \mathbf{R}_i , \hat{S}_i^z is its z -component, J_{ij} denotes the coupling constant between different sites, g_J is the Landé g -factor, and μ_B is the Bohr magneton. The factor $e^{-i \mathbf{K} \cdot \mathbf{R}_i}$ helps to differentiate between ferro- and antiferromagnetism. We choose $\mathbf{K} = 0$ for ferromagnetism; for antiferromagnetism, we choose \mathbf{K} in such a way that $e^{-i \mathbf{K} \cdot \mathbf{R}_i} = 1$ when \mathbf{R}_i connects sites of the same

sublattice and $e^{-i\mathbf{K}\cdot\mathbf{R}_i} = -1$ when \mathbf{R}_i connects sites of the other sublattice⁴³.

The magnetization with respect to the magnetic field B_0 at temperature T can be calculated by

$$M(T, B_0) = -\left(\frac{\partial \langle \hat{H} \rangle}{\partial B_0}\right)_T = g_J \frac{\mu_B}{\hbar} \sum_i e^{-i\mathbf{K}\cdot\mathbf{R}_i} \langle \hat{S}_i^z \rangle_{T, B_0}. \quad (2.31)$$

In the limit of a negligible magnetic field $B_0 \rightarrow 0$, the spontaneous magnetization is obtained:

$$M_s(T) = \lim_{B_0 \rightarrow 0} M(T, B_0) \quad (2.32)$$

In general, the spin operators can be transferred to \mathbf{k} -space by

$$\hat{S}^\alpha(\mathbf{k}) = \sum_i \hat{S}_i^\alpha e^{-i\mathbf{k}\cdot\mathbf{R}_i}, \quad \alpha \in \{x, y, z\}. \quad (2.33)$$

We introduce the ladder operators $\hat{S}_i^\pm = \hat{S}_i^x \pm i\hat{S}_i^y$ and obtain the following commutation relations:

$$\left. \begin{aligned} [\hat{S}_i^\alpha, \hat{S}_j^\beta] &= i\hbar \delta_{ij} \epsilon_{\alpha\beta\gamma} \hat{S}_i^\gamma \\ [\hat{S}_i^\alpha, \hat{S}_j^\pm] &= \hbar \delta_{ij} (\mp \delta_{\alpha x} \hat{S}_i^z - i\delta_{\alpha y} \hat{S}_i^z \pm \delta_{\alpha z} \hat{S}_i^\pm) \end{aligned} \right\} \Rightarrow \begin{aligned} [\hat{S}^+(\mathbf{k}_1), \hat{S}^-(\mathbf{k}_2)] &= 2\hbar \hat{S}^z(\mathbf{k}_1 + \mathbf{k}_2) \\ [\hat{S}^z(\mathbf{k}_1), \hat{S}^\pm(\mathbf{k}_2)] &= \pm \hbar \hat{S}^\pm(\mathbf{k}_1 + \mathbf{k}_2) \end{aligned} \quad (2.34)$$

Here, δ_{ij} is the Kronecker delta, $\epsilon_{\alpha\beta\gamma}$ is the Levi-Civita symbol, and $\alpha, \beta, \gamma \in \{x, y, z\}$.

The Bogoliubov inequality now gives an upper bound for the magnetization by choosing

$$\hat{A} = \hat{S}^-(-\mathbf{k} + \mathbf{K}) \iff \hat{A}^\dagger = \hat{S}^+(\mathbf{k} - \mathbf{K}), \quad (2.35)$$

$$\hat{C} = \hat{S}^+(\mathbf{k}) \iff \hat{C}^\dagger = \hat{S}^-(-\mathbf{k}). \quad (2.36)$$

With these relations, we can now evaluate the three expressions in the inequality. The first term is

$$\begin{aligned} \langle [\hat{C}, \hat{A}] \rangle &= \langle [\hat{S}^+(\mathbf{k}), \hat{S}^-(-\mathbf{k} + \mathbf{K})] \rangle \\ &= 2\hbar \langle \hat{S}^z(\mathbf{K}) \rangle \\ &= 2\hbar \sum_i e^{-i\mathbf{K}\cdot\mathbf{R}_i} \langle \hat{S}_i^z \rangle \\ &= \frac{2\hbar^2}{g_J \mu_B} M(T, B_0). \end{aligned} \quad (2.37)$$

In the last line, Eq. 2.31 was utilized. The second term is obtained by summation over the whole \mathbf{k} -space:

$$\begin{aligned} \sum_{\mathbf{k}} \langle \{\mathbf{A}, \mathbf{A}^\dagger\} \rangle &= \sum_{\mathbf{k}} \langle \{\hat{S}^-(-\mathbf{k} + \mathbf{K}), \hat{S}^+(\mathbf{k} - \mathbf{K})\} \rangle \\ &= \sum_{\mathbf{k}} \sum_{i,j} e^{i(\mathbf{k}-\mathbf{K}) \cdot (\mathbf{R}_i - \mathbf{R}_j)} \langle \hat{S}_i^- \hat{S}_j^+ + \hat{S}_j^+ \hat{S}_i^- \rangle \\ &= 2N \sum_i \langle (\hat{S}_i^x)^2 + (\hat{S}_i^y)^2 \rangle \\ &\leq 2N \sum_i \langle \hat{S}_i^2 \rangle \\ &= 2\hbar^2 N^2 S(S+1) \end{aligned} \quad (2.38)$$

For the third term $\langle [[\hat{C}, \hat{H}], \hat{C}^\dagger] \rangle$, we first evaluate the commutator of the Hamiltonian with the spin operator in real space:

$$[\hat{S}_m^+, \hat{H}] = - \sum_{i,j} J_{ij} \sum_{\alpha \in \{x,y,z\}} [\hat{S}_m^+, \hat{S}_i^\alpha \hat{S}_j^\alpha] - b \sum_i [\hat{S}_m^+, \hat{S}_i^z] e^{-i\mathbf{K}\cdot\mathbf{R}_i} \quad (2.39)$$

Using the Jacobi identity $[\hat{A}, \hat{B} \hat{C}] = \hat{B}[\hat{A}, \hat{C}] + [\hat{A}, \hat{B}]\hat{C}$, as well as $J_{ii} = 0$, $J_{ij} = J_{ji}$, and the commutator relations in Eq. 2.34, we obtain

$$[\hat{S}_m^+, \hat{H}] = -2\hbar \sum_i J_{im} (\hat{S}_i^+ \hat{S}_m^z - \hat{S}_i^z \hat{S}_m^+) + \hbar b \hat{S}_m^+ e^{-i \mathbf{K} \cdot \mathbf{R}_m}. \quad (2.40)$$

With this, the double commutator evaluates to

$$[[\hat{S}_m^+, \hat{H}], \hat{S}_p^-] = 2\hbar^2 \sum_i J_{ip} \delta_{mp} (\hat{S}_i^+ \hat{S}_p^- + 2 \hat{S}_i^z \hat{S}_p^z) - 2\hbar^2 J_{mp} (\hat{S}_m^+ \hat{S}_p^- + 2 \hat{S}_m^z \hat{S}_p^z) + 2\hbar^2 b \delta_{mp} \hat{S}_p^z e^{-i \mathbf{K} \cdot \mathbf{R}_p}. \quad (2.41)$$

The third term of the Bogoliubov inequality then yields

$$\begin{aligned} \langle [[\hat{C}, \hat{H}], \hat{C}^\dagger] \rangle &= \sum_{m,p} e^{-i \mathbf{k} \cdot (\mathbf{R}_m - \mathbf{R}_p)} \langle [[\hat{S}_m^+, \hat{H}], \hat{S}_p^-] \rangle \\ &= 2\hbar^2 \sum_{m,p} J_{mp} (1 - e^{-i \mathbf{k} \cdot (\mathbf{R}_m - \mathbf{R}_p)}) \langle \hat{S}_m^+ \hat{S}_p^- + 2 \hat{S}_m^z \hat{S}_p^z \rangle + 2\hbar^2 b \sum_p \underbrace{\langle \hat{S}_p^z \rangle e^{-i \mathbf{K} \cdot \mathbf{R}_p}}_{= B_0 M(T, B_0)}. \end{aligned} \quad (2.42)$$

Evaluating Eq. 2.42 with $\hat{C} = \hat{S}^+(-\mathbf{k})$ instead of $\hat{C} = \hat{S}^+(\mathbf{k})$ leads to the same result but with \mathbf{k} replaced by $-\mathbf{k}$. In both cases, the expectation value must be positive according to Eq. 2.26, and an upper bound for the expectation value can be given:

$$\begin{aligned} \langle [[\hat{C}, \hat{H}], \hat{C}^\dagger] \rangle &\leq 4\hbar^2 \sum_{m,p} J_{mp} (1 - \cos(\mathbf{k} \cdot (\mathbf{R}_m - \mathbf{R}_p))) \langle \hat{\mathbf{S}}_m \cdot \hat{\mathbf{S}}_p + \hat{S}_m^z \hat{S}_p^z \rangle + 4\hbar^2 B_0 M(T, B_0) \\ &\leq 4\hbar^2 \sum_{m,p} |J_{mp}| |1 - \cos(\mathbf{k} \cdot (\mathbf{R}_m - \mathbf{R}_p))| (|\langle \hat{\mathbf{S}}_m \cdot \hat{\mathbf{S}}_p \rangle| + |\langle \hat{S}_m^z \hat{S}_p^z \rangle|) + 4\hbar^2 |B_0 M(T, B_0)| \\ &\leq 4\hbar^2 \sum_{m,p} |J_{mp}| |1 - \cos(\mathbf{k} \cdot (\mathbf{R}_m - \mathbf{R}_p))| (\hbar^2 S(S+1) + \hbar^2 S^2) + 4\hbar^2 |B_0 M(T, B_0)| \\ &\leq 8\hbar^4 S(S+1) \sum_{m,p} |J_{mp}| |1 - \cos(\mathbf{k} \cdot (\mathbf{R}_m - \mathbf{R}_p))| + 4\hbar^2 |B_0 M(T, B_0)| \\ &\leq 8\hbar^4 S(S+1) \sum_{m,p} |J_{mp}| \frac{1}{2} k^2 |\mathbf{R}_m - \mathbf{R}_p|^2 + 4\hbar^2 |B_0 M(T, B_0)| \end{aligned}$$

Finally, we obtain the following inequality:

$$\langle [[\hat{C}, \hat{H}], \hat{C}^\dagger] \rangle \leq 4\hbar^4 S(S+1) N Q k^2 + 4\hbar^2 |B_0 M(T, B_0)| \quad (2.43)$$

We have defined $Q := \frac{1}{N} \sum_{i,j} |\mathbf{R}_i - \mathbf{R}_j|^2 |J_{ij}|$, which is a measure for the exchange range J_{ij} . For sufficiently fast decreasing exchange interactions, Q is finite, and the inequality 2.43 is well-defined. This is a weak criterium that allows the Mermin-Wagner theorem to hold even beyond next neighbor interactions.

We now rearrange the Bogoliubov inequality in Eq. 2.18, sum over all \mathbf{k} -points, and insert the expressions 2.37, 2.38, and 2.43:

$$\frac{1}{2} \beta \sum_{\mathbf{k}} \langle \{\hat{A}, \hat{A}^\dagger\} \rangle \geq \sum_{\mathbf{k}} \frac{|\langle [\hat{C}, \hat{A}] \rangle|^2}{\langle [[\hat{C}, \hat{H}], \hat{C}^\dagger] \rangle} \quad (2.44)$$

$$\iff \beta S(S+1) \geq \left(\frac{M(T, B_0)}{N g_J \mu_B} \right)^2 \sum_{\mathbf{k}} \frac{1}{\hbar^2 S(S+1) N Q k^2 + |B_0 M(T, B_0)|} \quad (2.45)$$

In the 1D case, we can make additional simplifications. First, the sum is replaced by an integral bounded

by the Brillouin zone k_{BZ} . In the thermodynamic limit, let furthermore $\nu = V_{\text{1D}}/N$ and $m(T, B_0) = \frac{M(T, B_0)}{N}$ be the average spacing and microscopic magnetization of the spins:

$$S(S+1) \geq \frac{\nu m^2(T, B_0)}{\pi \beta (g_J \mu_B)^2} \int_0^{k_{\text{BZ}}} \frac{dk}{\hbar^2 S(S+1) Q k^2 + |B_0 m(T, B_0)|} \quad (2.46)$$

This integral can be easily evaluated and yields

$$S(S+1) \geq \frac{\nu m^2(T, B_0)}{2\pi \beta (g_J \mu_B)^2} \frac{\arctan\left(k_{\text{BZ}} \sqrt{\frac{\hbar^2 S(S+1) Q}{|B_0 m(T, B_0)|}}\right)}{\sqrt{\hbar^2 S(S+1) Q |B_0 m(T, B_0)|}}. \quad (2.47)$$

The spontaneous magnetization is given in the limit of $B_0 \rightarrow 0$. In this case, the arctangent approaches $\frac{\pi}{2}$, and the spontaneous magnetization yields:

$$m_s(T) = \lim_{B_0 \rightarrow 0} |m(T, B_0)| \leq \text{const.} \cdot \lim_{B_0 \rightarrow 0} \frac{B_0^{1/3}}{T^{2/3}} \rightarrow 0 \text{ for } T \neq 0 \quad (2.48)$$

This inequality implies that there cannot be any ferro- or antiferromagnetic ordering for an interacting one-dimensional system at finite temperatures, which is known as the Mermin-Wagner theorem. We make a few more remarks below that are essential for the theorem:

1. The proof is also valid for a 2D system. In this case, the integral in the inequality 2.46 has a slightly different form and solution. The asymptotic behavior of the spontaneous magnetization, however, is similar.
2. The theorem holds only at finite temperatures. At zero temperature, it cannot make any predictions.
3. The inequalities 2.47 and 2.48 are independent of the factor $\exp(-i \mathbf{K} \cdot \mathbf{R}_i)$, which was introduced to also account for antiferromagnetism. Consequently, the theorem also forbids an antiferromagnetic long-range ordering.
4. The continuous symmetry of the system is mandatory for the Mermin-Wagner theorem. For instance, it can be shown that the Ising model exhibiting a discrete symmetry has a phase transition at $T = 0 \text{ K}^{46}$.
5. The theorem holds only for isotropic systems. The introduction of even very small anisotropies leads to a breakdown of the theorem. This is the reason why materials with a magnetic long-range ordering on the surface, as discussed in chapter 5, are not precluded.
6. The Mermin-Wagner theorem can be readily extended to other models, e.g., the Hubbard model⁴⁷.
7. A more intuitive approach to the Mermin-Wagner theorem is possible via a simple energy argument: For a ferromagnetic spin chain consisting of N spins, a twist by 2π can be divided into N twists by $\phi_i = \frac{2\pi}{N}$. Thus, for large N , the energy requirement of a single twist within the harmonic approximation is $E_i \propto \phi_i^2 = \frac{4\pi^2}{N^2}$, and the total energy change scales as $N \frac{4\pi^2}{N^2} \propto \frac{1}{N}$. Therefore, the energy requirement for long-wavelength excitations, i.e., $k \rightarrow 0$ in 1D, goes to 0 in 1D.

2.4 Nosé-Hoover Thermostat

In its basic formulation, density-functional theory (DFT)^{48–50} allows the calculation of ground-state properties at absolute zero. In many cases, one is interested in the static or dynamic properties, e.g., at a specific energy level or a specific temperature. *Ab initio* molecular dynamics builds upon DFT and allows one to perform simulations for systems involving the dynamics of the ions.

Integrating the Hamiltonian equations of motion leads to a microcanonical ensemble, where the dynamics of the system is constrained to an isoenergetic hyperplane. However, the properties at a particular temperature are described by the canonical ensemble, which allows for the exchange of energy with the environment. By introducing a virtual thermostat coupled to the system, we can account for energy dissipation that is needed to maintain a specific temperature.

How can a virtual thermostat be realized? For ideal gases, the average kinetic energy $\langle E_{\text{kin}} \rangle$ is related to the temperature T by⁵¹

$$\langle E_{\text{kin}} \rangle = \left\langle \sum_i \frac{1}{2} m_i \dot{\mathbf{r}}_i^2 \right\rangle = \frac{3}{2} N k_B T, \quad (2.49)$$

where m_i and $\dot{\mathbf{r}}_i$ are the mass and velocity of particle i , and N is the number of unconstrained particles in a system. Thus, the simplest and also earliest attempt of a thermostat involves scaling the particle velocities after each time step⁵². While this approach leads to a constant temperature, it does not reproduce a canonical phase-space distribution. The main problem is that in a canonical ensemble—although the average kinetic energy is constant—fluctuations around the mean are allowed. The standard deviation of the kinetic energy within the canonical ensemble yields⁵¹

$$\Delta E = \sqrt{N k_B T^2 c_V}. \quad (2.50)$$

Here, c_V is the specific heat capacity. More precisely, the temperature is a well-defined quantity only in the thermodynamic limit $N \rightarrow \infty$, and the relative standard deviation of the kinetic energy $\Delta E/E \propto N^{-1/2}$ approaches zero. For a system with a small number of particles, the kinetic energy is subject to strong fluctuations, which makes the treatment of molecular dynamics at constant temperature cumbersome.

H. C. Anderson⁵³ proposed a more sophisticated approach where at a certain frequency the velocity of random particles is stochastically changed to match the Boltzmann distribution. While this approach generates a canonical phase-space distribution, it results in a discontinuous phase-space trajectory.

S. Nosé proposed a different approach: Instead of an external or stochastic change of the particle velocities, he extended the system by an additional degree of freedom with variable s , which acts as an external system coupled to the N -particle system^{54,55}. It takes the role of a heat bath that stabilizes the temperature but allows for fluctuations in the kinetic energy. In addition, he introduced a virtual time t that is scaled by the variable s , so that $dt' = dt/s$. Consequently, the virtual positions and velocities are $\mathbf{r}_i = \mathbf{r}'_i$ and $\dot{\mathbf{r}}_i = \dot{\mathbf{r}}'_i/s$, where the primed variables t' , \mathbf{r}'_i and $\dot{\mathbf{r}}'_i$ denote the real variables. The latter relation can be interpreted as an exchange of heat between the physical and the external system⁵⁴. With this, he postulated the Lagrangian

$$L = \sum_i^N \frac{1}{2} m_i s^2 \dot{\mathbf{r}}_i^2 - \Phi(\mathbf{r}_1, \dots, \mathbf{r}_N) + \frac{Q}{2} \dot{s}^2 - \frac{g}{\beta} \ln s, \quad (2.51)$$

where $\Phi(\mathbf{r}_1, \dots, \mathbf{r}_N) = \Phi(\mathbf{r})$ is the potential of the N -particle system, and g is a constant of proportionality

whose exact value will be determined at a later point. The potential $g/\beta \ln s$ is chosen such that a canonical phase-space distribution is obtained, and the kinetic energy term $Q/2\dot{s}^2$ is introduced to construct a dynamic equation for s . The parameter Q has the dimension [energy-time²] and can be regarded as a frequency for the energy fluctuations. The associated virtual momenta \mathbf{p}_i and p_s are:

$$\mathbf{p}_i = \nabla_{\dot{\mathbf{r}}} L = m_i s^2 \dot{\mathbf{r}}_i \quad \Longleftrightarrow \quad \dot{\mathbf{r}}_i = \frac{\mathbf{p}_i}{m_i s^2} \quad (2.52)$$

$$p_s = \frac{\partial L}{\partial \dot{s}} = Q \dot{s} \quad \Longleftrightarrow \quad \dot{s} = \frac{p_s}{Q} \quad (2.53)$$

A Legendre transformation connects the Hamiltonian of the extended system to the Lagrangian, so that

$$\begin{aligned} H &= \sum_i^N \mathbf{p}_i \cdot \dot{\mathbf{r}}_i + p_s \dot{s} - L \\ &= \underbrace{\sum_i^N \frac{\mathbf{p}_i^2}{2m_i s^2} + \Phi(\mathbf{r})}_{=:H_0(\mathbf{p}/s, \mathbf{r})} + \frac{p_s^2}{2Q} + \frac{g}{\beta} \ln s. \end{aligned} \quad (2.54)$$

Based on the Hamiltonian, we obtain the following equations of motion:

$$\dot{\mathbf{r}}_i = \nabla_{\mathbf{p}_i} H = \frac{\mathbf{p}_i}{m_i s^2}, \quad \dot{\mathbf{p}}_i = -\nabla_{\mathbf{r}_i} H = -\nabla_{\mathbf{r}_i} \Phi(\mathbf{r}) \quad (2.55)$$

$$\dot{s} = \frac{\partial H}{\partial p_s} = \frac{p_s}{Q}, \quad \dot{p}_s = -\frac{\partial H}{\partial s} = \sum_i^N \frac{\mathbf{p}_i^2}{m_i s^3} - \frac{g}{\beta s} \quad (2.56)$$

While the extended system in Eq. 2.54 generates a microcanonical ensemble, we will show that the partition function of the reduced system, i.e., the subspace of variables \mathbf{r}'_i and \mathbf{p}'_i , is canonical. Neglecting prefactors, the partition function adhering to energy conservation yields

$$Z = \int d\mathbf{p}_s \int ds \int d\mathbf{p} \int d\mathbf{r} \delta \left[H_0(\mathbf{p}/s, \mathbf{r}) + \frac{p_s^2}{2Q} + \frac{g}{\beta} \ln s - E \right]. \quad (2.57)$$

We have used here the shorthand notation $d\mathbf{p} = d\mathbf{p}_1 \cdots d\mathbf{p}_N$ and $d\dot{\mathbf{r}} = d\dot{\mathbf{r}}_1 \cdots d\dot{\mathbf{r}}_N$. According to Eq. 2.52, the relation between the virtual and the real momentum is $\mathbf{p}_i = s \mathbf{p}'_i$, and thus $d\mathbf{p} = s^{3N} d\mathbf{p}'$. Furthermore, δ is the Dirac delta distribution, for which the relation $f'(s_0) \cdot \delta[f(s)] = \delta(s - s_0)$ holds. s_0 denotes the single root of $f(s)$. Eq. 2.57 can then be rewritten into

$$\begin{aligned} Z &= \frac{\beta}{g} \int d\mathbf{p}' \int d\mathbf{r}' \int d\mathbf{p}_s \int ds s^{3N+1} \delta \left[s - e^{-\frac{\beta}{g} (H_0(\mathbf{p}', \mathbf{r}') + \frac{p_s^2}{2Q} - E)} \right] \\ &= \frac{\beta}{g} e^{\beta \frac{3N+1}{g} E} \int d\mathbf{p}_s e^{-\beta \frac{3N+1}{g} \frac{p_s^2}{2Q}} \int d\mathbf{p}' \int d\mathbf{r}' e^{-\beta \frac{3N+1}{g} H_0(\mathbf{p}', \mathbf{r}')} \\ &= \frac{\sqrt{2\pi\beta Q}}{(3N+1)} e^{\beta E} \underbrace{\int d\mathbf{p}' \int d\mathbf{r}' e^{-\beta H_0(\mathbf{p}', \mathbf{r}')}}_{\propto Z_c}. \end{aligned} \quad (2.58)$$

In the last line, we have set $g = 3N + 1$. By this choice, the partition function of the reduced system is equivalent to the partition function of the canonical ensemble Z_c except for a constant prefactor. As a consequence, the expectation values of a quantity O averaged by the canonical ensemble and by the Nosé ensemble are identical. The latter is connected to the time average by the ergodic hypothesis, so that

$$\lim_{t_0 \rightarrow \infty} \frac{1}{t_0} \int_0^{t_0} dt O(\mathbf{p}', \mathbf{r}') = \langle O(\mathbf{p}', \mathbf{r}') \rangle_c = \langle O(\mathbf{p}/s, \mathbf{r}) \rangle_{\text{Nosé}}. \quad (2.59)$$

While the approach of Nosé is well suited to calculate averages of static quantities, the implicit varying time steps dt in the Eqs. 2.55 – 2.56 lead to errors in the case of dynamic quantities. The size of the error depends on the chosen Q and the typical time scale with which the quantity changes⁵⁴. Eqs. 2.55 – 2.56 can be rewritten in terms of real variables (with $dt' = dt/s$, $\mathbf{r}'_i = \mathbf{r}_i$, $\mathbf{p}'_i = \mathbf{p}_i/s$, $s' = s$, and $p'_s = p_s/s$):

$$\dot{\mathbf{r}}'_i = s \frac{d\mathbf{r}_i}{dt} = s \frac{\mathbf{p}_i}{m_i s^2} = \frac{\mathbf{p}'_i}{m_i} \quad \dot{\mathbf{p}}'_i = s \frac{d}{dt} \left(\frac{\mathbf{p}_i}{s} \right) = -\nabla_{\mathbf{r}_i} \Phi(\mathbf{r}) - \dot{s} \frac{\mathbf{p}_i}{s} = -\nabla_{\mathbf{r}'_i} \Phi(\mathbf{r}') - \frac{s' p'_s}{Q} \mathbf{p}'_i \quad (2.60)$$

$$\dot{s}' = s \frac{ds}{dt} = \frac{s'^2 p'_s}{Q} \quad \dot{p}'_s = s \frac{d}{dt} \left(\frac{p_s}{s} \right) = \sum_i^N \frac{\mathbf{p}'_i^2}{m_i s'} - \frac{g}{\beta s'} - \frac{s' p'_s^2}{Q} \quad (2.61)$$

While these equations recover equidistant time steps, they have no Hamiltonian form, as is evident from the additional force terms for the momenta that lead to the nonvanishing derivatives $\nabla_{\mathbf{p}'_i} \cdot \dot{\mathbf{p}}'_i$ and $\partial \dot{p}'_s / \partial p'_s$.

W. G. Hoover⁵⁶ further simplified these equations by introducing the thermodynamic friction coefficient $\zeta' = \ln s'$, so that

$$\dot{\zeta}' = \frac{\dot{s}'}{s'} = \frac{s' p'_s}{Q} = \frac{p_s}{Q} \quad \text{and} \quad p'_\zeta = \dot{\zeta}' Q = p_s. \quad (2.62)$$

Eqs. 2.60–2.61 then become independent of s' by rewriting them in terms of $\dot{\mathbf{r}}'_i$ and $\ddot{\mathbf{r}}'_i$ as well as $\dot{\zeta}'$ and $\ddot{\zeta}'$:

$$\ddot{\mathbf{r}}'_i = \frac{\dot{\mathbf{p}}'_i}{m_i} = -\frac{\nabla_{\mathbf{r}'_i} \Phi(\mathbf{r}')}{m_i} - \frac{s' p'_s}{Q} \frac{\mathbf{p}'_i}{m_i} = -\frac{\nabla_{\mathbf{r}'_i} \Phi(\mathbf{r}')}{m_i} - \dot{\zeta}' \dot{\mathbf{r}}'_i \quad (2.63)$$

$$\ddot{\zeta}' = \frac{1}{Q} [s' p'_s + s' \dot{p}'_s] = \frac{1}{Q} \left[\frac{s'^2 p'_s^2}{Q} + \sum_i^N \frac{\mathbf{p}'_i^2}{m_i} - \frac{g}{\beta} - \frac{s'^2 p'_s^2}{Q} \right] = \frac{1}{Q} \left[\sum_i^N m_i \dot{\mathbf{r}}'_i^2 - \frac{g}{\beta} \right]. \quad (2.64)$$

These equations are known as the Nosé-Hoover equations. They can be used to calculate the dynamics of the ions, e.g., within the Born-Oppenheimer approximation⁵⁷.

As before, we will show that the equations of motion generate a canonical ensemble. Because the phase space is a symplectic geometry, we must integrate over the variables leading to Hamiltonian equations of motion. Liouville's theorem⁵⁸ is satisfied only for these variables, which states that the phase-space density is constant along the trajectory that follows the equations of motion⁵¹. Here, ζ' , p'_ζ , \mathbf{r}_i and \mathbf{p}_i lead to Hamiltonian equations of motion. We use $d\mathbf{r} = d\mathbf{r}'$ and $d\mathbf{p} = e^{3N\zeta'} d\mathbf{p}'$, so that

$$\begin{aligned} Z &= \int d\mathbf{p}' \int d\mathbf{r}' \int dp'_\zeta \int d\zeta' e^{3N\zeta'} \delta \left[H_0(\mathbf{p}', \mathbf{r}') + \frac{p'_\zeta^2}{2Q} + \frac{g}{\beta} \zeta' - E \right] \\ &= \frac{\beta}{g} e^{\beta \frac{3N}{g} E} \int dp'_\zeta e^{-\beta \frac{3N}{g} \frac{p'_\zeta^2}{2Q}} \int d\mathbf{p}' \int d\mathbf{r}' e^{-\beta \frac{3N}{g} H_0(\mathbf{p}', \mathbf{r}')} \\ &= \frac{\sqrt{2\pi\beta Q}}{3N} e^{\beta E} \underbrace{\int d\mathbf{p}' \int d\mathbf{r}' e^{-\beta H_0(\mathbf{p}', \mathbf{r}')}}_{\propto Z_c} \end{aligned} \quad (2.65)$$

If we set $g = 3N$ —as was done in the last line—we obtain a partition function that is canonical.

Please note that we have used ζ' only for the construction of the Hamiltonian. The relevant parameter is $\dot{\zeta}'$, whose dynamics is governed by Eq. 2.64 and depends on twice the difference of the instantaneous and average kinetic energy at temperature T . Furthermore, only energy conservation was assumed to derive the partition function in Eqs. 2.57 and 2.65. For a second constraint, an additional degree of freedom needs to be introduced by coupling a second external system to the first in the same way as the first was coupled to the N -particle system in Eq. 2.54. In this way, we can create a chain of Nosé-Hoover equations to account for the conservation of momentum and angular momentum or other constraints⁵⁹.

The atoms may be compared to the letters of the alphabet, which can be put together into innumerable ways to form words. So the atoms are combined in equal variety to form what are called molecules [and crystals].

William Henry Bragg

3

Self-Assembled Au Atomic Wires on Vicinal Si(111) Surfaces

Although one-dimensional systems can be sufficiently described in theory, it soon became evident that the observation of 1D phenomena predicted by Luttinger liquid theory^{7,8} presents its own challenges. This is mainly due to the inherent Peierls instability⁹ that destabilizes ideal 1D systems, such as free-standing atomic wires. For this reason, a substrate is required on which the 1D system can be deposited. On the one hand, a suitable substrate must prevent a Peierls-induced clustering of the delicate 1D structure. This requires close structural coupling of the substrate with the 1D system. On the other hand, electronic separation of both systems is crucial to preserve the 1D character. The key idea is to use substrate materials with large-enough band gaps, such as insulators or wide-band gap semiconductors. Ideally, the metallic states of the 1D material then lie within the band gap and are electronically decoupled from the substrate. In reality, however, the situation is more complicated: Surface reconstructions of insulators or semiconductors tend to introduce surface states near the Fermi energy, sometimes even rendering the surface metallic. Therefore, finding compatible 1D systems and substrates is challenging and complicates the observation of pure 1D effects in nature.

3.1 Silicon Surfaces

With a band gap of 1.1 eV⁶⁰, silicon is by no means considered a wide-band gap semiconductor. However, it exhibits other beneficial properties: First, Si is abundantly available on Earth: 15% of the entire Earth and 27% of the Earth's crust consist of Si by weight⁶¹. Second, Si is the most researched and best-understood semiconductor. The vast majority of the integrated circuits used in present-day technology are based on silicon. In terms of application, a silicon-based 1D system would therefore be beneficial.

Si(111) is, together with Si(001), the technological most relevant Si surface. As previously mentioned, surface states are likely to narrow the bulk band gap, and this is especially true for Si(111) and Si(001). The Si(001) surface is stabilized by the formation of Si dimers⁶². Buckling of these dimers with alternating

registry reduces the surface energy and preserves the non-metalllicity of the surface⁶³. Consequently, all dangling bonds (DBs) on Si(001) are either completely filled or empty. Despite the non-metallic character, the surface states narrow the band gap considerably⁶⁴. Although electrical conductance measurements reveal a metallic temperature dependence, its magnitude is below the universal conductance quantum⁶⁵. However, details depend on the substrate doping and on the amount of adsorbed hydrogen⁶⁴.

Several surface reconstructions exist for the clean Si(111) surface. The (7×7) and $(\sqrt{3} \times \sqrt{3})$ reconstruction are the most prominent⁶⁶. Both surface reconstructions are conductive, with the former having a noticeably lower resistance⁶⁷. Electronic decoupling seems difficult to realize for both Si(111) and Si(001) unless substantial surface reconstructions accompany the formation of 1D structures. Indeed, the realization of 1D systems on Si surfaces exhibiting Luttinger liquid behavior has proven to be challenging^{68,69}.

However, Si surfaces have another advantage concerning the fabrication of 1D structures: Many metals self-assemble into atomic wires on these surfaces under controlled ambient conditions. Self-assembly significantly facilitates the fabrication of 1D structures. Other techniques, such as atom deposition by scanning tunneling microscopy (STM) tips, are not feasible for larger systems. Si(111), in particular, tends to break its three-fold symmetry and forms anisotropic structures for many metals⁷⁰: For instance, In^{71–75} and Au^{76–80} self-assembles into large arrays of parallel-aligned atomic wires. The same holds for Ag^{81–83}, Pb^{84,85}, and Ca⁸⁶ on vicinal Si(111) surfaces. But also on Si(001), atomic wires of rare earth metals form^{87–89}.

One significant difference between Si(111) and Si(001) is the number of DBs per Si surface atom. For Si(001), every surface atom has two broken bonds, while for Si(111), only a single broken bond exists per surface atom. Generally, a high density of unsaturated bonds renders a surface more reactive and facilitates the adsorption of molecules and other adsorbents⁹⁰. The sticking factor of H₂O, e.g., is close to one for Si(001), while water molecules are more likely to be repelled by the Si(111) surface⁹⁰. Another example is the formation of a μm -thick oxide layer upon O₂ exposure: Si(001) exhibits a lower activation barrier for molecular O₂ adsorption⁹¹—although surface reconstructions also play a dominant role⁹².

A similar trend can be observed concerning self-assembled atomic wires: On Si(001), rare earth wires are incorporated into the surface and covered by a layer of Si atoms⁸⁹. On Si(111), on the other hand, the self-assembled atomic wires are integrated into the top surface layer^{10,80}. In principle, buried atomic wires should be less prone to oxidation or the influence of other adsorbents such as water or hydrogen. However, an embedding in the substrate bears the risk of a tighter coupling to the substrate. In addition, experimental measurements are becoming more complicated: Many experimental methods, such as STM, are surface sensitive. These are no longer applicable or only allow indirect conclusions. Having this in mind, the properties of surface atomic wires are easier examined and should be less coupled to the substrate.

Nevertheless, even with surface atomic wires, the electronic coupling to the substrate is not negligible in most cases. Moreover, the interaction of adjacent wires may have an additional negative impact on the one-dimensionality. As a result, the dimensionality of such wire systems is a fraction between one and two. These systems are called *quasi-one-dimensional*, indicating their dependence on the substrate.

Although Luttinger liquids have not yet been observed on silicon substrates, the loose coupling of many quasi-1D wires is still accompanied by a plethora of interesting properties. Only one shall be mentioned here: Indium wires on Si(111) exhibit a second-order metal-insulator phase transition, which can be triggered by very short laser pulses. The resulting phase transition is considered the fastest switch seen in nature so far⁷⁴.

3.2 Au on Si(111)

In general, silicon and gold are immiscible, i.e., there are no known Si-Au compounds that form stable crystalline bulk phases^{93,94}. However, a variety of Au surface reconstructions exist on Si(111). Depending on the amount of evaporated Au and the ambient conditions, different phases form on the surface.

Bishop and Rivière were the first to discover the Si(111)-(5 × 2)-Au reconstruction in 1969⁷⁶. At substrate temperatures above 400 °C, the (7 × 7) low-energy electron diffraction (LEED) spots of the clean Si(111) surface transform into sharp (5 × 1) spots and diffuse second-order streaks upon Au deposition^{77,78}. Alternatively, the sample can be flash-annealed after room-temperature growth. The (5 × 2) reconstruction is characterized by islands of self-aligned parallel Au atoms, forming atomic wires. Between these wires, the Si surface atoms arrange in honeycomb ribbons, i.e., in flat graphene-like layers of sp^2 -bonded Si atoms^{79,80}. Although generally unstable, the Au atoms, which act as donors, stabilize the honeycomb ribbon, also called the honeycomb chain (HCC).

It was generally proposed that any monovalent, divalent, or trivalent adsorbent stabilizes such an HCC on Si(111) by electron donation^{95,96}. Indeed, similar structures have been observed, e.g., for Li, Na, Rb, or Ag^{97,98}. The HCC matches the substrate lattice in the direction parallel to the chains. At the same time, a lattice mismatch perpendicular to the chains limits the width of the HCC. As a consequence, the HCCs form equidistant rows separated by the Au chains, resulting in a (5 × 2) surface lattice.

The atomic chains form islands with different orientations. These originate in the three-fold symmetry of the unreconstructed Si(111) surface^{99,100}. Step edges on the imperfect Si(111) surface serve as natural guides for the wire formation¹⁰¹. The introduction of artificial steps thus achieves a more uniform alignment. These can be created systematically by cutting the Si(111) surface at an acute angle. The resulting terraces guide the wire formation along the step edges¹⁰². As a result, a uniform area of parallel wires form.

3.2.1 Au on Vicinal Si(111) Surfaces

A slightly miscut surface also has other advantages: It introduces terraces that serve as nucleation sites for single atomic chains. For not too broad terraces, the interwire distance is then governed by their width. As previously mentioned, interwire interactions of closely spaced chains may strongly influence the system. An increased spacing of the wires could thus reduce the interwire interaction. Si(111) surfaces miscut towards [112] or [112] result in Si(hhk) surfaces with uniform step edges and evenly spaced terraces¹⁰. The Au wires adsorb preferentially in the middle of the vicinal Si(111) terraces. Their width b_{ter} and height h_{ter} determine the interwire distance

$$d_{\text{ter}} = \sqrt{b_{\text{ter}}^2 + h_{\text{ter}}^2}. \quad (3.1)$$

The Miller indices (hhk) define b_{ter} and h_{ter} by¹⁰³

$$b_{\text{ter}}(h, k) = \frac{2h + k}{3} \sqrt{\frac{3}{8}} a_0 \quad \text{and} \quad h_{\text{ter}}(h, k) = \frac{|h - k|}{2\sqrt{3}} a_0, \quad (3.2)$$

where $a_0 = 5.431 \text{ \AA}$ is the lattice constant of the underlying Si surface in the [110] direction¹⁰⁴.

Fig. 3.1 illustrates the family of Si(hhk) surfaces. Most of these vicinal Si(111) surfaces are unstable in the absence of metallic donors, such as Au¹¹. Instead of regularly stepped surfaces, (7 × 7) reconstructions

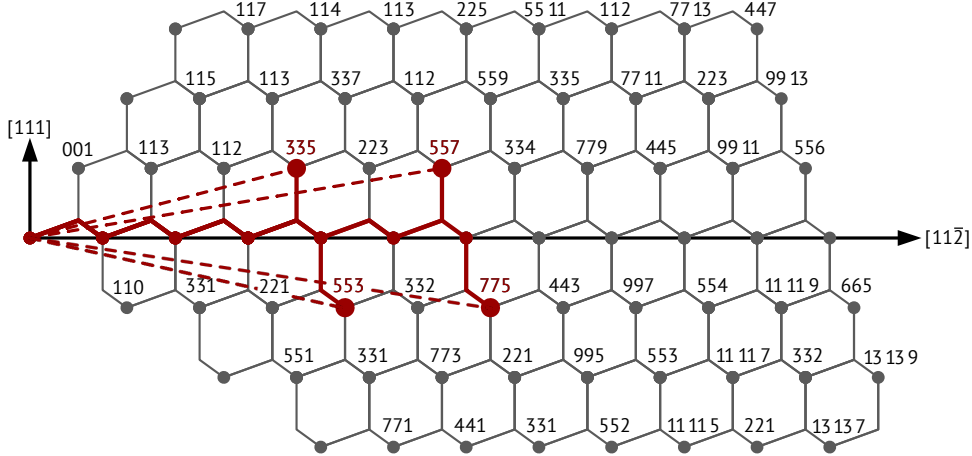


Figure 3.1: Sidecut of the silicon crystal in the $[1\bar{1}0]$ direction. The solid horizontal line indicates the Si(111) surface. If tilted towards $[1\bar{1}2]$ or $[\bar{1}12]$, Si($h\bar{h}k$) surfaces arise. The indices mark the orientation of these surfaces. The dashed red lines illustrate the cutting planes of the (335), (557), (553), and (775) surfaces, while the solid red lines represent the surface structures of the perfect, unreconstructed surfaces (adapted from Ref. [10]).

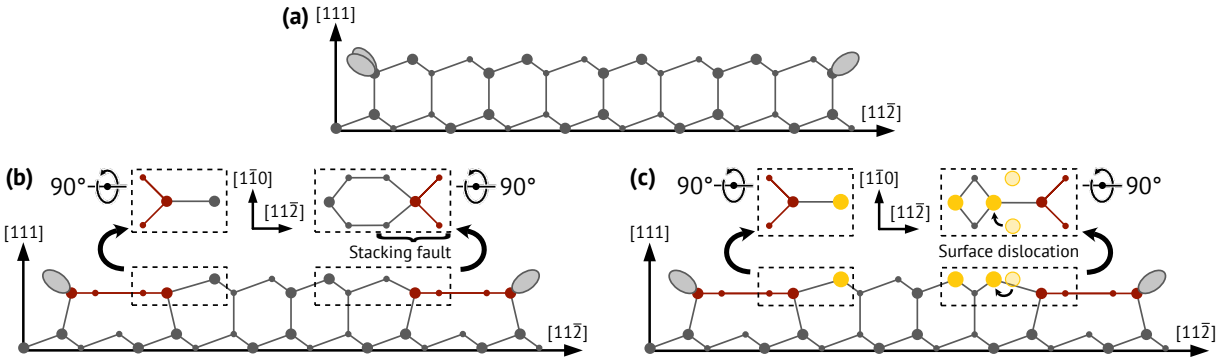


Figure 3.2: Step edges of vicinal Si(111) surfaces for positive (left edges) and negative (right edges) cutting angles. Big and small dark gray circles indicate Si atoms of different depth along $[1\bar{1}0]$, while light gray ellipses illustrate DBs of the step-edge atoms. (a) The unreconstructed step edge has two (one) DBs per step-edge atom for surfaces with positive (negative) orientation. (b) The HCC reconstruction (red) stabilizes the step edge, resulting in a single DB per step-edge atom for both orientations. For negative cutting angles, a stacking fault occurs between the HCC and the remaining Si surface atoms. The upper dashed boxes show the Si surface atoms along the $[111]$ direction. (c) The adsorbed Au atoms (yellow circles) replace Si surface atoms next to the HCC. Depending on the orientation, a single-strand or double-strand Au chain forms. A surface dislocation within the Au chain (yellow transparent circles) repairs the stacking fault for negative cutting angles.

appear on differently sized terraces¹⁰⁵. In the case of Au wires, the deposition of Au and subsequent heating to temperatures above 400 °C stabilizes the vicinal Si(111) surfaces. As a result, regular-sized terraces form. However, only Si($h\bar{h}k$) surfaces with odd Miller indices were found to be stable¹⁰.

The lack of symmetry along the $[11\bar{2}]$ direction results in two different types of step edges: For a negative ($h > k$) and positive ($h < k$) surface orientation, the step-edge atoms of the unreconstructed surface have one and two DBs, respectively, as illustrated in Fig. 3.2(a). The mirror-symmetric HCC reconstruction stabilizes the step edge by reducing the number of DBs on the surface. Furthermore, both types of step edges then share the same geometry with a single DB per step-edge atom (see Fig. 3.2(b)). However, this results in a stacking fault at the interface of the HCC and the remaining Si surface atoms in the case of negative cutting angles¹⁰⁶. The stacking fault necessitates the formation of a double-strand Au chain: First, the Au atoms substitute the Si atoms at the interface. Second, a surface dislocation within the double-strand Au

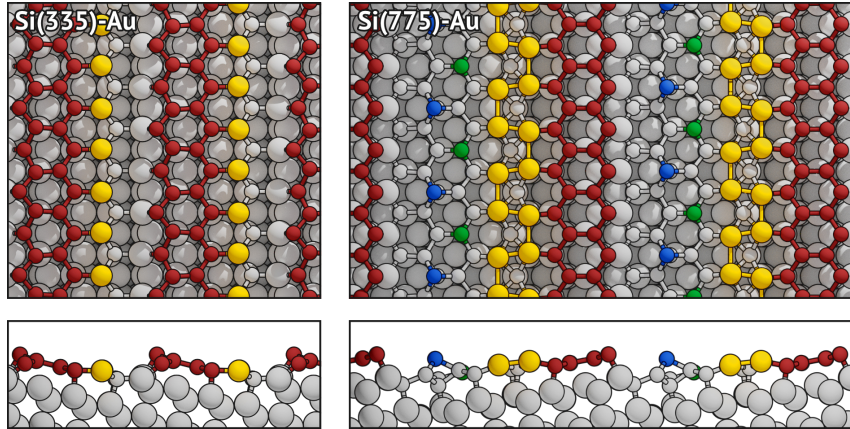


Figure 3.3: Atomic structures of Si(335)-Au¹⁰⁷ and Si(775)-Au¹⁰⁸ in top and side view. Big and small gray circles as well as red circles indicate Si bulk and Si HCC atoms, respectively. Additional green and blue circles represent Si rest atoms (having one unsaturated DB) and Si adatoms, while yellow circles mark the positions of the Au atoms.

chain repairs the stacking fault previously felt by the substituted Si atoms and the adjacent HCC atoms. The spherical s -orbitals of the Au atoms are less sensitive to specific bonding geometries than the more rigid sp -hybridized Si atoms. In contrast, the bonding geometry of the HCC and Si surface atoms match for surfaces with positive orientation. Consequently, only a single-strand Au chain is needed on these surfaces. In this sense, the Au chain stabilizes the HCC by electron donation—similar to Si(111)-Au—and corrects the stacking fault for surfaces of negative orientation.

Si(335)-Au¹⁰ and Si(553)-Au¹¹⁰ are the smallest vicinal Si(111) surfaces whose terraces can fit an HCC together with a single- and double-strand Au chain, respectively. Two other prominent Si(hhk)-Au surfaces are Si(557)-Au¹¹ and Si(775)-Au¹⁰. These have two additional rows of Si surface atoms per terrace with unsaturated DBs—called *rest atoms*. On both surfaces, additional Si adatoms saturate three out of four DBs of these rest atoms¹⁰⁸. The atomic structures of Si(335)-Au and Si(775)-Au are depicted in Fig. 3.3. A detailed summary of the terrace width, the cutting angle, and the amount of Au required for the self-assembly of Au nanowires on (vicinal) Si(111) surfaces is given in Tab. 3.1.

The following sections give a detailed, chronological overview of Si(553)-Au and a shorter overview of Si(557)-Au. In this way, outdated results are also summarized and put into perspective. This is all the more important as some results are seemingly contradicting each other, while the reasons for this are meanwhile understood to a large extent. Several overview papers^{29,36,41} have already been published, on which the following sections are partially based.

Orientation	Terrace width (Å)	Au coverage (ML)	Off-axis angle
Si(111)-(5 \times 2)	16.7	0.70 ⁸⁰	0°
Si(335)	12.6	0.27	14.4° to [112]
Si(557)	19.2	0.18	9.5° to [112]
Si(553)	14.8	0.48 ¹¹¹	12.3° to [112]
Si(775)	21.3	0.32 ¹⁰⁵	8.5° to [112]
Si(995)	26.3	0.13	13.8° to [112]
Si(13 13 7)	37.8	0.30	14.4° to [112]

Table 3.1: The terrace width, Au coverage, and off-axis angle for several vicinal Si(111)-Au surfaces. The Au coverages are in units of Si(111) monolayer (ML). Unless otherwise indicated, all data were taken from Ref. [10].

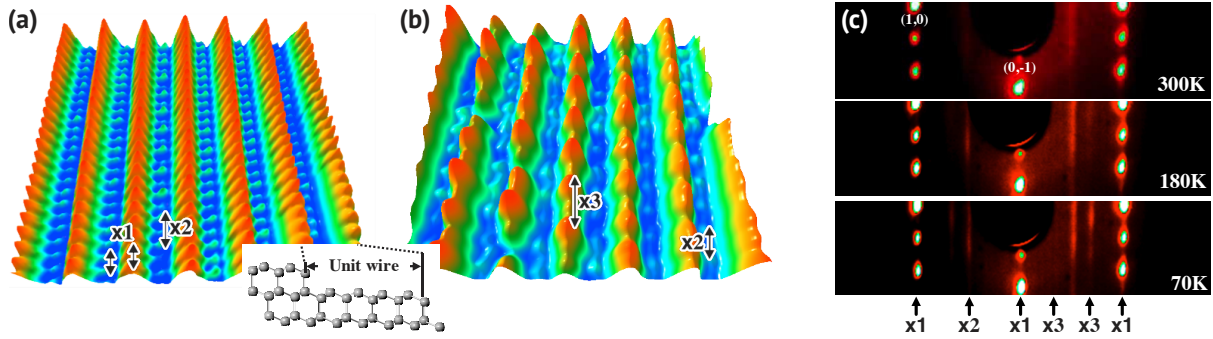


Figure 3.4: STM images of Si(553)-Au at (a) 300 K and (b) 45 K taken at -0.2 V and -0.5 V biases, respectively. The inset depicts the unreconstructed Si(553) surface. (c) LEED patterns of Si(553)-Au at 300 K, 180 K, and 70 K measured with an electron beam energy of 88 eV. Reprinted figures with permission from Ref. [112]. Copyright (2005) by the American Physical Society.

3.3 Au on Si(553)

Of all the Si(hhk)-Au surfaces, Si(553)-Au has been the most researched. This is for two reasons: First, it has the lowest defect concentration and is thus the most undisturbed quasi-1D system with Au wires^{10,109}. Second, the experimental results concerning the phase transition of Si(553)-Au seem to be in parts contradictory¹⁶. It has, therefore, the least understood dynamic behavior, which spurred further investigations.

3.3.1 Atomic Structure

The Si(553)-Au surface has an inclination angle of 12.3° towards $[1\bar{1}\bar{2}]$. Its terraces are $4\frac{1}{3}$ Si(111) surface unit cells wide—the narrowest of all Au-decorated vicinal Si(111) surfaces with negative orientation. For that reason, the Au chain separation is even smaller than for Si(111)-(5 \times 2)-Au. The atomic wires formed by 0.48 monolayer (ML) of Au (with respect to the Si surface atom density of the Si(111) surface) are distributed very homogeneously over the surface when heated to 650 °C. Subsequent flash-annealing for several seconds at 850 °C reduces the defect concentration even further¹⁰. The defect concentration of well-prepared surfaces is estimated to be in the order of 1%¹⁰⁹.

First Structural Models

The surface has been thoroughly investigated by STM^{10,103,110–121}. Parallel aligned rows of bright protrusions alternate with dark trenches, in which subtle structures are visible. These two different features are associated with the Si step edges and the Au atomic wires, respectively¹⁰. The bright protrusions are occasionally interrupted by defects, which appear as dark spots at both negative and positive tunneling biases. For the latter, these are larger^{122,123}. Fig. 3.4 depicts filled-state STM images of Si(553)-Au by topographs. Please note that in most literature the STM images are illustrated by 2D colormaps.

At room temperature, the step edge has a simple $\times 1$ periodicity (with respect to the unreconstructed (5 \times 1) unit cell of Si(553))¹¹⁰. In contrast, the faint structure associated with the Au chain exhibits a weak $\times 2$ periodicity¹⁰ (cf. Fig. 3.4(a)). Upon cooling, the $\times 2$ modulation gains intensity¹¹². More importantly, there is a period tripling at the step edge, as shown in Fig. 3.4(b). However, the onset of this tripling depends sensitively on the defect density: Defects tend to pin the $\times 3$ superstructure locally and shift the transition temperature to higher regimes¹¹³. Based on LEED, a transition temperature of 160 K was proposed for the period tripling¹²⁴.

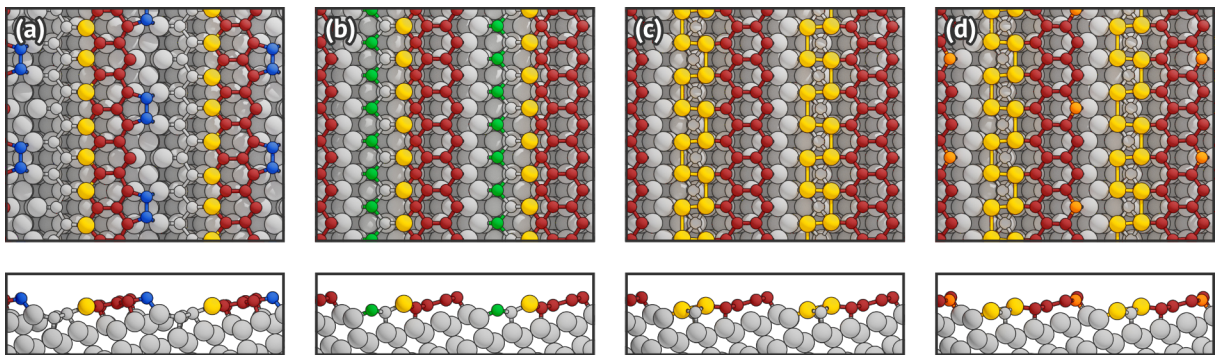


Figure 3.5: Historical development of the structural model of Si(553)-Au in top and side view. The color code is similar to Fig. 3.3. (a) The earliest surface structure¹⁰ exhibits a single Au strand, a deformed HCC, and Si adatom dimers, which account for the $\times 3$ periodicity seen in LEED. (b) A regular HCC without Si adatom dimers is energetically more stable¹⁰⁶, but higher periodic structural features are missing. (c) The discovery of a higher Au coverage led to a new model¹²⁶ with a double-strand Au chain and no Si rest atoms. The Au atoms form dimers, which account for $\times 2$ periodic features. (d) In the latest model, every third step-edge atom (orange circles) is spin-polarized and slightly lowered in position. This reflects the $\times 3$ periodicity observed in experiments^{13,120}.

Initially, Snijder *et al.* reported an additional $\times 2$ periodicity at the step edge for intermediate temperatures in STM¹¹³. However, electron injection through the STM tip was identified to induce the structural change^{118,119}. Surprisingly, the coprime $\times 3$ and $\times 2$ periodicities of the step edge and Au chain seem uncorrelated. In LEED, only a weak $\times 2$ and an even fainter $\times 3$ pattern in conjunction with the $\times 1$ pattern of the substrate are visible^{112,120,125} (cf. Fig. 3.4(c)). An additional $\times 6$ superstructure is missing.^a Au chains of adjacent terraces have no fixed arrangement with respect to each other, as is visible by the $\times 2$ streaks.

Based on early STM measurements at room temperature^{10,110,112,113}, a Au coverage of 0.24 ML was proposed, implying a single Au strand per terrace for Si(553)-Au. With this knowledge, structural models were developed using density-functional theory (DFT). A first proposal¹⁰ comprised a single-row Au chain in the middle of the terrace and a partially deformed HCC at the step edge. An additional Si dimer is attached to the step edge, which accounts for the $\times 3$ periodicity seen in experiments. The structural model is illustrated in Fig. 3.5(a). Nevertheless, the model lacks $\times 2$ structural features. Riikonen *et al.* conducted a detailed analysis of several structures¹⁰⁶. They found that Si dimers at the step edge have only a minor impact on the total energy. Furthermore, a much simpler structure with a regular HCC at the step edge is energetically more stable but misses both $\times 2$ and $\times 3$ periodic features (see Fig. 3.5(b)).

Double-Strand Au Chain

Based on X-ray diffraction (XRD) experiments, Ghose *et al.*¹²⁷ proposed a higher Au coverage of 0.48 ML. One way to accommodate the increased number of Au atoms is a double-strand Au chain. Furthermore, they suggested that an additional Si adatom row could explain the $\times 2$ periodicity seen in STM. Typically, Si adatoms appear as bright spots in STM on other Si surfaces¹²⁸. On Si(553)-Au, however, these characteristic bright spots are missing. Additionally, the Au chain of the proposed model resides at the step edge—in contrast to previous models. Later, total-energy calculations found that the atomic structure is energetically unstable^{114,129}. However, subsequent STM measurements calibrated with respect to the better understood Si(557)-Au system confirmed a Au coverage of 0.48 ML¹¹¹.

^aPolei *et al.*^{118,119} demonstrated that high-tunneling currents in STM are capable of inducing a $\times 6$ superstructure. Later it was shown that a $\times 6$ periodicity is also visible in high-resolution STM images—Independent of the electrical current¹²¹. For more details, see section 3.3.2.

Krawiec incorporated these findings into a new model¹²⁶, shown in Fig. 3.5(c). This model exhibits a double-strand Au chain, where the Au atoms arrange in a *ladder* structure. This is energetically more favorable than a *zigzag* chain, where the Au atoms would merely substitute Si surface atoms. In contrast, the formation of the ladder structure involves a surface dislocation that intrinsically resolves the stacking fault caused by the HCC reconstruction (cf. Fig. 3.2 and the accompanying text). The Au atoms within a strand form dimers, which explains the $\times 2$ periodicity seen in the experiments. However, this model cannot reproduce the $\times 3$ periodicity seen at the step edge at low temperature (LT).

Spin Chain Model

An explanation for the $\times 3$ periodicity was given only a little later¹³: According to DFT calculations, every third Si step-edge atom of the HCC is spin-polarized. In addition, these atoms have a slightly lower position of about 0.3 Å, as illustrated in Fig. 3.5(d). This leads to a $\times 3$ periodic structure at the step edge, which explains the patterns seen in LEED and STM at LT. Hafke *et al.*¹²⁰ further noted that the spot-profile analysis LEED (SPA-LEED) data indicates a centered geometry with respect to the spin-polarized step-edge atoms. The associated primitive surface unit cell exhibits an inherent higher symmetry, and step-edge atoms of adjacent terraces have a fixed relation.

Although the spin-chain (SC) structure provides a decent match with empty state STM images at higher tunneling biases, not all features are reproduced for lower biases. A detailed comparison of experimental with calculated STM images of the SC structure, together with a new model proposal, is discussed in detail in chapter 5.

Low-Coverage Wire Phase

The deposition of 0.2 ML Au on Si(553) results in the formation of low-coverage wires—in contrast to the high-coverage wires with 0.48 ML Au¹³⁰. This phase is characterized by two alternating terraces with different surface reconstructions and widths of $4\frac{1}{3} a_0$ and $5\frac{1}{3} a_0$, where a_0 denotes the width of a Si(111) surface unit cell. The smaller one is identical to the high-coverage terrace exhibiting a Au chain and an HCC at the step edge. However, every other terrace is a pure Si surface with elements of the Si(111)-(7 \times 7) structure. As the terrace width is limited, only parts of the (7 \times 7) reconstruction form on these terraces. The total width of both terraces is $9\frac{2}{3} a_0 = 32.7$ Å, which is slightly larger than two Si(553)-Au terraces. Therefore, the low-coverage phase ideally forms on a Si(11 11 7) surface with an inclination angle of 11°. Step bunching accounts for the orientation mismatch of approximately 1.2° to the Si(553) surface¹³⁰.

The alternating terraces appear in LEED as $\times 2$ reflexes in the direction perpendicular to the steps. In the chain direction, additional $\times 5$ spots occur compared to the high-coverage phase. According to the structure model shown in Fig. 3.6, this $\times 5$ periodicity is due to the *dimer-adatom-stacking-fault* structure known from the Si(111)-(7 \times 7) surface⁶⁶. The Si terrace exerts significant strain on the Au terrace. Consequently, the HCC step edge adopts the $\times 5$ periodicity of the dimer-adatom-stacking-fault, as seen in STM for empty states. Moreover, the 1D band structure, the metallic carrier density, and its velocity are modified as well¹³⁰.

The low-coverage phase is mentioned here for the sake of completeness. In this dissertation, only the high-coverage phase is investigated. Therefore, the high-coverage phase of Si(553)-Au will be simply referred to as Si(553)-Au in the following.

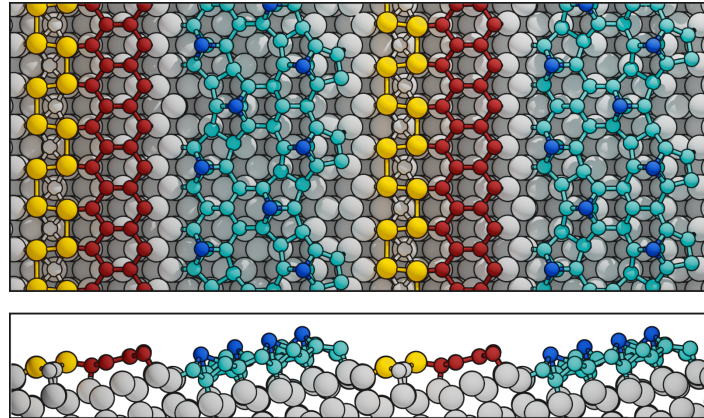


Figure 3.6: Structural model of the low-coverage wires of Si(553)-Au in top and side view. The color code is similar to Fig. 3.3. Light and dark blue circles indicate the dimer-adatom-stacking-fault structure known from the Si(111)-(7 \times 7) surface.

3.3.2 Electronic Structure

Band Structure and Dimensionality

The band structure of Si(553)-Au was investigated by means of angle-resolved photoemission spectroscopy (ARPES)^{10,112}: Similar to other vicinal Si(111)-Au surfaces, Si(553)-Au exhibits a doublet of bands, labeled S_1 and S_2 . These have fractional fillings of $0.51 e$ and $0.56 e$. Additionally, a third band (S_3) with a lower band filling of $0.27 e$ is observed, as shown in Fig. 3.7. These bands originate in the hybridized states of gold and adjacent silicon atoms. Their minima are located at the Brillouin zone (BZ) boundary of the (5 \times 1) unit cell. Furthermore, they show a large dispersion in the direction parallel to the Au chain but little to no dispersion in the orthogonal direction. This agrees with the measured Fermi surface, which appears as two parallel lines in the experiment¹⁰. However, small modulations of these lines suggest non-negligible interwire coupling, which is indicative of quasi-1D systems.

A detailed tight-binding analysis¹⁰ of the ARPES data gives a quantitative measure of the ratio between intrawire and interwire coupling t_{\parallel}/t_{\perp} . For the S_1 and S_2 doublet of bands, the ratios are 46 and 38, whereas the S_3 band has a smaller ratio of about 12. As expected, the hopping ratio of Si(553)-Au is lower compared to other Au-decorated vicinal Si(111) surfaces with greater terrace widths. For instance, the hopping ratio of Si(775)-Au is $t_{\parallel}/t_{\perp} > 100$.

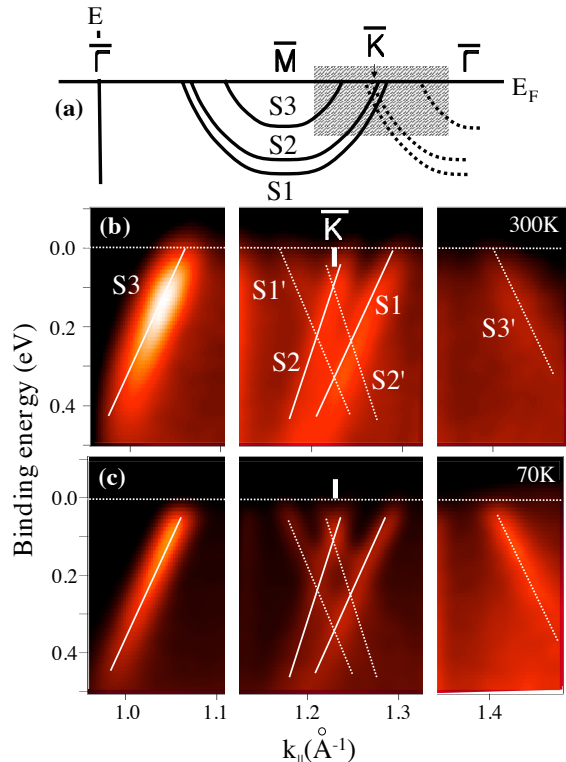


Figure 3.7: (a) Schematic illustration of the metallic 1D bands of Si(553)-Au. The shaded area indicates the section of the ARPES spectra that is shown below at (b) 300 K and (c) 70 K. The dotted line represents the Fermi energy and the bands with primed labels are the *Umklapp* bands (see text on p. 26). Reprinted figure with permission from Ref. [112]. Copyright (2005) by the American Physical Society.

Plasmon dispersions obtained by electron energy loss spectroscopy (EELS) confirm the 1D character of the metallic bands^{18,131}. While loss features are observed in the direction parallel to the Au wires, they are missing perpendicular to the wires. The loss features shift to higher energies with increasing scattering angle. Nevertheless, the plasmon dispersion curve has a slight 2D character. This is attributed to the width of the conduction channel and, to a lesser extent, to interchain coupling. Consequently, even for an isolated double-strand Au chain, there is a 2D crossover attributable to the lateral expansion of the Au wire according to Ref. [18].

Rashba Spin-Orbit Coupling

Si(553)-Au and Si(557)-Au are very similar systems in the sense that they both share the parabolic $S_{1/2}$ bands. For the latter, DFT calculations showed that the origin of the doublet resides in a spin splitting due to spin-orbit coupling¹³². Therefore, a similar situation was assumed for Si(553)-Au and a little bit later also shown theoretically by DFT calculations¹³³. The S_1 and S_2 bands are thus not two distinct bands, but rather the splitting of a single band.

Experimental evidence, however, is difficult to obtain: The small splitting of the bands requires high momentum resolution in ARPES. Additional filtering according to the emitted electrons' spin orientations significantly reduces the electron count rate. Barke *et al.* thus utilized a different approach¹³⁴: They analyzed the avoided band crossings of the S_1 , S_2 , and S_3 bands with their *Umklapp*¹³⁵ bands. The latter are back-folded bands with respect to the BZ boundary of the (5×2) unit cell and are faintly visible in ARPES^{10,112} (cf. Fig. 3.7; Fig. 2 of Ref. [134] shows a close-up with higher resolution). They originate in the doubled periodicity of the Au chain, and their visibility is directly related to the Au atoms' degree of dimerization.

In total, there are four possibilities for avoided band crossings: a Rashba-type spin splitting¹³⁶, a splitting of unpolarized bands, and a ferro- or antiferromagnetic exchange splitting²⁵. While the latter three result in vertical band shifts of the two respective bands, only the Rashba-induced spin splitting leads to a horizontal shift. Indeed, a horizontal shift of the bands was observed by Barke *et al.* for Si(553)-Au. Therefore, a Rashba-type spin splitting is in good agreement with the avoided band crossings seen in ARPES and indirectly confirms the previous prediction based on DFT calculations.

A direct proof was provided shortly afterward by spin-resolved ARPES¹²⁵: A strong spin polarization was observed near the Fermi energy E_F for the band doublet, in full agreement with a Rashba spin-orbit coupling. In contrast, significant spin polarization could not be measured for the S_3 band. Non-collinear DFT calculations, including spin-orbit coupling, confirmed the measurements¹³⁷. The spins of the $S_{1/2}$ band have a large in-plane component and a smaller out-of-plane component. Surprisingly, DFT also indicates a Rashba spin-splitting for the S_3 band with a perpendicular orientation to the $S_{1/2}$ band. The magnitude of this splitting, however, was too small to be measured in the spin-resolved ARPES experiment.

Band Gap

Earlier publications on Si(553)-Au reported band gaps at LT. For instance, Ahn *et al.* found band gaps of 30 meV, 40 meV, and 23 meV for the S_1 , S_2 , and S_3 bands in ARPES at 70 K¹¹² (cf. Fig. 3.7(c)). Furthermore, an area-averaged scanning tunneling spectroscopy (STS) study confirmed a band gap at 40 K, although with a larger gap of 150 meV¹¹³. It was argued in both publications that the band gaps are due to Peierls distortions that lead to CDWs of $\times 2$ and $\times 3$ periodicity—as seen, e.g., in STM^{112,113}.

However, the band gaps are difficult to reconcile with other experimental results: For example, Aulbach *et al.*¹¹⁷ reported a finite DOS at E_F in STS, directly contradicting the previous STS study¹¹³. The states at the Fermi energy were shown to originate in the Au atoms and preclude a CDW formation as an explanation for the $\times 2$ periodic lattice distortion. More importantly, an asymmetric^b band gap of the S_1 and S_2 bands is in stark contrast to the observed Rashba splitting.

Several other studies have also shown that the surface remains metallic even at LT. This is discussed in more detail in the next subsection. Based on the current state of knowledge, band gaps at LT are therefore unlikely. However, it should be noted that a Au excess of only 0.024 ML on Si(553)-Au was reported to cause the opening of a pseudo band gap¹³⁸. The observed band gap could thus be related to a slightly differing Au coverage.

Electronic Transport and Metallicity

Okino *et al.* performed the first transport measurements of Si(553)-Au using a linear microscopic four-point probe (4PP)¹⁶. They investigated the dimensionality of the electrical conductivity by measuring the resistance R with respect to the probe spacing s : It is utilized that $R \propto s$ for 1D, $R \propto \text{const}$ for 2D, and $R \propto 1/s$ for 3D conductivity. The measured resistance R is independent of the probe spacing, indicating a 2D flow of the electrical current. Despite the quasi-1D character of the Au bands, the electrical current is thus not restricted along the Au chain. According to Okino *et al.*, this is to a small extent due to an isotropic space charge layer (SCL) beneath the surface but, more importantly, due to interchain coupling.

In addition, rotational square micro-4PP experiments allow for directional-dependent transport measurements of anisotropic systems¹³⁹. In this way, the parallel σ_{\parallel} and orthogonal σ_{\perp} conductivity were measured simultaneously. The anisotropy $\sigma_{\parallel}/\sigma_{\perp} = 2.7$ of the surface is much smaller than the band structure and the tight-binding hopping ratio suggest. Estimates based on the Boltzmann distribution and the surface-state band dispersion allow for further comparison with the experiment. The experimental σ_{\perp} is close to the estimated conductivity, while the experimental σ_{\parallel} is an order of magnitude smaller. The discrepancy is believed to be caused by intrinsic point defects and impurity atoms. These divide the atomic wires into small metallic segments and hinder the conductivity along the wires^{122,123,139}.

In another experiment of the same research group¹³⁹, extrinsic defects were introduced by O₂ gas exposition to a similar system exhibiting self-assembling atomic wires—the In/Si(111)-(4 \times 1) surface. There, σ_{\parallel} decayed rapidly, whereas σ_{\perp} remained unchanged with increasing oxygen dose. The authors concluded that the electrical current flows to adjacent chains to circumvent the surface defects. Furthermore, they suggested that a similar behavior can be expected from Si(553)-Au.^c It is further hypothesized that the S_3 band contributes to a greater extent to the conductivity because the S_3 band has a stronger interband coupling. Additionally, it was found that the surface is metallic for temperatures above 160 K and insulating below 160 K¹⁶.

Edler *et al.*, on the other hand, came to a different conclusion with their rotational square 4PP setup¹²⁴: For temperatures above 100 K, they found an anisotropy factor similar to the previous measurement. However, the anisotropy factor increases significantly upon cooling and is comparable in size with previous

^bThe problem is not only related to the differing band gaps but also to the distinctive temperature behavior of the S_1 and S_2 band gaps. For more details concerning the temperature dependence, see section 3.3.3.

^cIn section 4.1, the influence of oxygen on the transport properties of Si(553)-Au is discussed in detail.

tight-binding calculations¹⁰. This is due to the different thermal development of R_{\perp} and R_{\parallel} , which increase by two to three and one order of magnitude, respectively. The resistances stabilize at 50 K.

Two factors were identified to drive the increase of the anisotropy: First, the isotropic contribution of the SCL declines faster than the surface state contribution upon cooling. Second, interband hopping related to σ_{\perp} is significant only for higher temperatures¹²⁴. As a result, the electrical conductivity perpendicular to the chains σ_{\perp} can be entirely associated with the contribution σ_{SCL} of the SCL at LT. Subtracting σ_{SCL} from σ_{\parallel} gives the exclusive conductivity of the surface states σ_s , which peaks at about 80 K. For higher temperatures, σ_s quickly decreases, which is expected due to the enhanced electron-phonon scattering of 1D systems¹⁴⁰. However, also for temperatures as low as 50 K, the conductivity remains finite and the system metallic.

Both EELS^{18,131,141,142} and infrared spectroscopy¹⁴³ confirm the observed metallicity at LT. In EELS, the spectrum exhibits a Drude tail originating in the continuum of low-energy excitations, which is a characteristic of metals¹⁴⁴. Similarly, a robust plasmonic signal is obtained in infrared spectroscopy for temperatures as low as 20 K. In analogy to the previous discussion regarding a band gap opening, the insulating behavior in the transport measurements of Okino *et al.*^{16,139} could be related to a slightly different amount of Au on the surface¹³⁸.

Spin-Polarized Step Edge

While the $\times 3$ modulation at the step edge had been explained by a Peierls-induced CDW^{112,113}, Erwin and Himpel proposed a different scenario for the periodic lattice distortion¹³: Every third Si step-edge atom is spin-polarized with a spin moment of one Bohr magneton—in addition to the Rashba spin splitting observed for the Au states. In contrast, the other two step-edge atoms are diamagnetic, i.e., they host a pair of electrons. Compared to these atoms, the position of the spin-polarized atoms is lowered by 0.3 Å.

According to DFT calculations, the total energy is reduced by 20 meV per spin compared to a non-spin-polarized structure. An antiferromagnetic order is established along the step edge, which is favored over a ferromagnetic order by 2.4 meV per spin. A nearest-neighbor Heisenberg Hamiltonian calibrated by DFT total energies yields an antiferromagnetic coupling of $J_{\parallel} = 15$ meV along the steps and a weaker ferromagnetic coupling of $J_{\perp} = -0.3$ meV across the steps¹³.

The spin-chain (SC) model well reproduces many experimental observations: The modulation of the step-edge geometry explains the $\times 3$ reflexes observed in LEED. Similarly, the periodic $\times 3$ pattern seen in STM images is attributed to the structural and electronic modifications at the step edge (cf. Fig. 3.4).

The non-polarized surface exhibits a metallic band that is not observed in ARPES. This band has its origins in the identical step-edge atoms. In the SC model, it is replaced by two less dispersive bands associated with the diamagnetic and spin-polarized step-edge atoms, respectively. While the former band entirely shifts below the Fermi energy, the latter spin-splits into two states below and above the Fermi energy with an exchange splitting of 0.5 eV. Although the occupied spin-split band is also not observed in ARPES, its absence is justified by thermal fluctuations. These are hypothesized to commence between 30 K to 70 K^{109,145} due to the relatively low energy gain per spin-polarized atom.

Nevertheless, direct experimental proof of spin-polarized surface states, e.g., by spin-resolved STM or STS, is still missing. There is, however, some indirect evidence: A nondispersing state 0.62 eV above E_F and two states 0.45 eV and 0.79 eV below E_F were observed in a two-photon photoemission (2PPE)

experiment¹⁴⁶. These match only with the calculated step-edge bands of the SC model. Furthermore, the occupied band was located by STS at 40 K above every third step-edge atom—although at a slightly lower energy of 0.5 eV¹⁴⁵. This state was missing above the other surface atoms.

It was shown in STM that the $\times 3$ periodicity at the step edge vanishes for low tunneling voltages, in contradiction to a CDW scenario¹¹⁷. Simulated constant-current STM images based on the SC model reproduced this behavior at the step edge: a $\times 1$ periodicity at low and a $\times 3$ periodicity at higher biases¹¹⁷.

In SPA-LEED, the $\times 3$ reflexes appear as elongated spots, indicating a long-range order of the spin-polarized step-edge atoms across the terraces¹²⁰. The associated unit cell is described by a centered geometry. A reduction of the Madelung energy¹⁴⁷ by the Coulomb interaction is assumed to cause the spins' long-range order. Indeed, classical electrostatic and DFT calculations support this scenario: A centered geometry lowers the energy by 2 meV per spin. In this geometry, the spins are arranged in a triangular lattice, locking them in a frustrated spin state due to the antiferromagnetic coupling along the step edge. It is thus postulated that the spins form a 2D quantum spin liquid¹²⁰. In contrast, adjacent Au chains are uncorrelated, as is apparent by the $\times 2$ streaks.

As the periodicities of the spin chain and Au chain are coprime, an interaction between both would be evident by additional $\times 6$ periodic features. In SPA-LEED¹²⁰ and STM^{10,110,112,113} experiments, patterns with sixfold periodicity are missing. However, Aulbach *et al.* demonstrated that faint $\times 6$ modulations are visible in STM between +0.1 V to +0.4 V¹²¹. In this range, the step edge exhibits $\times 6$ periodic patterns with alternating brighter and darker spin-polarized and non-polarized step-edge atoms. The interaction is unidirectional, i.e., the Au chain modulates the step edge, but not vice versa. Missing $\times 6$ features in SPA-LEED¹²⁰ suggest that the interaction is of electronic nature. In general, dimer formation is accompanied by charge accumulation between the participating atoms. This is also seen in STM¹¹³ for the Au dimers. The step-edge modulations are thus explained by the Coulomb interaction of the step edge with these Au dimers¹²¹. While the diamagnetic step-edge atoms react to the dimers on the same terrace, the spin-polarized step-edge atoms are sensitive to the dimers on the adjacent downhill terrace (cf. Fig. 5.3). Local STS spectra taken above two neighboring spin sites confirm that the DOS is indeed shifted by about 20 meV¹²¹.

3.3.3 Phase Transition

In this subsection, some new and some already mentioned properties of Si(553)-Au are revisited in light of their temperature dependence.

Peierls-Induced Charge-Density-Waves

In an early study, Ahn *et al.*¹¹² observed a phase transition in both STM and LEED occurring somewhere between 70 K and 300 K: Upon heating, the $\times 3$ step-edge periodicity is replaced by the $\times 1$ periodicity of the underlying lattice. The same applies in part to the $\times 2$ periodicity of the Au chain: While the $\times 2$ pattern in STM has mostly disappeared at 300 K, the $\times 2$ reflexes in LEED are still visible (cf. Fig. 3.4). Therefore, the authors assumed that two independent phase transitions occur concerning the $\times 3$ and $\times 2$ periodic lattice distortions. They specified a transition temperature of 250 K for the period tripling based on ARPES and LEED measurements. In addition to the structural changes, band gap openings of 30 meV and 23 meV at 70 K for the S_1 and S_3 bands were reported, as shown in Fig. 3.7(c). In contrast, the S_2 band has a reported temperature-independent band gap of 40 meV¹¹².

Similarly, a continuous band gap opening was observed in area-averaged STS¹¹³. However, a considerably lower transition temperature of 110 K is reported. In addition, a band gap of 150 meV at 40 K is specified, which is in stark contrast to the band gap estimates in ARPES. Both publications identify the band gaps as Peierls-induced CDWs, causing the $\times 2$ and $\times 3$ lattice distortions^{112,113}.

Transport measurements performed by microscopic 4PP supports the observation of a band gap opening¹⁶: Upon cooling, the conductivity remains metallic and steadily increases up to 160 K. Further cooling leads to a drastic drop in conductivity, which was hypothesized to be a metal-insulator transition (MIT) occurring at 160 K.

These three observed phase transitions seem to have contradicting transition temperatures: two band gap openings at 250 K in ARPES, an MIT at 160 K in a 4PP experiment, and a band gap opening at 110 K in STS. Ref. [16] gives an explanation on how to reconcile the different transition temperatures: STM measurements¹¹³ show that defect sites on Si(553)-Au act as nucleation sites for the $\times 3$ periodic elements at the step edge, rendering regions around the defects insulating. With decreasing temperature, these regions spread along the atomic chains. In area-averaged STS, a band gap opens when the whole surface becomes insulating. Electronic transport on Si(553)-Au, on the other hand, relies on interchain coupling due to defects: Growing insulating regions interrupt the metallic conduction channels, which leads to a breakdown of the surface conductivity. This happens even though the surface is not insulating as a whole. As a result, the MIT in transport measurements is observed at higher temperatures compared to STS. In ARPES, however, the band gap opening was defined by an energy shift of a leading edge in the spectrum. Consequently, the opening is observed as soon as the first defect-induced isolating regions develop.

Another explanation is given by differing defect concentrations. It is reported that defect concentrations are difficult to control, even when sample preparation follows a fixed procedure¹⁴⁸.

Order-Disorder Phase Transition

The three previously discussed publications^{16,112,113} explain the phase transition by a Peierls-induced CDW leading to an MIT. However, this is difficult to reconcile with several other observations: (i) the fractional band fillings do not match the nesting condition for a Peierls transition^{36,117}; (ii) an asymmetric band gap opening is inconsistent with a Rashba-split $S_{1/2}$ band¹³⁴; (iii) the periodicity at the step edge in STM depends critically on the tunneling voltage^{117,121}; (iv) a finite DOS at the Fermi energy E_F was observed in the most recent STS spectra¹¹⁷; (v) plasmon dispersions obtained by EELS^{18,141} and infrared spectroscopy¹⁴³ indicate a metallic surface over a broad temperature range; (vi) the surface remains metallic at LT according to the latest 4PP measurements¹²⁴, and (vii) all relevant atomic models lack a band gap in DFT at E_F ^{13,126}.

In contrast, the spin chain model¹³ explains the phase transition by an *order-disorder* transition. Filling the DB of every third step-edge atom with a single, unpaired electron lowers the total energy by about 20 meV per spin. However, the relatively low energy gain makes the surface susceptible to local thermal fluctuations between spin-polarized and diamagnetic states. These fluctuations wash out the long-range order at the step edge. As a consequence, only an averaged $\times 1$ periodic structure is observed.

Spatially resolved STS measurements¹⁴⁵ at different temperatures support an order-disorder transition scenario: A nondispersing band at +0.5 eV, identified with the spin-split band in the SC model, is detected above every third step-edge atom at 40 K. Above the other step-edge atoms, this state is missing. At 300 K, however, this characteristic peak is visible above every step-edge atom but with a smaller amplitude.

Furthermore, *ab initio* molecular dynamics (AIMD) and kinetic Monte Carlo simulations show the melting of the $\times 3$ ground state at about 30 K due to thermal fluctuations¹⁰⁹. More importantly, it was shown that defects locally pin the spins and stabilize the ground state, which leads to higher transition temperatures, as is seen in experiments¹¹³.

Pinning of the $\times 3$ superstructure by defects is also observed in SPA-LEED¹²⁴. Upon heating, the full width at half maximum (FWHM) of the $\times 3$ reflex in the direction along the steps suddenly increases at 100 K. At the same time, the peak intensity decreases superexponentially. The $\times 3$ reflex finally vanishes at 160 K. This temperature depends sensitively on the defect concentration, while the onset of the phase transition is mostly unaffected by surface defects. In comparison, the $\times 2$ reflex intensity mainly displays an exponential decrease related to the Debye-Waller effect¹⁴⁹. The FWHM remains mainly unaffected with a single exception: At 65 K, it exhibits a faint discontinuity, which is assumed to be related to a change of the dimerization strength along the Au wires¹²⁴.

At the same temperature, a sudden increase in the surface conductivity is found: Upon heating, the low but finite surface conductivity rapidly increases until it peaks at about 80 K. For higher temperatures, the conductivity decreases again—in agreement with metallic transport and the postulated enhanced electron-phonon scattering for 1D systems¹⁴⁰. Instead of an MIT, these measurements suggest a metal-to-metal transition with a critical temperature of 100 K. The metal-to-metal transition is proposed to originate in thermal excitations between delocalized Au and more localized Si states. This transition is elaborated in more detail in chapter 6.

SPA-LEED measurements performed by Hafke *et al.*^{150,151} agree qualitatively with the other SPA-LEED data¹²⁴. However, they note that the long-range order of the $\times 3$ reflex collapses faster across than along the steps. This unusual behavior implies a thermally induced crossover from 2D to 1D and is attributed to the creation of soliton-antisoliton pairs at the step edge. These destroy first the interwire and afterward the intrawire correlation. A Hamiltonian based on the Potts model¹⁵², which is a generalization of the Ising model, is used to study the dynamics of interacting wires. It well reproduces the measured data¹⁵⁰.

Phase Transition Driven by Electron Doping

Another metastable phase of Si(553)-Au is accessible via electron doping by an STM tip^{118,119}. In this phase, the step edge periodicity changes from threefold to twofold. After a while, the excited state is destabilized by excess carrier flow to the bulk and transitions back to the $\times 3$ ground state. The lifetime of this excited state is characterized by a specific time constant and is unaffected by the tunneling current. The transition rate to the $\times 2$ state, on the contrary, accelerates with increasing tunneling current and decreases with rising temperature. Indeed, a $\times 2$ superstructure at the step edge is ubiquitous for all accessible tunneling currents at temperatures as low as 13 K. For intermediate currents and high temperatures, a $\times 6$ periodic step-edge structure is observed, which can be explained by a time-averaged linear combination of the low- and high-current phase and is unrelated to an interaction with the Au chain.

3.4 Au on Si(557)

Among all vicinal Si(111)-Au surface, Si(557)-Au was discovered first¹¹. It has been extensively investigated and spurred the examination of other Si(hhk)-Au surfaces¹⁰. Many of its properties can be transferred to the other vicinal surfaces. For instance, it shares many characteristics with Si(553)-Au, of which some are outlined in the following. However, there are also considerable differences, which are mostly related to the different surface orientations and differing structural motifs. One example is the influence of oxygen on the electronic transport properties of both surfaces, which is explored in more detail in section 4.1.

3.4.1 Atomic Structure

As listed in Tab. 3.1 on p. 21, the terrace width of Si(557)-Au is 19.2 Å. Compared to Si(111)-Au, this allows for a slightly larger separation between the Au wires. Approximately 0.18 ML of Au is deposited on the Si(557) surface at 650 °C with subsequent flash-annealing at 850 °C. As a result, well-ordered Si(557) terraces decorated with parallel-aligned Au wires form¹⁰.

STM^{12,153–155} was used to investigate the surface structure. Two different atomic wires with different characteristics are identified at the edges of each terrace¹⁵⁵: One atomic wire is seen best in empty-state STM images and exhibits a twofold periodicity¹⁵³ in the direction along the step edge. The other atomic wire shows pronounced features in filled-state images and is less corrugated. In addition, irregular bright protrusions decorate the surface¹⁵⁵.

Because Au atoms scatter X-rays more strongly than Si atoms, XRD is used to distinguish between both types of atoms¹⁵⁶. The XRD pattern reveals a very simple structure with a single Au atom per (6 × 1) unit cell. This is consistent with a Au coverage of 0.18 ML determined in other experiments^{10,11}. Additionally, the Au atoms substitute Si atoms in the top layer of the surface and are situated in the middle of the terrace. These two points suggest that both atomic wires seen in STM consist of Si and not Au atoms. Furthermore, the Si-Au bond lengths are indistinguishable from the Si-Si bond lengths. Consequently, the Au atoms are incorporated into the Si surface with little strain.

In addition, XRD indicates that a Si adatom is present in every second unit cell. Each Si adatom saturates three Si surface atoms with DBs. The adatoms form a row that is identified with the corrugated atomic wire with $\times 2$ periodicity seen in STM.

The other atomic wire is associated with the Si step edge. An analysis of the Debye-Waller factor¹⁴⁹ near the step edge hints towards a trigonal (120°) bonding geometry of sp^2 character. This is consistent with an HCC reconstruction at the step edge, similar to Si(553)-Au.

DFT calculations¹⁵⁷ by Sanchez-Portal *et al.* confirmed the structural motifs derived from XRD. Although the exact position of the adatoms was not ultimately determined, there is already a good agreement between the calculated band structure and the ARPES data. A little later, Crain *et al.*¹⁰ published a structural model with an additional adatom row. This structural model well reflects the $\times 2$ periodicity observed in STM.

The faint corrugation at the step edge was mainly explained by the interaction with the $\times 2$ periodic adatom row¹⁰. However, Erwin *et al.*¹³ gave another explanation: In analogy to Si(553)-Au, every second step-edge atom is spin-polarized. This is accompanied by a slightly reduced height of \approx 0.5 Å of these step-edge atoms. The structure of the spin-polarized model is illustrated in Fig. 3.8.

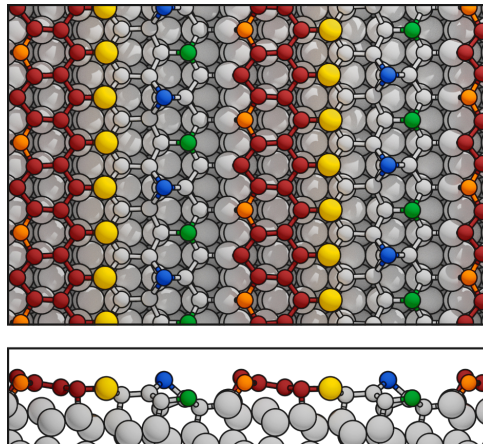


Figure 3.8: Side and top view of the spin chain structure of Si(557)-Au. Large and small grey circles indicate saturated Si bulk and surface atoms. Honeycomb chain atoms are colored red, while green, blue, and orange circles represent unsaturated Si rest atoms, Si adatoms, and spin-polarized Si step-edge atoms, respectively. The Au chain is shown by yellow circles.

3.4.2 Electronic Structure

In ARPES measurements performed between 12 K to 300 K, no significant change in the electronic structure was observed¹¹. In the direction along the step edge, a half-filled dispersing band was measured that was attributed to the 6s states of the Au atoms. The lack of dispersion perpendicular to the Au wires was seen as a validation for the system's one-dimensionality. Close to the Fermi vector k_F , the dispersing band has a peak at about -100 meV. Near the Fermi energy, the intensity of the band drops, and no explicit Fermi cutoff is visible. However, its metallic character can be deduced from its dispersion and occupation¹¹. Consequently, no CDW formation and, thus, no Peierls instability was observed. Luttinger liquid theory¹⁵⁸ requires the absence of Peierls instabilities at finite temperatures as well as a momentum-resolved spectral function that follows a power-law behavior of the form $(E - E_F)^{\alpha-1}$. While a reliable α could not be extracted from the data, a band splitting of the dispersing band was observed that seemed to merge at E_F and was identified with holon and spinon excitations. Therefore, the authors concluded that “*our system is a realization of a Luttinger liquid, one of whose properties is vanishing spectral intensity at E_F .*”¹¹

It was later shown in ARPES measurements with improved energy and momentum resolution^{12,153} that the band splitting with the alleged single crossing at E_F is, in fact, two separate crossings in close distance. This finding is inconsistent with the interpretation of a Luttinger liquid and spin-charge separation. Despite the absence of Luttinger liquid behavior, the system displays a high degree of correlation. For instance, the plasmons measured in EELS indicate a strong 1D confinement^{18,159}. Although the plasmon dispersion is similar to that of a free-electron gas, a strong influence of electron correlation on the signal is visible. Section 4.2 elaborates on the plasmonic properties of Si(557)-Au in more detail.

The Fermi surface of Si(557)-Au is slightly corrugated, indicating a quasi-1D rather than a genuine 1D system¹⁰. The 2D coupling was estimated by tight-binding calculations fitted to the ARPES data¹⁰. The ratio of the parallel and perpendicular coupling constants $t_{||}/t_{\perp}$ yields a value of ≥ 60 . Although not truly 1D, the high ratio is indicative of the mostly 1D character of the atomic wires.

The finding of two instead of one closely spaced half-filled bands (labeled S_1 and S_2) also resolves the apparent contradiction with an even number of electrons per unit cell. However, the filling of these two bands is not exactly 0.5 e. Instead, fillings between 0.42 – 0.5 e for S_2 and between 0.49 – 0.54 e for S_1 have

been reported^{10,12,110,153}, resulting in a unit cell with a fractional number of electrons. Different explanations have been given for this: One explanation is that the actual unit cell is larger than the experimentally observed³⁶. Another explanation is given in terms of electron doping by additional Si adatoms¹⁰. In combination with the high defect density of about 10%^{10,12}, this could also account for the differences in the reported band fillings. However, it should be noted that the band fillings obtained by DFT calculations exhibit similar fractional fillings¹⁵⁷, suggesting that these are intrinsic.

Similar to Si(553)-Au, the S_1 and S_2 bands are Rashba-split. They originate in the same band associated with the single-strand Au chain. In fact, the Rashba splitting was first predicted by DFT calculations for the Si(557)-Au surface¹³². Later, a thorough analysis of the avoided crossings of the parabolic bands in ARPES¹³⁴ confirmed that the splitting is of the Rashba type.

The Si adatom row and the step edge were investigated at room temperature using STS¹⁵⁴. While the adatom row seems to be insulating, a finite local DOS is observed at the step-edge atoms, rendering the latter metallic.

In analogy to Si(553)-Au, DFT calculations indicate that the step edge of Si(557)-Au is also spin-polarized¹³. Here, however, every second step-edge atom hosts an unpaired electron—in contrast to every third in the case of Si(553)-Au. Furthermore, the Si rest atoms are fully polarized as well. In the direction along the step edge, both types of atoms exhibit an antiferromagnetic interaction. The same holds for the spins of adjacent rows. An energy gain of 45 meV per spin is reported in relation to the unpolarized surface¹³.

3.4.3 Phase Transition

In contrast to earlier reports^{11,110}, Ahn *et al.* observed a phase transition at about 270 K¹⁵³. The phase transition becomes apparent by a symmetry breaking involving a period doubling of the step edge at LT. The period doubling is attributed to an up-down buckling of the step-edge atoms accompanied by an MIT. In the case of the S_1 band, a gap opening and a shift of the leading edge by 40 meV is observed in ARPES¹⁵³. Supplementary STS measurements show that the band gap is symmetrical and 80 meV in size¹⁵⁴. Similarly, also the S_2 band exhibits a band gap. However, the band gap is reported to be stable even at room temperature¹⁵³. EELS measurements support this claim¹⁵⁹. However, one should note that this is in contrast to the proposed Rashba-split $S_{1/2}$ band—similar to Si(553)-Au.

The phase transition was explained by fluctuating step-edge atoms^{132,160}. The mechanism is similar to the phase transition described in chapter 6 for Si(553)-Au. While the step-edge-fluctuation model can explain the buckling at the step edge, the ARPES and STS measurements are not reproduced as well. However, with the advent of the spin-chain (SC) model, the phase transition is explained more consistently: For instance, the opening of a small band gap is also found in the SC model.

On the other hand, transport measurements show that the temperature dependence of Si(557)-Au is entirely different from that of Si(553)-Au¹⁶. Si(557)-Au exhibits an activation-type T dependence that is incompatible with an MIT: With increasing temperature, the conductivity increases steadily.

*Science is what we understand well enough to explain to a computer.
Art is everything else we do.*

Donald Knuth

4

Electronic Properties of Clean and Oxidized $\text{Si}(hhk)$ -Au Surfaces

True one-dimensional (1D) systems differ from their higher-dimensional counterparts by having a particularly pronounced electron correlation. This correlation leads to unique properties not seen elsewhere. They are characterized by the Luttinger liquid theory^{7,8} (see section 2.1). Although the collapse of Fermi liquid behavior in the $\text{Si}(hhk)$ -Au family could not be observed, several members of this family exhibit complex electrical and kinetic behavior. Despite this, the question remains to what extent a dimensional crossover between Fermi and Luttinger liquid exists.

The presence of defects further complicates this question. In 1D materials, defects have a severe impact on the system. Already a single point defect breaks the periodicity of a 1D crystal in its only available direction. In the case of self-assembled atomic Au wires on $\text{Si}(hhk)$ surfaces, it is presumed that point defects reduce the conductivity along the wires^{16,139,161}. At the same time, they significantly increase the hopping probabilities perpendicular to the wires and, as a result, reduce the anisotropy of the system. On the other hand, point defects can also stabilize the local structure by shifting the critical temperature T_c of a phase transition. In the case of $\text{Si}(553)$ -Au, the $\times 3$ periodicity at the step edge is visible at higher temperatures in the vicinity of defects^{113,122,162}. Likewise, point defects in the form of oxygen adsorbates increase the inter- and intrawire coupling of the $\text{In}/\text{Si}(111)$ surface. In this way, oxygen stabilizes the insulating (8×2) LT phase and shifts T_c to higher temperatures. However, other adsorbates have the opposite effect and reduce T_c ¹⁶³⁻¹⁶⁶.

Kang *et al.* investigated the atomic and electronic properties of various point defects that occur on $\text{Si}(553)$ -Au and $\text{Si}(557)$ -Au using STM and STS¹¹⁵. They found five different types of point defects connected to dissociated water adsorption, displaced Si adatoms, and missing Au atoms. In STS, water-adsorbed defects near the honeycomb chain (HCC) induce a band gap of around 0.5 eV. However, the most reactive part of the $\text{Si}(557)$ -Au surface is the Si adatom—even more reactive than the HCC. At this site, water adsorption is not accompanied by a band gap opening. These results led to the conclusion that the HCC is relevant for electronic transport. A previous study had come to the same conclusion¹⁶¹.

Besides water and hydrogen, oxygen is a primary contributor to contamination by residual gas in vacuum chambers. It is also one of the basic components of our atmosphere. Consequently, oxidation is the first modification that will occur when samples come into contact with the environment¹⁶⁷. Silicon wafers, e.g., are known to form a μm -thick SiO_2 layer. Therefore, it is of interest to know how Au-decorated Si surfaces—and especially the self-assembled atomic wires—behave upon oxygen adsorption.

In section 4.1, the electrical conductivity of the clean Si(553)-Au and Si(557)-Au surfaces is investigated in comparison to the same oxidized surfaces. Subsequently, section 4.2 shows that plasmon spectroscopy is a valuable tool to make robust predictions about the electronic excitation spectrum when aided by *ab initio* calculations. This new method is tested on clean and oxygen-adsorbed Si(*hhk*)-Au surfaces.

4.1 Influence of Oxygen Adsorption on the Conductivity of Si(553)-Au and Si(557)-Au

Here, in cooperation with F. Edler (Leibniz Universität Hannover), the influence of oxygen adsorbates on the Si(553)-Au and Si(557)-Au surfaces is investigated using electrical transport measurements, LEED and DFT¹⁶⁸. In general, direct current (DC) conductance measurements are very sensitive to the electronic states near the Fermi energy. As the applied electrical fields are weak, the probed energy range is typically within a few $k_{\text{B}}T$. Furthermore, DC conductance is strongly dependent on the charge carrier mobility, which is easily impaired by defects¹⁶⁷. It is, therefore, very susceptible to the disorder of a system.

The results were published in Ref. [168], and the following subsections closely follow the structure of this paper.

4.1.1 Structural Changes Induced by Oxygen Adsorption

Si(553)-Au and Si(557)-Au are very similar, while the few differences originate mostly in their opposing surface orientation. For instance, Si(553)-Au has a double-strand Au chain while Si(557)-Au has a single-strand Au chain with an additional Si adatom row. At 300 K, the stepped terraces of the clean surfaces give rise to the $\times 1$ diffraction spots in the $[11\bar{2}]$ direction in LEED. Additional intensity streaks indicate a $\times 2$ periodicity in the same direction, as shown in Fig. 4.1(a) and (d). Although the $\times 2$ streaks—and the whole LEED pattern—of both surfaces look very similar, they originate from different structural elements exclusive to the respective surface. In the case of Si(553)-Au, the $\times 2$ periodicity stems from the dimerization of the double-stranded Au chain. For Si(557)-Au, the Si adatoms are responsible for the $\times 2$ pattern. Additional $\times 3$ spots associated with the step edge appear at LT for Si(553)-Au. At 300 K, however, the $\times 3$ superstructure has vanished¹¹³. Therefore only the atomic structures with simple $\times 2$ periodicity are used in the following.

Although both surfaces have a similar structure and LEED pattern, the mechanisms regarding oxygen adsorption are strikingly different. Fig. 4.1(b) and (e) illustrate the LEED pattern after a dosage of 20 L of molecular oxygen. These are shown side-by-side with the pattern of the clean surfaces in Fig. 4.1(a) and (d) for better comparison. The $\times 1$ spots resulting from the equidistant terraces and the underlying Si(111) surface remain almost unchanged. Of greater interest are the changes of the $\times 2$ features: The $\times 2$ reflexes of the Si(553)-Au surface fade only marginally, while the $\times 2$ streaks of the Si(557)-Au surface disappear

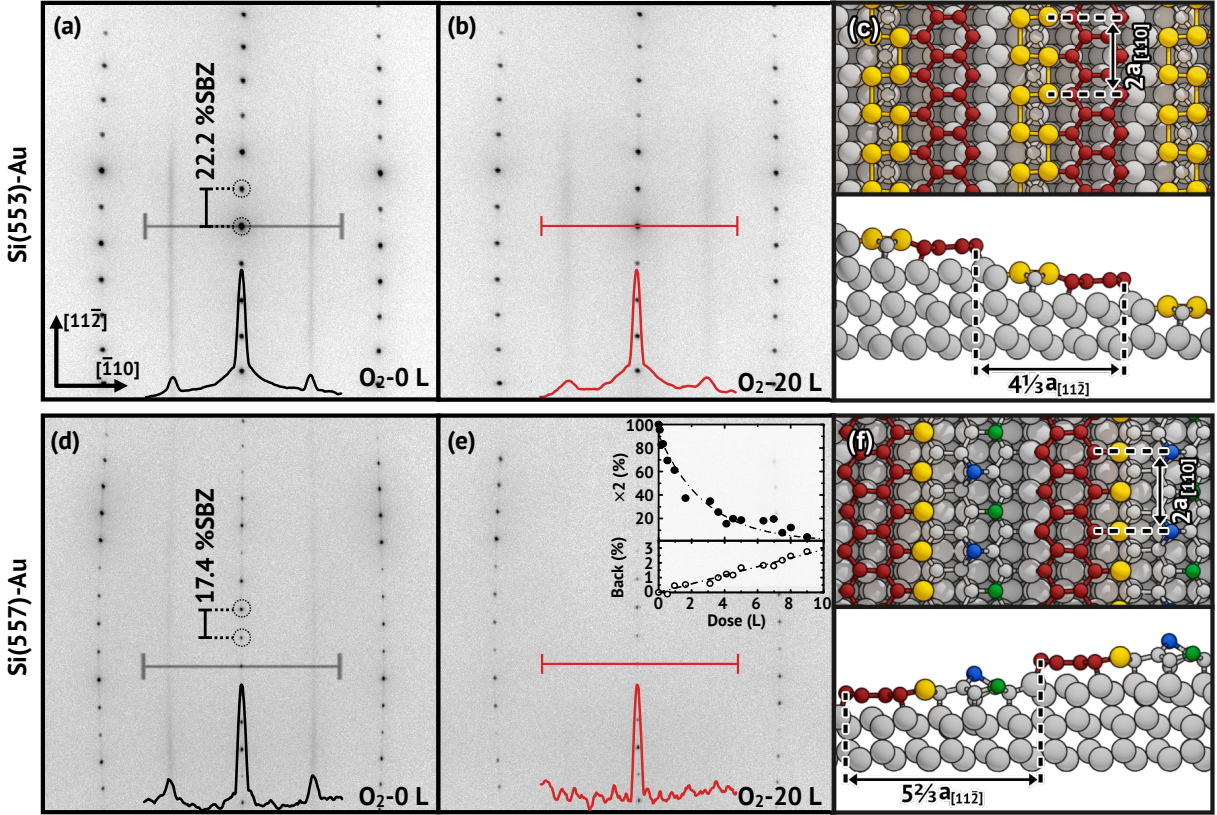


Figure 4.1: SPA-LEED patterns of Si(553)-Au and Si(557)-Au (a, d) without as well as (b, e) with an oxygen exposure of 20 L. Line scans are indicated by the horizontal bars and graphs at the bottom. In the inset of (e), the decrease of the $\times 2$ intensity and the increasing background (back) with respect to oxygen exposure is shown. In (c) and (f), the respective high-temperature structures are depicted in top and side view. Large and small grey circles indicate saturated Si bulk and surface atoms. Honeycomb chain atoms are colored red while green and blue circles represent unsaturated Si rest atoms and Si adatoms. Yellow circles indicate the Au chain. The image is adapted and taken from Ref. [168].

completely. The inset of Fig. 4.1(e) shows the nominalized peak intensity of the $\times 2$ streaks with respect to the oxygen dose. While the peak intensity decreases exponentially with increasing dose, the background noise shows a linear behavior. The latter indicates the occupation of random adsorption sites. Already at 5 L, the $\times 2$ reflex is indistinguishable from the background noise. Likewise, the background noise follows the same linear behavior at higher doses. Other adsorption sites must, therefore, also be relevant for oxygen adsorption. Assuming that every second Si adatom is occupied on average when the $\times 2$ pattern disappears, a sticking factor of 10%–20% is derived.

4.1.2 Transport Properties of the Clean and Oxygen-Adsorbed Surfaces

Four-point probe (4PP) transport measurements were performed using a square configuration, as shown in Fig. 4.2(a). With this probe arrangement, the parallel and perpendicular components of the conductance can be measured simultaneously. Current-voltage (I - V) curves were taken by changing the current between two pairs of probes from $-1 \mu\text{A}$ to $1 \mu\text{A}$. At the same time, the voltages between the other pairs of probes are measured. The slopes of the I - V curves correspond to the resistances of the respective crystallographic orientation, which are depicted for Si(553)-Au in Fig. 4.2(b). These are different in parallel and orthogonal direction and originate in the anisotropy of the surface conductivity.

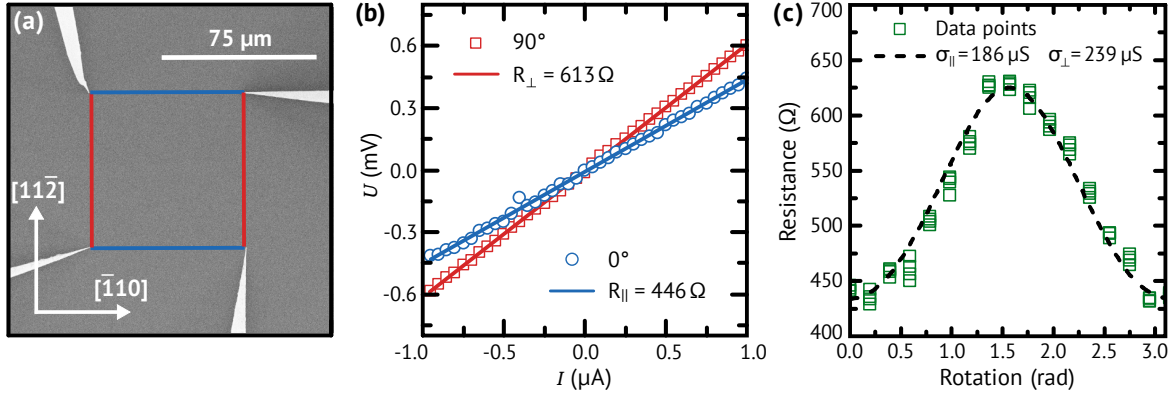


Figure 4.2: (a) 4PP setup used for transport measurements in square geometry. (b) I - V curves measured along (blue) and across (red) the wire direction. Their slopes determine the resistances R_{\parallel} and R_{\perp} . (c) The resistance with respect to the rotation angle obtained by the rotational square method. The dashed line represents the fit of the experimental data and enables the determination of the conductivity along (σ_{\parallel}) and perpendicular (σ_{\perp}) to the wires. The image is adapted and taken from Ref. [168].

With the knowledge of the resistances in both directions, the conductivity then equates to $R_{\parallel(\perp)} = (2\pi\sqrt{\sigma_{\parallel}\sigma_{\perp}})^{-1} \ln(1 + \sigma_{\parallel(\perp)}/\sigma_{\perp(\parallel)})^{169,170}$. The orientation of the atomic wires can be independently determined by rotating the probe configuration and measuring the resistance with respect to the rotation angle. Fig. 4.2(c) shows the angle-dependent resistance for Si(553)-Au.

At 300 K, the Si(553)-Au surface exhibits conductivities of $\sigma_{\parallel} = 239 \mu\text{Sv}$ and $\sigma_{\perp} = 186 \mu\text{Sv}$, resulting in an anisotropy ratio of $\sigma_{\parallel}/\sigma_{\perp} \approx 1.3$. This ratio is only half the ratio previously measured at 200 K^{16,139}. Si(557)-Au exhibits comparable conductivities of $\sigma_{\parallel} = 220 \mu\text{Sv}$ and $\sigma_{\perp} = 160 \mu\text{Sv}$, leading to a similar ratio of $\sigma_{\parallel}/\sigma_{\perp} \approx 1.4$. However, these anisotropy ratios are subject to small fluctuations: Depending on the defect concentration, they range from 1.3 to 1.7 for different samples. These values are, nevertheless, relatively small considering the quasi-1D surface bands seen in ARPES¹⁰. A much larger anisotropy would be visible if solely these bands contributed to the conductivity. The conductivity in perpendicular direction must therefore be due to parasitic bulk channels such as a space charge layer (SCL).

In a simplified model, surface defects should reduce σ_{\parallel} and increase σ_{\perp} due to increased scattering. In contrast, oxygen adsorption on Si(553)-Au and Si(557)-Au affects the conductivity perpendicular to the wires only to a minor extent. Fig. 4.3 shows the conductivity along and across the wires in relation to the oxygen dose. Upon O_2 exposure, σ_{\perp} remains almost unaffected for both surfaces. Indeed, σ_{\perp} is constant within the scattering of the data for Si(553)-Au. In the case of Si(557)-Au, the perpendicular conductivity exhibits an initial, small drop of 3% at an oxygen dose of 2.5 L. At higher doses, the conductivity recovers and adopts its initial value. This effect is most likely related to a change in band bending caused by the adsorbed oxygen, which affects the conductivity of the SCL σ_{SCL} . It is assumed that the band bending is most significant when every second reactive adsorption site is occupied on average. At higher O_2 doses, competing adsorbate-adsorbate interactions dominate, and the adsorbate-induced band bending becomes less relevant. Consequently, oxygen atoms occupy most of the reactive adsorption sites at higher doses, explaining why the $\times 2$ LEED pattern of Si(557)-Au vanishes at 5 L. A similar approach based on the SCL model was successfully applied to In/Si(111)¹⁷¹.

In contrast, σ_{\parallel} is much more affected by oxygen adsorption. While σ_{\parallel} of Si(553)-Au is only reduced by 5% at a dose of 30 L, σ_{\parallel} of Si(557)-Au is reduced by 20%. Since σ_{\perp} remains almost unaffected, the anisotropy of the conductivity disappears entirely for the latter. For Si(553)-Au, however, the anisotropy

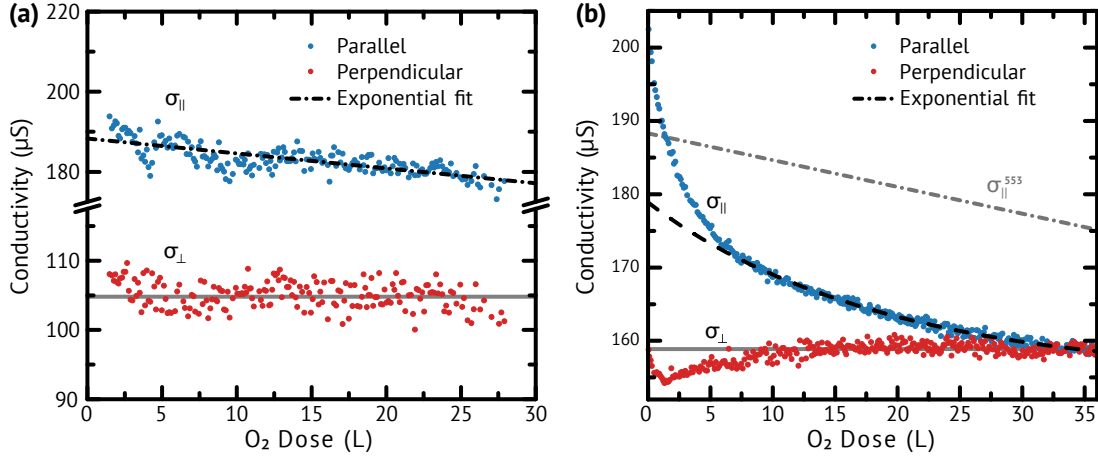


Figure 4.3: Conductivity in the parallel (σ_{\parallel} , blue) and perpendicular (σ_{\perp} , red) direction with respect to the oxygen dose for **(a)** Si(553)-Au and **(b)** Si(557)-Au. The dashed and dashed-dotted curves are exponential fits to the experimental data. The image is adapted and taken from Ref. [168].

does not change significantly. This is in so far remarkable as both surfaces share most of the structural building blocks.

In general, the conductivity can be separated into an isotropic and an anisotropic component. The former is predominantly bulk-like, whereas the anisotropic part can mainly be associated with the surface. In another study¹⁷², the same division was applied to In/Si(111), where the oxygen-related conductivity was well described by $\sigma_{\parallel}(D) = \sigma_{\text{SCL}} + \sigma_{\parallel}(0) \exp\left(-\frac{D}{D_0}\right)$. In this study, σ_{SCL} is believed to largely determine the isotropic bulk-like component, which is mostly independent of the O_2 dose D . $\sigma_{\parallel}(0)$, then denotes the conductivity along the wires of the pristine surface. This ansatz includes changes in both the band structure and the lattice periodicity. A more sophisticated approach would also consider adsorbate-adsorbate hopping transport. In this case, σ_{\perp} is relatively insensitive to oxygen adsorption, so that the hopping transport across the wires is negligible.

Applying this simple model to the changes of σ_{\parallel} leads to a good agreement with the experimental data. Fig. 4.3 compares the fitted curves (dashed lines) of this ansatz, together with the measured data. Especially for Si(553)-Au, the model is in close agreement over the entire dose range with a fitting parameter of $D_0 \approx 200$ L. For Si(557)-Au, the model can only describe the high-dose regime (≥ 10 L). At lower doses, there are considerable deviations between the fit and the data. Fig. 4.3(b) shows σ_{\parallel}^{553} alongside σ_{\parallel}^{557} , emphasizing the more substantial decrease of σ_{\parallel}^{557} for low and medium doses, but a similar decrease for high doses. The latter could be due to the occupation of common structural motifs, which only become relevant when oxygen occupied most reactive sites. However, the different behavior in the low-dose regime remains. These differences are due to the interaction of the additional Si adatoms of Si(557)-Au with the adsorbed oxygen, as shown in the next subsection.

4.1.3 Adsorption Sites of Molecular Oxygen

To gain a proper understanding of the mechanisms involved in the oxygen adsorption process, DFT calculations were carried out utilizing the Vienna *ab initio* simulation package (VASP)¹⁷³. The projector-augmented wave (PAW) method¹⁷⁴ was used to model the core electrons and the electron-ion interaction

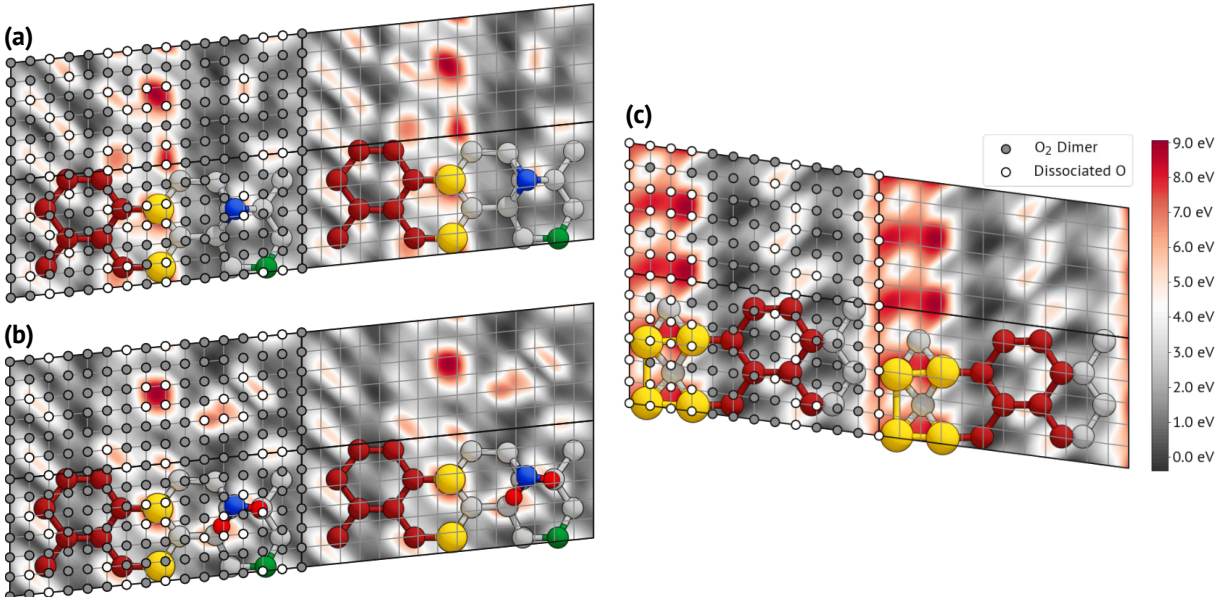


Figure 4.4: PES for the adsorption of a single O_2 molecule on pristine **(a)** Si(557)-Au and **(c)** Si(553)-Au. In **(b)**, the PES of a second oxygen molecule is displayed with initial oxygen adsorption at the Si adatom, indicated by bright red circles. Each PES is expanded to a 2×2 grid for better illustration. Gray lines indicate the mesh of the adsorption points, while gray and white circles on this grid indicate whether the O_2 molecule dissociated. The surface structure is superimposed for better orientation.

within the generalized gradient approximation (GGA) using the Perdew-Burke-Ernzerhof (PBE) functional¹⁷⁵. An energy cutoff of 410 eV was utilized for the plane wave expansion of the wavefunction. The Brillouin zones (BZs) were sampled by a Γ -centered, equidistant k -point mesh of $2 \times 9 \times 1$ and $2 \times 11 \times 1$ for Si(557)-Au and Si(553)-Au, respectively. The surfaces were modeled by periodic images of primitive surface cells of size (6×2) and (5×2) (w.r.t. Si(111)). These consisted of a hydrogen-passivated slab of six bulk-like Si bilayers. The lowest two bilayers were fixed during relaxation, modeling the bulk. An additional surface layer contained the Au surface as well as the rest of the surface reconstruction.

A potential energy surface (PES) was calculated to determine the energetically most stable adsorption sites of oxygen. For this purpose, an O_2 molecule was placed on the surfaces at each point of an equidistant mesh. The total energy was then calculated for the relaxed structure. While the surface and one of the oxygen atoms were free to relax, the lateral position of the other oxygen atom was fixed at the grid point. The adsorption energies of 90 and 72 different sites were determined for Si(557)-Au and Si(553)-Au, respectively. For each grid point, the O_2 molecule had three different starting configurations, which differed in the alignment of the molecule's axis with the three Euclidean axes. The lowest total energy of the three configurations then entered the PES.

Fig. 4.4(a) and (c) show the PES of a single O_2 molecule on pristine Si(557)-Au and Si(553)-Au. Common to both surfaces is that O adsorption near the Au chain is energetically unfavorable. This is especially true for the wider Au chain of the Si(553)-Au surface. In contrast, oxygen prefers to adsorb at the HCC and—in the case of the Si(557)-Au surface—in the vicinity of the Si adatom and rest atom. Note that the O_2 molecule dissociates at most grid sites, except for the energetically less stable. This is consistent with previous results: Mamiyev *et al.* also observed dissociative oxygen adsorption on Si(553)-Au using EELS¹⁷⁶. Furthermore, O_2 molecules dissociated upon adsorption on Si(111)-(7 \times 7) in an independent *ab initio* calculation¹⁷⁷.

(a) O ₂ on Si(557)-Au		(b) O ₂ on Si(553)-Au		(c) (O ₂) ₂ on Si(557)-Au	
Adsorption sites	Energy (eV)	Adsorption sites	Energy (eV)	Adsorption sites	Energy (eV)
Ad _{ins} -Other _{ins}	0.000	iHCC _{ins} -mHCC _{ins}	0.000	Ad _{ins} ³ -Other _{ins}	0.000
Ad _{ins} ²	0.007	eHCC _{brid} -eHCC _{ins}	0.146	Ad _{ins} ³ -Rest _{ins}	0.396
eHCC _{ins} -mHCC _{ins}	0.185	eHCC _{ins} ²	1.013	Ad _{ins} ³ -Rest _{ins} [*]	0.432
mHCC _{ins} ²	0.238			Ad _{ins} ² -eHCC _{ins} -mHCC _{ins}	0.513
eHCC _{brid} -eHCC _{ins}	0.246			Ad _{ins} ² -mHCC _{ins} ²	0.525
Ad _{ins} -Rest _{ins}	0.366			Ad _{ins} ² -eHCC _{brid} -eHCC _{ins}	0.572
eHCC _{ins} -mHCC _{ins} [*]	0.468			Ad _{ins} ³ -Ad _{top}	0.862
				Ad _{ins} ² -Other _{ins} ²	1.037

Table 4.1: The energies and adsorption sites of the stable configurations for (b) a single O₂ molecule on Si(553)-Au as well as (a) a single and (c) two O₂ molecules on Si(557)-Au. The labeling is based on the binding partner of the O atoms, i.e., ad- (Ad), rest (Rest), inner HCC (iHCC), middle HCC (mHCC), edge HCC (eHCC), or other Si surface (Other) atoms. The bonding geometry, i.e., insertion into existing bonds (ins), bridge sites (brid), and top sites (top) are indicated in the subscript. A superscript specifies the frequency (neglected for 1). For better comparison, the energies are shifted with respect to the most stable configuration.

The fourteen most stable adsorption sites on each surface served then as the starting point for a full relaxation, in which all spatial restrictions of the oxygen atoms were lifted. As the O is free to move, these fourteen starting configurations condensed in seven and three adsorption sites with (meta-)stable local minima for Si(557)-Au and Si(553)-Au, respectively. Tab. 4.1(a)–(b) lists these adsorption configurations together with their respective total energies. The oxygen molecule dissociates for all stable adsorption sites. With one exception, the individual O atoms solely occupy sites of existing bonds or bridge sites. Fig. 4.5 and Fig. 4.6 illustrate the corresponding adsorption geometries.

For Si(557)-Au, the two most stable adsorption sites are located next to the Si adatom, as shown in Fig. 4.5(a) and (b). Their adsorption energy is about 8.7 eV. They are almost energetically equivalent and significantly more stable than the sites at the HCC by \approx 180 meV to 250 meV. Oxygen occupation at adatom sites explains the disappearance of the $\times 2$ diffraction streaks seen in LEED: For Si(557)-Au, the doubled periodicity can be solely attributed to the Si adatoms. Random occupation of these two

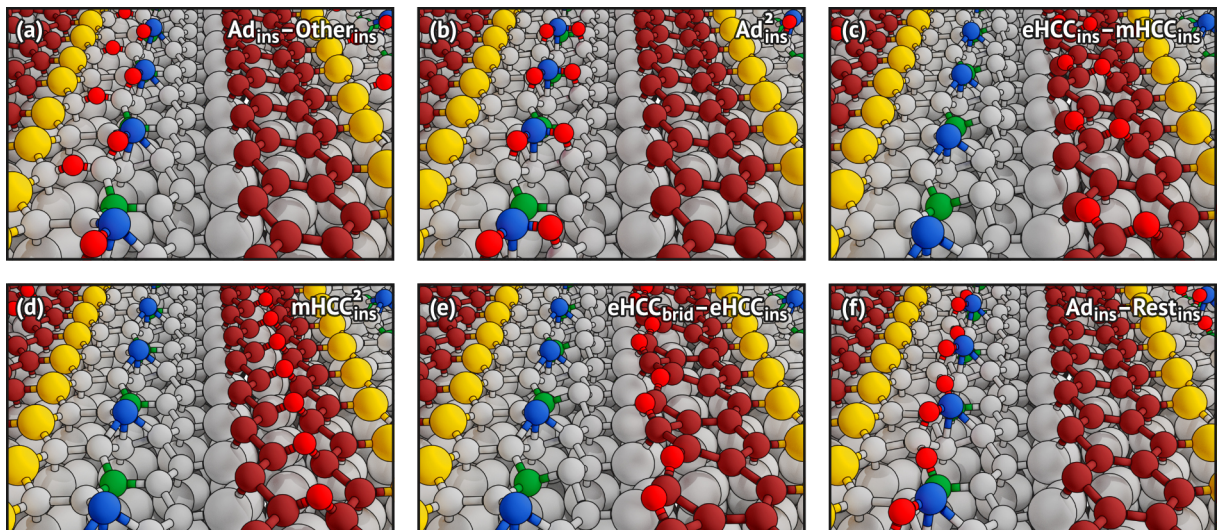


Figure 4.5: The atomic structure of the six most stable adsorption sites for a single O₂ molecule on Si(557)-Au. Bright red circles illustrate the oxygen atoms. Regarding the labels, see the caption of Tab. 4.1.

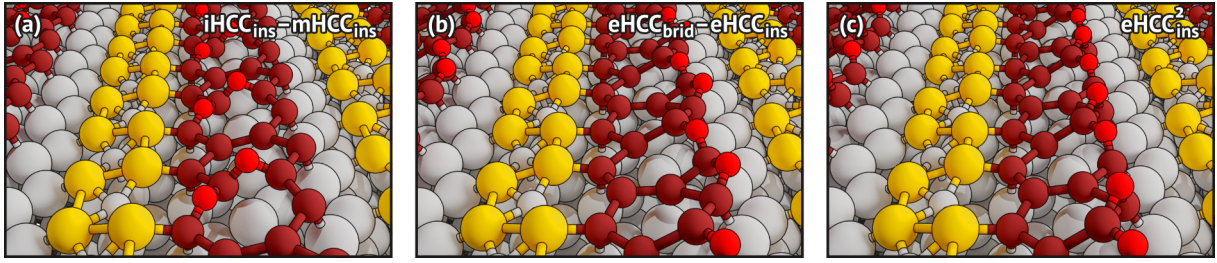


Figure 4.6: The atomic structure of the most stable adsorption sites for a single O_2 molecule on Si(553)-Au. In all three configurations, the oxygen preferably adsorbs on the HCC. Bright red circles illustrate the oxygen atoms. Regarding the labels, see the caption of Tab. 4.1.

adsorption sites exhibiting different SiO complexes thus destroys the long-range order of the $\times 2$ structure. Consequently, the $\times 2$ LEED streaks fade with increasing oxygen dose until the signal disappears in the background noise.

In contrast, Si(553)-Au lacks both Si rest and adatoms. Here, the Au and honeycomb chain cover most of the surface, and the $\times 2$ periodicity is solely due to the dimerized Au chain. The stable sites are all located at the HCC. Fig. 4.6 illustrates the atomic structure of the adsorption sites. Apart from increased background noise, the adsorbed oxygen affects the LEED $\times 2$ streaks only marginally.

In the following, the focus lies mainly on the oxidation of the more complex Si(557)-Au surface. In a similar study¹⁷⁷, multiple O_2 molecules per surface unit cell were involved in the adsorption process on the Si(111)-(7 \times 7) surface. Here, successive adsorption processes are taken into account as well.

The Ad_{ins}^2 site for the first oxygen pair proved to be a robust basis for a subsequent PES. This PES for a second O_2 molecule is shown in Fig. 4.4(c). Like the first O_2 molecule, the second molecule dissociates during the adsorption process on most parts of the surface. Tab. 4.1(c) lists the stable adsorption configurations that were obtained by a full relaxation. Fig. 4.7 illustrates several of these models. The most stable adsorption site depicted in Fig. 4.7(a) comprises three oxygen atoms directly bound to the Si adatom. The respective adsorption energy of the second O_2 molecule is in the same range as the first molecule at 8.5 eV. This configuration is favored by about 500 meV compared to a configuration where the second pair adsorbs at a different site, such as the HCC (see Fig. 4.7(d)).

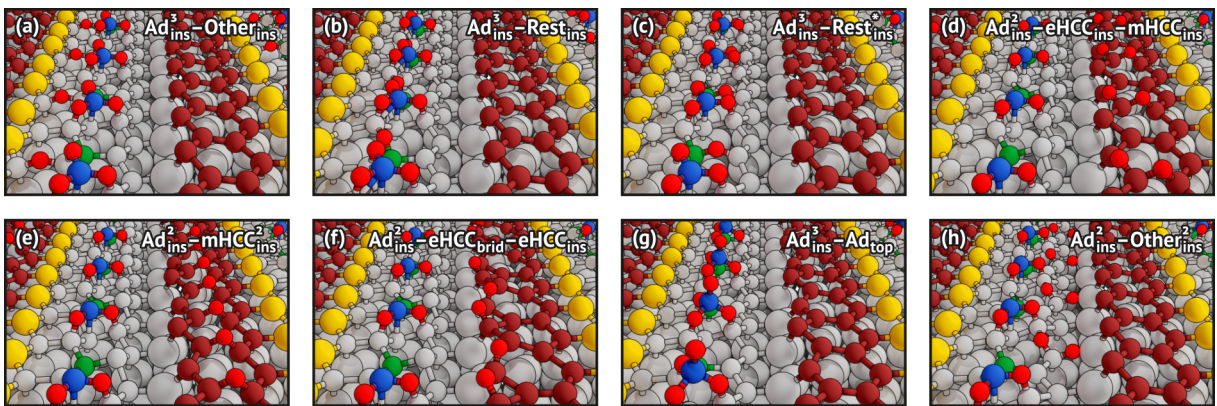


Figure 4.7: The atomic structure of the most stable adsorption sites for two O_2 molecules on Si(557)-Au. The starting point was the Ad_{ins}^2 configuration, where the first dissociated oxygen molecule was adsorbed at the adatom. Bright red circles illustrate the oxygen atoms. Regarding the labels, see the caption of Tab. 4.1.

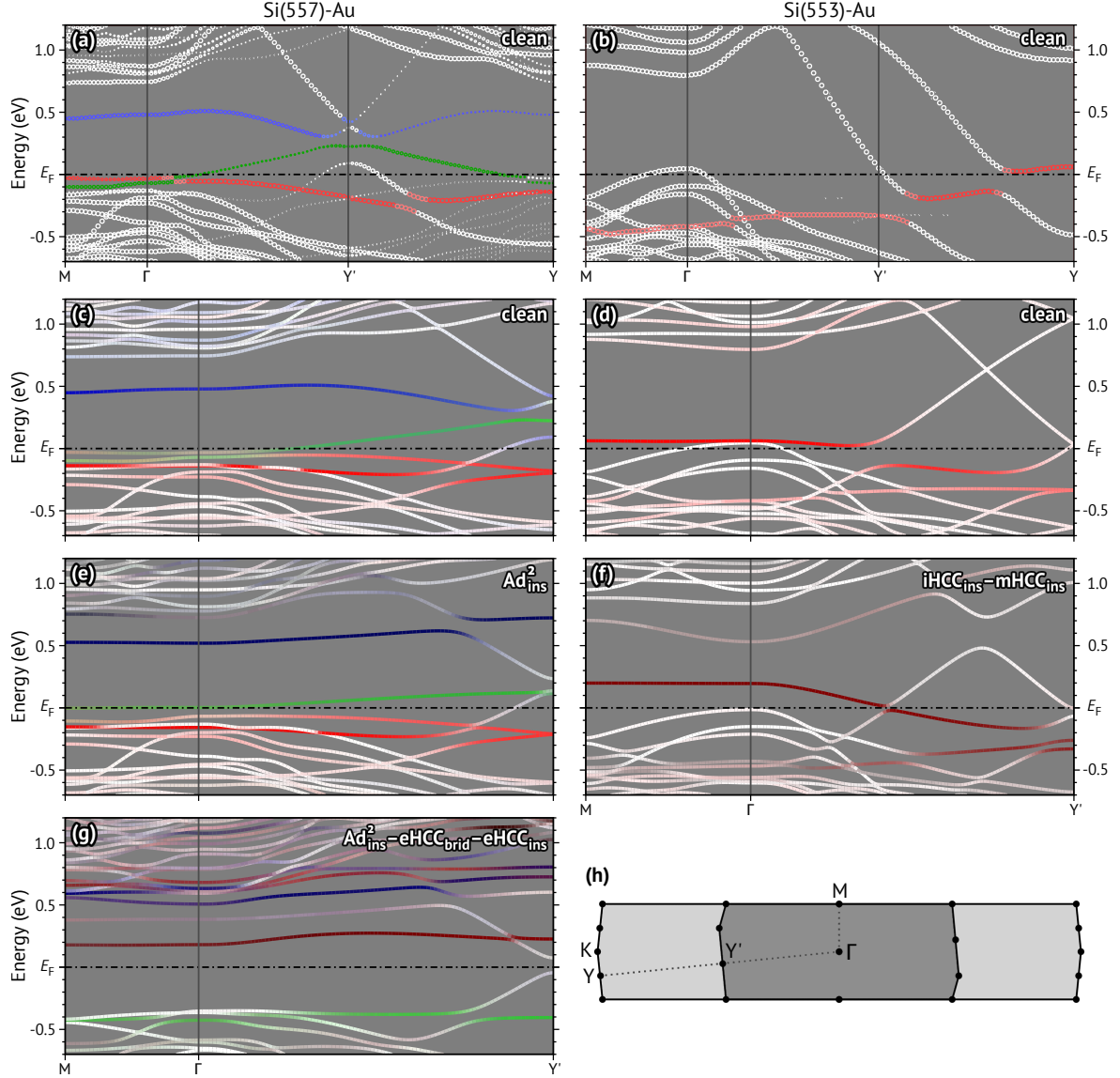


Figure 4.8: Band structures of clean and oxidized Si(557)-Au and Si(553)-Au. The unfolded band structures (according to Ref. [178]) of the clean (a) Si(557)-Au and (b) Si(553)-Au surface, obtained by the folded band structure (c, d) of the $\times 2$ surface unit cells, are shown. The point size in (a, b) indicates the $\times 1$ character of the individual state. Band structures of the oxidized surfaces are depicted for the (e) Ad_{ins}^2 and the (g) $\text{Ad}_{\text{ins}}^2\text{-eHCC}_{\text{brid}}\text{-eHCC}_{\text{ins}}$ model for Si(557)-Au and the (f) $\text{iHCC}_{\text{ins}}\text{-mHCC}_{\text{ins}}$ model for Si(553)-Au. The BZs of the $\times 1$ (light gray) and $\times 2$ (dark gray) supercell are shown in (h). The color code of the surface bands corresponds to their projection onto the atomic orbitals of the adatom (blue), HCC step-edge atoms (red), and rest atom (green). A black color admixture indicates hybridized states with oxygen contribution. The image is adapted and taken from Ref. [168].

4.1.4 Band-Structure Changes Induced by Oxygen Adsorption

Band structures of the (meta-)stable models listed in Tab. 4.1 provide a better understanding of the distinct electronic transport behavior of Si(557)-Au and Si(553)-Au upon oxygen adsorption. Fig. 4.8(a)–(b) illustrates the unfolded band structures of the clean surfaces. For Si(557)-Au, two bands associated with the Au chain (white and parabolic) and the Si rest atoms (green) are crossing the Fermi energy E_F . The latter is unoccupied in most parts, which corresponds to a rest atom with an almost empty dangling bond. Additional red-colored and blue-colored bands stem from the HCC step-edge atoms and the Si adatoms. While the former is fully occupied, the latter gives rise to a dispersive unoccupied surface band.

Similarly, the parabolic band crossing E_F for Si(553)-Au is due to the Au chain, while the other band with a Fermi crossing near the Γ -point is due to the SCL (both white). An additional anticrossing of a second dispersive Au band with the reddish step-edge band (approx. one third between Γ and Y') divides both bands into an occupied and unoccupied part.

Band structures of selected oxygen adsorption sites are depicted in Fig. 4.8(e)–(g). In these images, a darker coloration of the bands illustrates a high admixture of oxygen. The band structure of the Ad_{ins}^2 oxidation site (cf. Fig. 4.5(b)) on Si(557)-Au is shown in Fig. 4.8(e). Compared to the band structure of the pristine surface, the Si adatom band (blue) exhibits a strong hybridization with oxygen orbitals, indicated by a darkening of the band. Furthermore, the high electronegativity of oxygen depletes the residual charge of the nearby rest atom's dangling bond. Consequently, the metallic band associated with the rest atoms is energetically slightly raised. Additionally, the effective mass increases by 13% at the intersection point with the Fermi energy. In a simplified model, the conductivity should decrease in a similar range. The red surface band associated with the step edge, however, remains mostly unaffected.

As previously discussed, the redistributed charge induced by the oxygen results in additional surface dipoles. The work function tightly depends on these dipoles and also impacts σ_{\perp} to some degree. Nonetheless, DFT predicts a reduction of the charge carriers combined with an increased effective mass, leading to a reduced conductivity. However, it should be noted that the periodic boundary conditions combined with a relatively small unit cell imply an adsorption scenario in the high-coverage regime. At lower coverages, the scattering at oxygen defects becomes more significant, which further reduces the conductivity.

The band structure in Fig. 4.8(e) is very prototypical for a single adsorption process near the adatom. For surfaces with a second pair of O_2 adsorbed to them, the band structure dramatically changes based on the adsorption site. For instance, the band structure of the most stable adsorption configuration ($\text{Ad}_{\text{ins}}^3\text{-Other}_{\text{ins}}$, not shown) looks very similar to the band structure of the previously discussed Ad_{ins}^2 . In contrast, the band structure of the $\text{Ad}_{\text{ins}}^2\text{-eHCC}_{\text{brid}}\text{-eHCC}_{\text{ins}}$ adsorption configuration (cf. Fig. 4.7(f)) exhibits the most significant changes. As shown in Fig. 4.8(g), the surface bands of this configuration feature a band gap of about 100 meV at the Fermi energy. Consequently, surface transport should cease entirely. The conductivity is then mainly determined by the bulk, and the anisotropy should disappear.

Compared to $\text{Ad}_{\text{ins}}^3\text{-Other}_{\text{ins}}$, this configuration is less stable under idealized conditions. However, the energy difference is small compared to the adsorption energy. In a kinetically driven adsorption process, oxygen will nevertheless occupy this site with a finite probability. Furthermore, surface defects can catalyze the occupation of these sites. One example is residual water adsorption. STM data show that the adsorption occurs mainly on the HCC¹¹⁵. Similar to oxygen, the water molecules dissociate. The O and OH components on the HCC then open a band gap of approximately 0.5 eV¹¹⁵.

For Si(553)-Au, the situation is quite different. Here, the Au bands are the main contributor to the surface conductivity. However, the Au atoms are relatively inert to oxidation, and the O atoms prefer to adsorb at the HCC. A comparison of the band structures of the pristine and the oxidized surface depicted in Fig. 4.8(d) and (f) shows that the occupied part of the step-edge band is shifted to higher energies by about 0.1 eV. At the same time, the gap of the anticrossing decreases. Nevertheless, the influence on the dispersive Au bands is limited—and so is the influence on the conductivity. Similarly, the Au bands of Si(557)-Au change only slightly upon O_2 adsorption. The most extensive changes are for the ad- and rest atom bands, of which the latter contributes significantly to electronic transport. The oxidation of Si(557)-Au is,

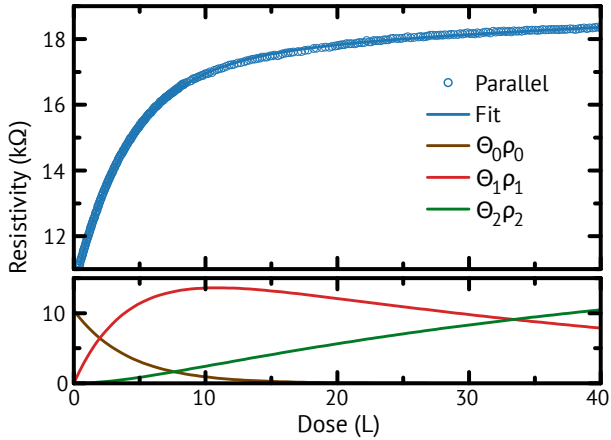


Figure 4.9: The resistivity of the Si(557)-Au surface in the chain direction with respect to the oxygen dose. In the upper part, the experimental data is shown as circles. The solid line indicates the fitted model. The individual components, of which the fitting function is composed, are shown in the lower section. The image is adapted and taken from Ref. [168].

therefore, more significant than for Si(553)-Au, in agreement with the experimental observation.

The here described adsorption scenarios are only part of several mechanisms that impact the overall conductivity. Other contributions, such as potential-well scattering, are expected to have a significant contribution as well. Nevertheless, DFT calculations show that both surfaces have different reactive adsorption sites. These affect the electrical conductivity very differently and provide an insight into why otherwise similar surfaces behave so dissimilar upon oxidation.

4.1.5 Analysis of the Transport Data

Based on the adsorption site analysis on Si(557)-Au by DFT calculations, F. Edler conducted a quantitative analysis of the transport data. The method applied here is only sketched out briefly. For more details, the reader is referred to the original paper in Ref. [168].

Two conduction channels affected by the adsorption of one and two O_2 molecules have been identified. Within the model described here, Θ_0 , Θ_1 , and Θ_2 represent the fractions of the free, single, and double occupied adsorption sites on Si(557)-Au. Naturally, double occupation can only occur if Θ_1 is nonzero. Only first-order adsorption kinetics is assumed within the Langmuir adsorption model, i.e., only adsorption and no desorption is considered. Furthermore, it is assumed that each occupation state affects the total resistivity individually. The overall resistivity is then described by $\rho = \Theta_0\rho_0 + \Theta_1\rho_1 + \Theta_2\rho_2$. In Fig. 4.9, the observed behavior of the resistivity as a function of O_2 dosage is compared with the model presented here. The individual components are also shown in the lower section. This model fits the experimental data very well for all probed doses. In the low-dosage regime, the increase in resistance can be approximated by $\Theta_1\rho_1 = 1 - \exp(-C_0D)$, where C_0 is a constant modeling the sticking coefficient. The value $D_0 \equiv 1/C_0 = 4.1 \text{ L}^{-1}$ agrees well with the decay constant independently obtained by LEED experiments for the $\times 2$ diffraction pattern. For a higher oxygen dose, the adsorption of a subsequent O_2 molecule becomes the dominant driver for an increase in resistance.

Although only elementary total-energy calculations—in contrast to transport calculations—have been performed here, the adsorption mechanisms and their influence on the conductivity could be explained in agreement with the experiment.

4.2 Probing Quasi-1D Electronic Excitation Spectra by DFT-Aided Plasmon Spectroscopy

DFT excels in total-energy calculations or in determining the atomic structure for a vast amount of materials. In the previous section, conclusions were drawn about the electrical conductivity of Si(553)-Au and Si(557)-Au using DFT band structures. Such band structure analyses work well if the character of whole bands changes or if the changes occur mostly in the occupied part. However, it is a fundamental problem of (semi-)local DFT to model the correct energies of unoccupied bands¹⁷⁹.

In this section, a new method is applied to make more robust predictions about the electronic excitation spectrum of quasi-1D systems. In principle, parts of the unoccupied bands can be derived from the experimental plasmon loss spectrum. For this purpose, the lower limit of the electron-hole (e-h) excitation continuum gained from the *ab initio* band structure is additionally required. This method was developed by Lichtenstein *et al.* (Leibniz Universität Hannover) and tested in collaboration on three different systems: Si(335)-Au, Si(557)-Au, and Si(775)-Au. In the context of this dissertation, the band structures of Si(557)-Au and Si(775)-Au were provided, and the method was collaboratively tested and discussed. In the following, only these two systems are discussed in detail. Later on, the same approach is taken to probe the oxidized Si(557)-Au surface, based on the adsorption sites and band structures that were discussed in the previous section. The results were published in Refs. [167, 180], and the following subsections are based on these papers.

4.2.1 Plasmon spectroscopy

Excited collective states of a material, such as plasmons, can be measured using experimental methods such as electron energy loss spectroscopy (EELS). The small penetration depth of low-energy electrons makes EELS particularly sensitive to surfaces. It is thus well suited for the investigation of atomic wire systems.

In contrast to 4PP, which probes the electronic bands near the Fermi energy, plasmon spectroscopy is sensitive to the unoccupied states between 100 meV and 1 eV¹⁶⁷. Furthermore, disorder affects plasmon loss dispersions only at long wavelengths, and the spectra are also insensitive to SCL contributions¹⁶⁷. Plasmon spectroscopy can thus be considered a viable supplement to DC conductance measurements, and a comparison between both methods is drawn at the end of this section.

The plasmon dispersion relation of a 1D system can be derived from a confined 2D nearly free electron gas (NFEG)^{181,182}. There is a fixed relationship between the 1D plasmon dispersion relation and the continuum of e-h excitations. In the case of a confined NFEG, the upper and lower boundary of this continuum ω_+ and ω_- are given by

$$\omega_{\pm}(k_{\parallel}) = \hbar \frac{k_{\parallel}^2 \pm 2k_{\parallel}k_F}{2m^*}. \quad (4.1)$$

Here, k_{\parallel} is the wave vector in the direction of the 1D system, and m^* denotes the effective mass of the majority charge carrier. The plasmonic dispersion relation is independent of the exact form of $\omega_{\pm}(k)$ and is given by¹⁸²

$$\omega_p(k_{\parallel}) = \sqrt{\frac{\omega_+^2(k_{\parallel})e^{A(k_{\parallel})} - \omega_-^2(k_{\parallel})}{e^{A(k_{\parallel})} - 1}} \quad (4.2)$$

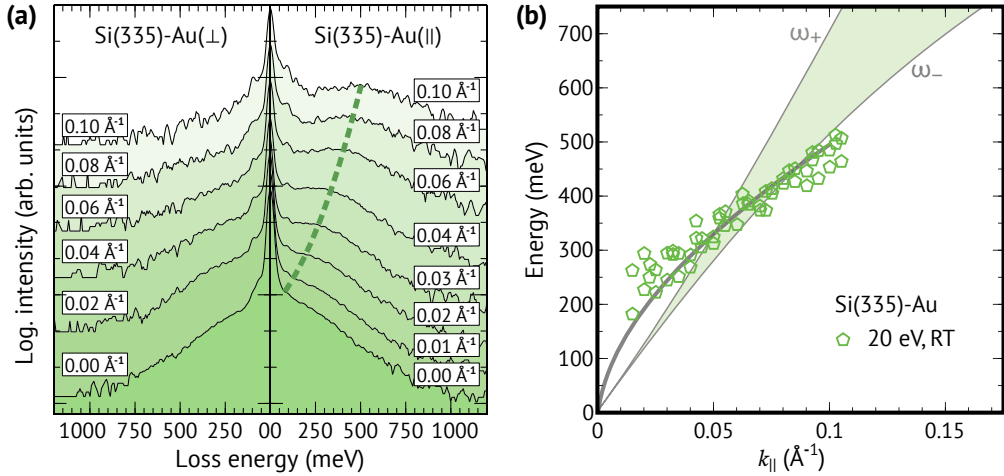


Figure 4.10: (a) Sample EEL spectra of Si(335)-Au measured across (left) and along (right) the wires. The green dashed line indicates a dispersive loss only seen in the parallel direction. (b) The plasmonic loss data taken from (a) with respect to the wavevector k_{\parallel} compared with the e-h continuum (green area) derived under the assumption of a confined NFEGR. The thick solid line indicates the fit of the plasmonic dispersion according to Eq. 4.2. The image is adapted and taken from Ref. [180].

for a 1D system, where

$$A(k_{\parallel}) = \frac{\hbar^2 2\pi k_{\parallel}}{m^* g_s V(k_{\parallel}) [1 - G(k_{\parallel})]}.$$

In this equation, g_s denotes the spin degeneracy, $V(k)$ the confining potential in reciprocal space, and $G(k)$ is a local field correction factor, which describes modifications of $V(k)$ due to exchange-correlation effects. It is emphasized that Eq. 4.1 is restricted to a confined NFEGR, while Eq. 4.2 is also valid beyond the scope of an NFEGR. The confining potential $V(k)$ can, e.g., be modeled by a simple square well or a harmonic potential. In practice, the exact potential of the Au wires has a more complex form, and coupling between adjacent wires also needs to be considered. An approximate description for this coupling exists in the small- k limit^{181,183,184}. Nevertheless, this model is robust against the exact form of the confining potential, and significant changes in the plasmon dispersion appear only at very small k .

A thorough analysis of Eq. 4.2 shows that the plasmon dispersion is always located above the continuum of the e-h excitations and merges into ω_+ for short wavelengths¹⁸¹. In 1D, it has a very simple form and exhibits a linear dispersion to the lowest order in k .

Fig. 4.10(a) shows an exemplary EEL spectrum for Si(335)-Au in the direction parallel (k_{\parallel}) and orthogonal (k_{\perp}) to the wires. Dispersive loss peaks are only visible along the wires. Additionally, the exponential drop of the signal near $k = 0$ is known as the Drude tail¹⁴⁴. It is a characteristic property of metallic systems. Fig. 4.10(b) illustrates the measured plasmonic dispersion for the same system. The data is fitted according to Eq. 4.2 within the NFEGR model. Despite the satisfactory agreement between the fit and the experimental data, this model cannot be correct. As the plasmon dispersion transects the e-h continuum, a strong dampening of the plasmon by the e-h excitation continuum would occur. The plasmon dispersion is even below the lower limit of the e-h continuum for larger k_{\parallel} , leading to imaginary solutions. Similar results are obtained when the NFEGR model is applied to Si(557)-Au and Si(775)-Au, as shown in Fig. 4.11. For Si(557)-Au, the results slightly improve. However, the plasmon dispersion curve still crosses the e-h continuum. In contrast, the discrepancies for Si(775)-Au worsen, as most of the plasmon dispersion is below the lower limit of the e-h continuum.

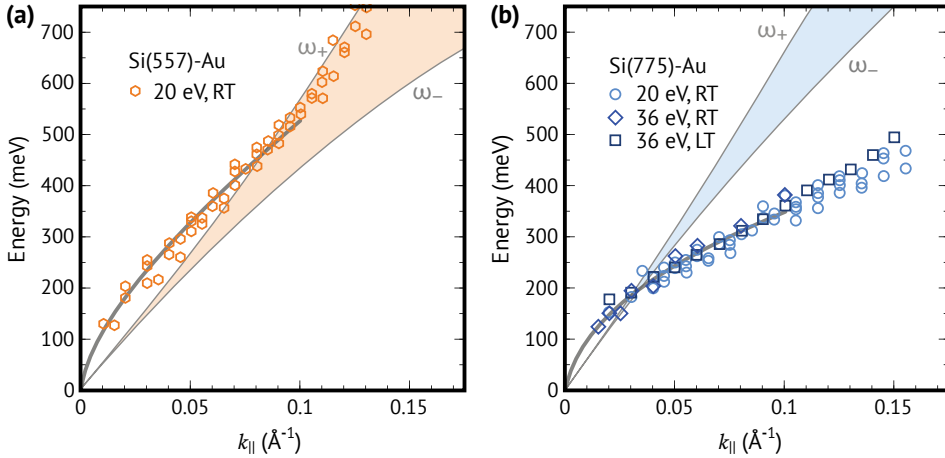


Figure 4.11: Plasmon dispersions of (a) Si(557)-Au and (b) Si(775)-Au with respect to the wavevector k_{\parallel} compared to the e-h continuum (colored area) derived under the assumption of a confined NFEGB. The thick solid lines indicate the fit of the plasmonic dispersion according to Eq. 4.2. The image is adapted and taken from Ref. [180].

Overall, a confined NFEGB describes Au atomic wires only insufficiently. In these systems, the Au bands are the main contributor to the plasmonic signal. As described in the previous section, these, however, are strongly hybridized with Si surface states. The same applies to Si(775)-Au¹⁰⁸. Therefore, no free-electron behavior should be expected.

In the following, a different approach is followed. Instead of modeling the upper and lower limits of the e-h continuum within a confined NFEGB, the lower limit ω_- can also be determined from the DFT band structure. This is achieved by fitting a parabolic function to the relevant part of the band structure. Typically, this is the highest occupied or lowest unoccupied band in the case of dominant electrons or holes. In this way, the course of ω_- can be predicted for all k_{\parallel} . The upper limit ω_+ can then be computed with the knowledge of ω_- and ω_p . The latter is taken by the averaged values of the measured plasmon dispersion curve at each k_{\parallel} . Solving Eq. 4.2 for ω_+ then yields predictions for the unoccupied bands. This approach is tested for the clean Si(557)-Au and Si(775)-Au as well as for the oxidized Si(557)-Au surfaces.

4.2.2 Electronic Excitation Spectrum of Clean and Oxidized Si(557)-Au

Clean Si(557)-Au

Si(557)-Au is very similar to Si(335)-Au, as both surfaces exhibit only a single strand of Au atoms per terrace. The associated EEL spectrum displayed in Fig. 4.12(a) therefore closely resembles that of Si(335)-Au. The presence of a single Au strand makes the treatment of both surfaces relatively easy because it implies only a single dispersive Au band. This band is primarily responsible for the measured plasmon dispersion depicted in Fig. 4.12(b). Interaction with other Si surface bands, however, introduce small electronic gaps into the band structure. This is particularly true for the unoccupied bands. The DFT band structure of Si(557)-Au limited to the surface bands is shown in Fig. 4.12(b). A Gaussian distribution with an FWHM of 3.3 Å models the confining potential. This corresponds to a single Au wire and is equivalent to a harmonic potential of width 1.4 Å or a square-well potential of width 6.6 Å.

The small electronic gaps in the surface bands of Si(557)-Au complicate the extraction of ω_- . For this reason, two approaches were conducted, assuming dominant electrons or dominant holes within a

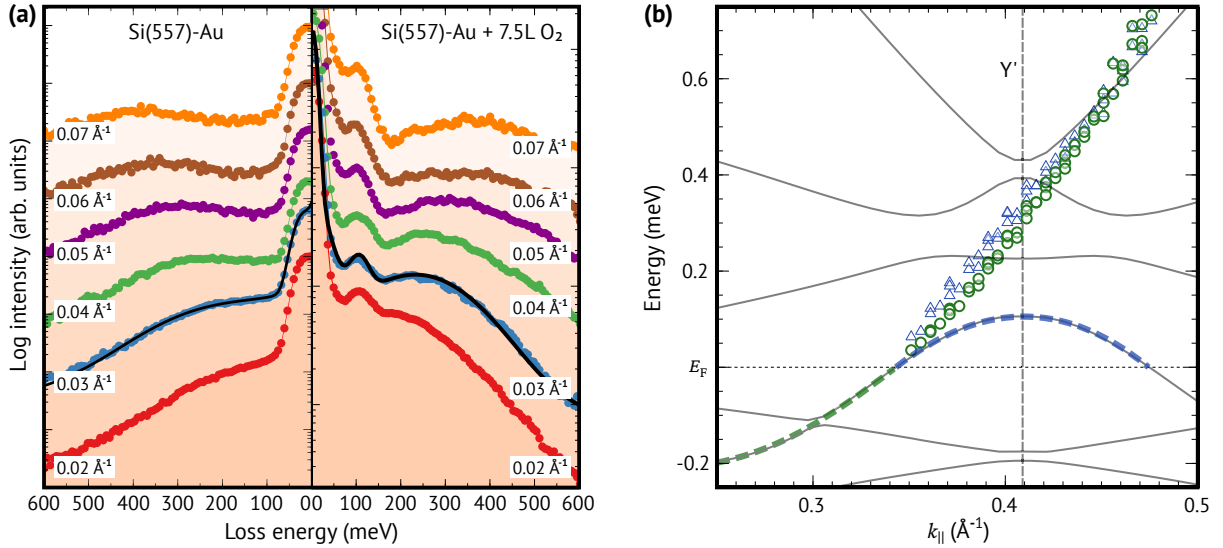


Figure 4.12: (a) EEL spectra of Si(557)-Au without (left) and with (right) 7.5 L of O₂ in the direction along the wires. (b) Section of the surface bands together with the overlayed derived dispersion of ω_+ (circles and triangles). The green (blue) dashed line indicates a parabolic fit of ω_- to the underlying occupied (unoccupied) bands assuming dominant electron (hole) excitation. Green circles (blue triangles) show ω_+ , as calculated by Eq. 4.2 using ω_- and the measured plasmon dispersion (cf. Fig. 4.11(a)). The image is adapted and taken from Refs. [167, 180].

quasi-free particle picture. In the first scenario, ω_- is taken from the uppermost occupied band (see the green dashed line in Fig. 4.12(b)). The curvature obtained from a parabolic fit of this band corresponds to an effective mass of $m^* = 0.23 m_e$. In the second scenario, ω_- is taken from the lowest unoccupied band (see the blue dashed line in Fig. 4.12(b)). The negative curvature of this band is equivalent to an effective mass of $m^* = 0.5 m_e$. The resulting values of ω_+ for both scenarios are plotted in Fig. 4.12(b) as green circles and blue triangles. Only for lower excitation energies, there exist some small deviations. Overall, the deviations are insignificant and depend only to a small extent on the choice of ω_- .

The calculated values of ω_+ in Fig. 4.12(b) are in good agreement with the unoccupied band starting at 0.45 eV. In contrast, the bands with low dispersion and the small band gaps are poorly modeled. The upper limit of the e-h excitation continuum seems to be insensitive to these gaps. Several mechanisms are possible that could limit the visibility of these gaps in the plasmonic dispersion curve: (i) The average length of the Au wires limits the lifetime of the plasmons, which in turn leads to lifetime broadening. For this system, a lifetime broadening of $\Delta E \geq 20$ meV is estimated and thus will not dominate. (ii) e-h pairs with excitation energies within the range of the electronic gap can be further excited. In this case, the band gaps would be effectively integrated over. (iii) There is a chance that plasmonic excitations are limited to delocalized electrons, only. Since the band gaps result from hybridization between Au and more localized Si states, these are not “seen” by the plasmons.

In summary, the plasmonic dispersion and the upper limit of the e-h continuum are most sensitive to the parts of the single-particle band structure with a high free-electron character. Other parts, e.g., non-dispersive bands or band gaps, are not resolved.

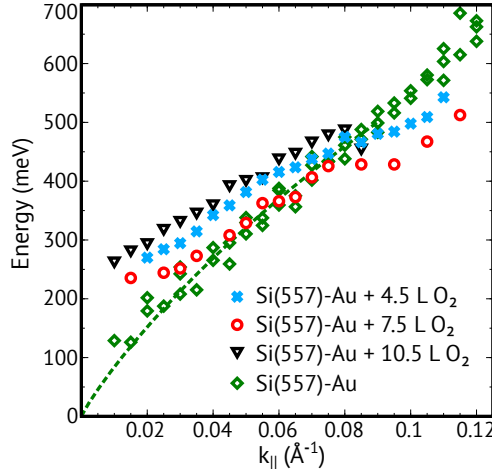


Figure 4.13: Plasmon dispersion of the pristine (green) and oxygen-adsorbed (blue, red, black) Si(557)-Au surface for various O_2 doses. The green dashed line indicates the fit according to Eq. 4.2. The image is adapted and taken from Ref. [167].

Oxidized Si(557)-Au

The influence of oxygen atoms on the conductivity of Si(557)-Au was already discussed in detail in section 4.1. However, DC conductivity measurements are sensitive only to the changes in unoccupied bands near E_F . In order to investigate the influence of oxygen atoms on the energetically higher bands, an EEL spectrum was recorded for the oxidized surface at various O_2 doses. The corresponding spectrum is shown on the right-hand side of Fig. 4.12(a) for a dose of 7.5 L.

Contrary to expectations, oxygen adsorption does not lead to a decrease in the plasmon loss energy. Instead, a partial increase in energy is observed. The most significant change compared to the pristine surface is a new loss peak at ≈ 110 meV. This loss peak is a fingerprint of Si-O vibrations and provides further evidence for the dissociative behavior of adsorbed O_2 on Si(557)-Au. In contrast, the plasmonic loss due to the Au band is almost unaffected. This is particularly remarkable because the adsorbed oxygen introduces a high degree of disorder to the surface.

Fig. 4.13 compares the plasmon dispersions of the surface exposed to 4.5 L, 7.5 L, and 10.5 L of O_2 with the clean surface. At low k_{\parallel} , the energies of the plasmonic loss of the oxidized surfaces are well above the energies of the clean surface. Simultaneously, the slopes are reduced, leading to finite plasmon loss energies in the limit of $k_{\parallel} \rightarrow 0$. Only severe changes in the band structure can explain such drastic changes in the plasmon dispersion. In addition, adsorbed oxygen atoms act as scatterers of the plasmonic waves. Above a specific defect density, total reflections and standing waves arise. Consequently, finite plasmon loss energies emerge in the long-wavelength limit. In contrast, a fit of the plasmon dispersion of the clean surface according to Eq. 4.2 exhibits an almost linear behavior and zero offset, as illustrated in Fig. 4.13.

Again, the upper limit of the e-h excitation continuum ω_+ can be determined by the lower limit ω_- and the experimental plasmon dispersion. In the last section, adsorption models for O_2 on Si(557)-Au were discussed, and band structures for these models have been calculated. Here, the band structures of two particular models are taken for the extraction of ω_- and the analysis of ω_+ : Ad_{ins}^2 and $\text{Ad}_{\text{ins}}^2\text{-eHCC}_{\text{ins}}\text{-mHCC}_{\text{ins}}$. The corresponding atomic models can be found in Fig. 4.5 and Fig. 4.7. A comparison between the band structures of the oxidized and clean surface is depicted in Fig. 4.14(a). As the adatom row becomes oxidized, the bands associated with the ad- and rest atom undergo the most significant changes. In

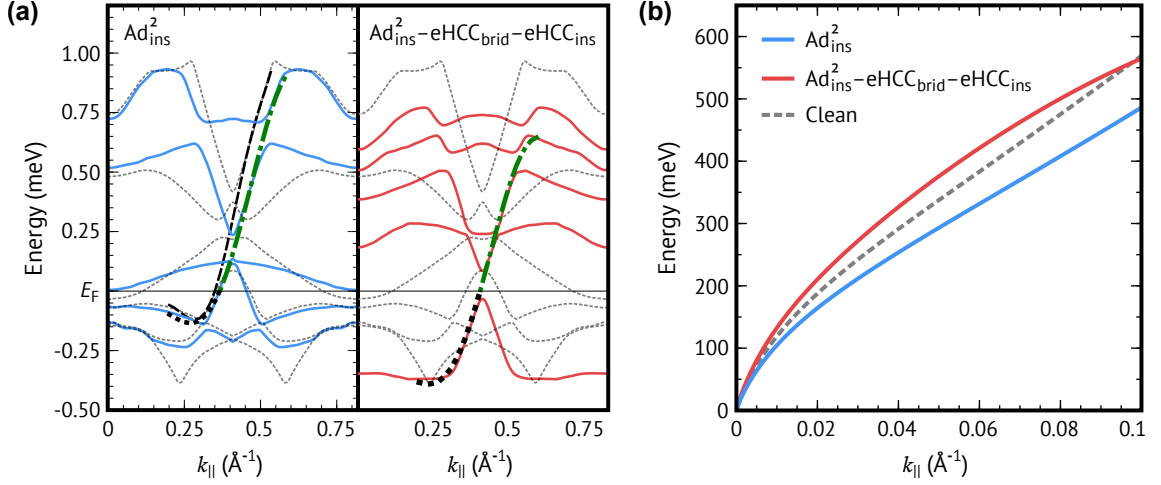


Figure 4.14: (a) Surface bands of the Ad_{ins}^2 (left, blue) and the $\text{Ad}_{\text{ins}}^2\text{-eHCC}_{\text{ins}}\text{-mHCC}_{\text{ins}}$ (right, red) oxidation model of Si(557)-Au. The black dotted line below E_F is the parabolic band taken for ω_- , while the green dashed line is the resulting ω_+ . Gray and black dashed lines indicate the surface bands and ω_+ of the clean surface for comparison. (b) Upper limit of the e-h excitation continuum of the clean and oxidized surfaces. The image is adapted and taken from Ref. [167].

contrast, changes to the bands with Au character are less significant. For a more detailed analysis of the band structure changes due to O_2 adsorption, the reader is referred to section 4.1.4.

Same as before, the excitations from the highest occupied band to the Fermi energy define the lower limit of the e-h excitation continuum. A parabolic fit to this band gives well-defined values for ω_- for all k_{\parallel} . For instance, the parabola fitted to Ad_{ins}^2 yields an effective mass of $m^* = 0.23 m_e$. In both cases, ω_+ , indicated by green dashed lines in Fig. 4.14(a), follows the measured plasmon dispersion ω_p very closely. Only near the Fermi energy, the influence of ω_- is more decisive, and the deviations become larger. As for the rest, the results are very similar to those of the clean surface: While small electronic gaps are integrated over, ω_+ is otherwise in good agreement with the calculated unoccupied bands. In addition, the upper limit of the e-h excitation exhibits a linear dispersion over large parts, similar to the clean surface.

Fig. 4.14(b) gives a better overview of the calculated ω_+ . Compared to the pristine surface, the most significant difference of the Ad_{ins}^2 model is the decrease of the average slope by about 15%, as illustrated by the gray dashed and blue lines. As a consequence, ω_+ is lower over the whole k_{\parallel} -space. In contrast, the simultaneous oxidation of the Si adatom as well as the HCC leads to an increase of ω_+ compared to the clean surface. However, at $k_{\parallel} = 0.1 \text{ \AA}^{-1}$, the upper excitation limit of $\text{Ad}_{\text{ins}}^2\text{-eHCC}_{\text{ins}}\text{-mHCC}_{\text{ins}}$ and of the pristine surface intersect. For $k_{\parallel} \leq 0.1 \text{ \AA}^{-1}$, the energy of the plasmon dispersion is elevated. Furthermore, an up and down shift of the oxidized band structure is observed in Fig. 4.14(a), depending on the degree of oxidation. Nevertheless, the calculated upper edge of the e-h excitation spectrum is mainly determined by the highly dispersive Au bands.

Overall, the calculated ω_+ coincides closely with the measured ω_p and corresponds well with the calculated band structure. Especially the nonmonotonic shift is well reproduced by the DFT band structures. However, it should be noted that the modeling occurred within perfect periodic unit cells, same as in the previous section. Effects of empty or mixed adsorption sites are therefore not considered. Nevertheless, the plasmon spectra show, just like the DC conductivity measurements, that the oxygen interferes with the metallic properties but does not destroy them. EELS, in combination with DFT band structure calculations, can therefore be considered as a valuable addition to DC conductivity measurements.

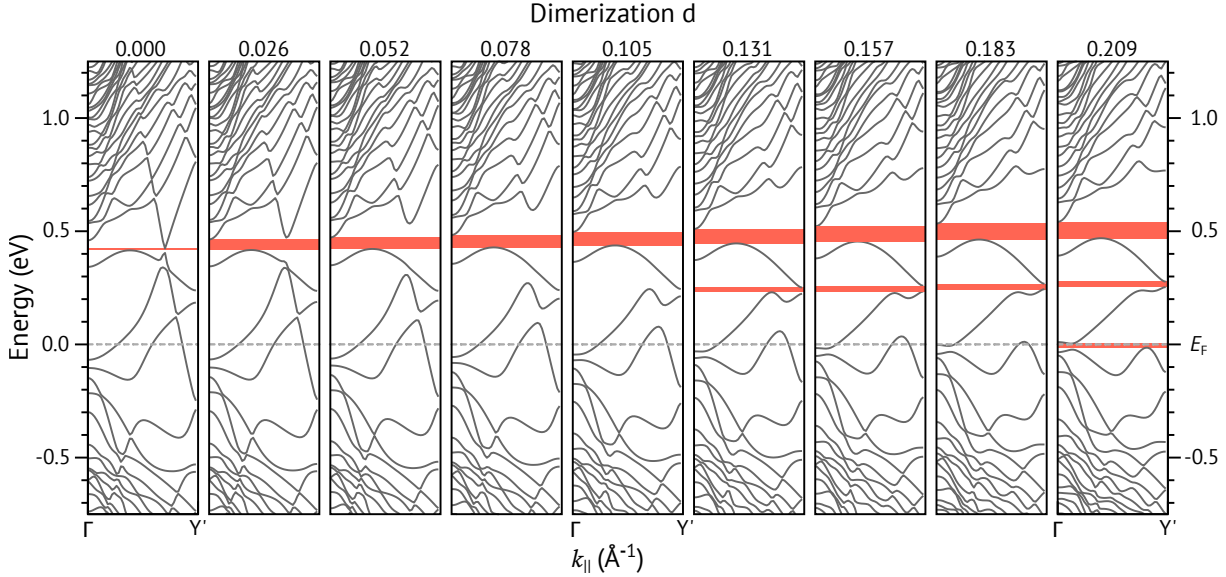


Figure 4.15: Band structure of Si(775)-Au in the direction parallel to the wires for several set dimerizations d . Band gaps are indicated in red.

4.2.3 Electronic Excitation Spectrum of Clean Si(755)-Au

The atomic geometry and band structure of Si(775)-Au have already been discussed in detail in my master thesis¹⁸⁵. In the following, only novel findings for this system are reported. In addition, previously published properties are only mentioned here if they are relevant for the plasmon loss analysis. For further information on this system, the reader is referred to the associated paper and thesis in Refs. [108, 185].

Band structure calculations show that Si(775)-Au has two dispersive metallic bands—labeled $S_{1/2}$ and S_3 ¹⁰⁸. These bands are also visible in ARPES, where the $S_{1/2}$ band is Rashba-split¹⁰. According to DFT calculations, unpaired electrons reside in the DBs of the Si rest atoms. The magnetic ordering has a stabilizing energy of 0.1 eV per spin site¹⁰⁸. However the system is magnetically disordered at room temperature, and thus only the spin-averaged band structure is considered here.

Similar to the situation at Si(557)-Au, the Au bands hybridize with the Si surface atoms of the HCC and the rest atoms. As a result, electronic gaps open in the occupied part of the $S_{1/2}$ and S_3 bands. Similarly, electronic gaps are also present in the unoccupied part of these bands due to hybridization. In fact, there is a strict correlation between the dimerization

$$d = \frac{|a_1 - a_0|}{a_0} \quad (4.3)$$

of the Au chain and the electronic gaps above E_F . Here, a_0 denotes the surface lattice constant and a_1 the distance between the Au atoms forming the dimer. Compared to PBE ($d_{\text{PBE}} = 0.108$), the dimerization is almost twice as large within the local-density approximation (LDA) with $d_{\text{LDA}} = 0.187$. In LDA, the larger dimerization is accompanied by an increase in existing and the creation of additional electronic gaps.

To elaborate on this, band structure calculations within PBE were carried out for several different dimerization values. For this, the dimer distance of the Au atoms was manually set and fixed during relaxation. The associated band structures are depicted in Fig. 4.15. In the absence of Au dimers ($d = 0.0$), only a small band gap approximately 0.4 eV above the Fermi energy exists. With increasing dimerization, this

gap steadily grows until a second gap opening at ≈ 0.25 eV occurs for $d = 0.131$. This trend continues until eventually a band gap opens up at the Fermi energy for $d = 0.209$. These band gaps, among others, cause the breakdown of the NFEG model and lead to the inconsistencies already discussed in the context of Fig. 4.11 on page 48.

Similar to Si(335)-Au, the EEL spectra of Si(775)-Au exhibit a Drude tail, confirming the metallicity of the system¹⁸⁰. However, only one characteristic shoulder associated with a single loss signal is visible in the spectra. This is in contrast to the two dispersive bands seen in both ARPES¹⁰ and DFT¹⁰⁸. However, due to the limited energetic resolution of ARPES, it is not clear whether both bands reach the Fermi energy. Regarding Fig. 4.15, it should be noted that the DFT band structures are also subject to change with respect to the chosen exchange-correlation functional or chosen dimerization. Consequently, two separate loss signals associated with each band would have been expected. Fig. 4.16 illustrates the surface bands calculated with the PBE and HSE06 functional. The latter is a hybrid functional developed by Heyd, Scuseria and Ernzerhof (HSE), where the exact exchange from Hartree-Fock theory replaces 25% of the local electron exchange¹⁸⁶. Hybrid functionals can improve the DFT results of the unoccupied bands considerably if the fraction of exact exchange is carefully chosen.

Furthermore, Fig. 4.16 highlights the $S_{1/2}$ and S_3 Au bands in the DFT band structure based on the shape of the metallic bands, as seen in ARPES¹⁰. Within the above considerations, only the $S_{1/2}$ band cutting the Fermi energy at $k_F = 0.365 \text{ \AA}^{-1}$ can be responsible for the observed plasmon loss. At this point, the Au band has the highest dispersion and should be the most visible. The other bands crossing the Fermi energy exhibit a lower dispersion and are thus not observable in the EELS experiment conducted here.

A parabolic fit of the $S_{1/2}$ band yields an effective mass of $m^* = 0.08 m_e$, which was used for the lower limit of the e-h excitation continuum ω_- . Additionally, the confining potential is modeled by a Gaussian distribution with a FWHM of 6.6 \AA . The low effective mass leads to a large $A(k)$ so that the measured plasmon dispersion almost entirely determines ω_+ . Fig. 4.16 compares ω_+ , depicted as blue circles, to

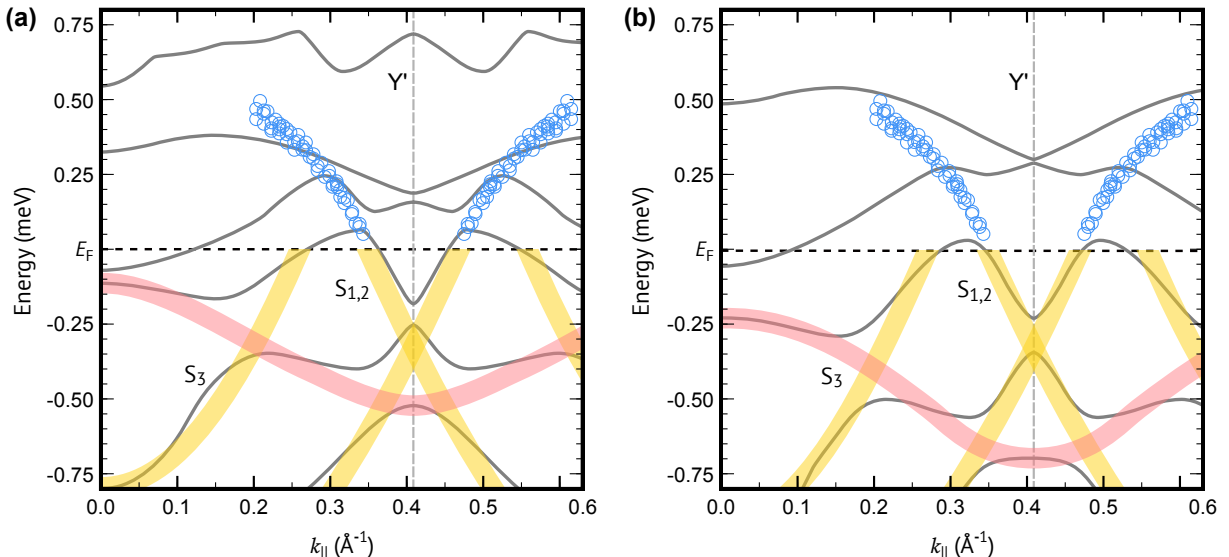


Figure 4.16: Surface bands (gray lines) of Si(775)-Au calculated with the (a) PBE and (b) HSE06 functional. The dispersive Au bands are highlighted in yellow and derived from the DFT band structure and the ARPES data. Blue circles mark the dispersion of the upper limit of the e-h continuum ω_+ derived from the $S_{1/2}$ band. The step-edge band is shown in red. The image is adapted and taken from Ref. [180].

the PBE and HSE06 band structure. For both functionals, ω_+ crosses two band gaps and levels off near 0.5 eV. In the hybrid band structure, a band at the same energy appears to confine the upper limit of the e-h continuum, and ω_+ seemingly adapts to the course of this band. In comparison, ω_+ terminates in the middle of a band gap in the case of PBE. However, ω_+ needs to cover smaller distances by crossing the narrower band gaps for PBE.

In summary, ω_+ , as well as the Au bands, fit better to the HSE06 band structure. The behavior is qualitatively similar to the Si(557)-Au surface described above¹⁸⁰.

[...] but I shall certainly admit a system as empirical or scientific only if it is capable of being tested by experience. These considerations suggest that not verifiability but the falsifiability of a system is to be taken as a criterion of demarcation.

Karl Raimund Popper

5

Low-Temperature Structure of Si(553)-Au

Although the Krawiec model is consistent with most experimental results at room temperature, it cannot reproduce many experimental observations specific to low temperatures (LTs). In the last two decades, several other atomistic models have been proposed. A detailed overview of the historical development for Si(553)-Au is given in section 3.3.1. The latest structural model, called the spin-chain (SC) model, is consistent with many experimental observations at LT¹³. Unlike previous models, it can explain both the $\times 2$ and the $\times 3$ periodicity observed in ARPES¹⁰, STM¹³, and XRD^{127,187}. Its central components are a double strand gold chain and an HCC¹²⁶. In the latter, every third step-edge atom exhibits a magnetic moment. Along the chain, the magnetic order is antiferromagnetic. However, due to the 2D arrangement in a triangular lattice, the system is in a frustrated state¹²⁰.

The SC model is of particular interest for two reasons: First, Si atoms rather than metallic atoms host the unpaired electrons—a rather uncommon structural theme. Second, it explains the origin of the $\times 3$ periodicity at the step edge for the first time, which is due to the lowered position of the spin-polarized step-edge atoms.

However, the SC model raises several questions: Normally, unpaired electrons are avoided on Si surfaces by the specific surface reconstructions. One prominent example is the Si(100) surface. Here, the unsaturated surface atoms are arranged in a way that avoids unpaired spins. This is achieved by a buckled arrangement of Si dimers⁶³. If the SC structure correctly describes the ground state at LT, the presence of Si surface atoms hosting unpaired electrons would be at least a novelty. Moreover, it should be noted that surface spins have not been measured to date—even in spin-polarized STM. In ARPES, experimental evidence is also missing: The occupied part of the surface band originating from the spin-polarized DBs was not detected^{10,13}.

Therefore, a reliable atomic structure in agreement with the experiments at LT is paramount for further investigations. This is especially true for the observed phase transition, which involves structural¹¹³ as well as electronic modifications¹²⁴. In this chapter, a new atomic model without the need for half-filled DBs is derived. This structural model also explains the $\times 3$ periodicity and agrees well with the available experimental data. The results were published in Ref. [188].

5.1 Structure Determination

5.1.1 Methodology

The computational details mostly match the parameters described in section 4.1.3. However, a larger (5×6) unit cell is utilized to fit both $\times 2$ and $\times 3$ periodic structural motifs. The sampling of the Brillouin zone (BZ) is adapted accordingly to a Monkhorst-Pack¹⁸⁹ mesh of $2 \times 5 \times 1$. Furthermore, the PBEsol functional with an energy cutoff of 450 eV is used. In comparison to PBE, it is designed to improve the lattice parameters of bulk solids and their surfaces¹⁹⁰. However, this is at the expense of the accuracy of atomization energies¹⁹¹. Collinear spin orientation accounts for potential spin-polarized structural motifs.

5.1.2 The Rehybridized Model

From vicinal Au-covered surfaces, it is known that an HCC stabilizes the step edge^{10,80}. This is unlikely to change for Si(553)-Au. The other structural motif is a double-stranded Au chain, which is experimentally confirmed by XRD¹⁸⁷.

Starting with the SC model, the HCC's unpaired electrons can be remedied in two ways: by pairing or by removal from the DBs. Pairing the electrons of the singly occupied DBs leads to a newly filled and empty DB. Hence, a $\times 6$ periodicity would arise, which is not observed in the experiment. As an alternative, evenly redistributing the charge among the step-edge atoms leads to DBs filled by 5/6 electrons (per spin channel). However, this structure corresponds to the already proposed Krawiec (K) model¹²⁶ and lacks the required $\times 3$ periodicity. It would neither help to transfer electrons from the Au chain—which serves as an electron reservoir¹⁹²—and fill all DBs. A structural motif with $\times 3$ periodicity would still be missing.

Alternatively, the unpaired electrons could move from the DBs back to the Au chain. In this case, two out of three DB were entirely filled, while every third one was empty. Silicon preferentially binds in an sp^3 -hybridized geometry. The same is true for the step-edge atoms. Nonetheless, empty orbitals in an sp^3 -hybridized geometry are energetically unfavorable. Similar to the HCC, Si may also bind in a trigonal-

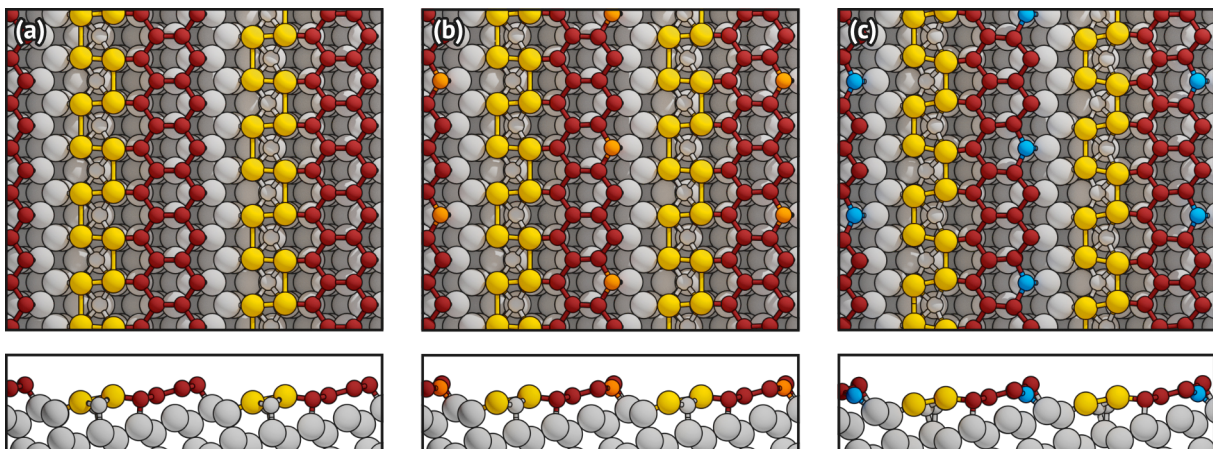


Figure 5.1: The (a) Krawiec (K), (b) spin-chain (SC), and (c) rehybridized (R) model of Si(553)-Au. The main difference between all structures is the position and the accompanying electronic configuration of every third step-edge atom. Big and small gray circles as well as red circles indicate Si bulk and Si HCC atoms, respectively. Additional orange and light blue circles represent Si step-edge atoms with half-filled or empty DB, while yellow circles mark the positions of the Au atoms.

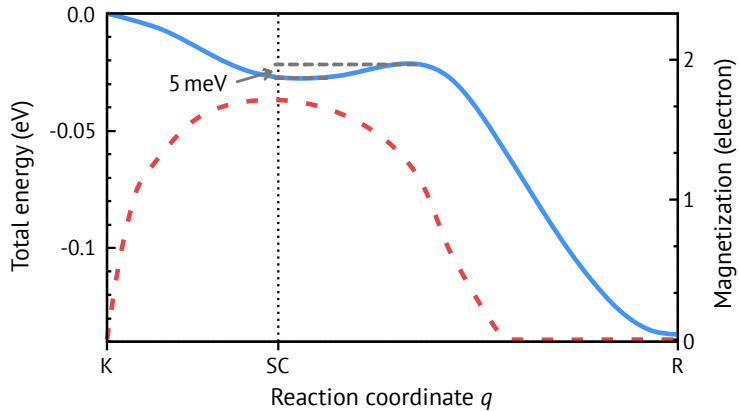
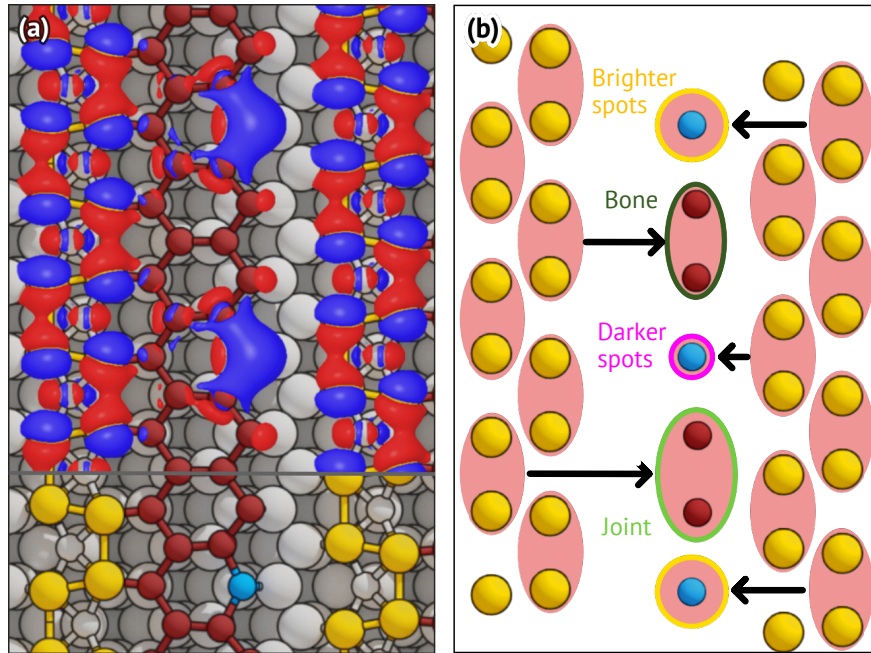


Figure 5.2: Calculated surface energy (solid line) and surface magnetization (dashed line) per (1×6) surface unit cell with respect to the reaction coordinate given by the height of every third step-edge atom for PBEsol. The respective position for the Krawiec (K), spin-chain (SC), and rehybridized (R) model is indicated.

planar geometry. This corresponds to an sp^2 hybridization with an additional p_z orbital. However, this would require a lower position of the corresponding step-edge atom until it lies in one plane with its binding partners. The associated structural model is called the rehybridized (R) model and leads to a diamagnetic electronic structure. The atomic geometries of the K, SC, and R models are illustrated in Fig. 5.1.

The stability of the R model is probed by means of DFT total-energy calculations. Starting from the K structure, the vertical position of every third step-edge atom is lowered until the R structure is reached. Fig. 5.2 depicts the energy profile and surface magnetization along this reaction path. Lowering the height of every third step-edge atom reduces the surface energy while simultaneously increases the surface magnetization. The latter reaches its maximum value for the SC configuration when the position is about 0.3 \AA below the neighboring step-edge atoms. At this position, the system is in a local energetic minimum. As the increase of the magnetization already suggests, a charge transfer takes place among the step-edge atoms. In the K model, all step-edge atoms carry the same charge. However, the lowered step-edge atoms are half-filled, and the other step-edge atoms are completely filled for the SC model.

Indeed, the R structure lowers the surface energy by another 110 meV per (1×6) surface unit cell compared to the SC model. With respect to the latter, a 5 meV high energy barrier must be overcome to reach the global minimum of the PES. It is characterized by a step edge where every third atom is lowered by about 0.8 \AA compared to its neighbors. These atoms rehybridize from an sp^3 to an $sp^2 + p_z$ bonding configuration. As a result, the rehybridized step-edge atoms slightly distort the HCC. A surface charge transfer accompanies these structural changes. Approximately 1.6 electrons per surface cell move from the step edge to the Au chain. This is roughly the amount of unpaired electrons found in the SC model's DBs. Fig. 5.3(a) visualizes the charge redistribution by plotting the difference of the SC and R models' electron densities. The charge transfer from the step edge to the Au dimers is clearly seen. Due to the additional charge, the dimerization of the Au chain increases from 5% to 14% (cf. Eq. 4.3). A similar observation was made by Conor *et al.*, who observed an increase in dimerization by electron doping¹⁹².



5.2 Influence of the Exchange-Correlation Functional on the Stability

Some structural and electronic changes involved in the SC \rightarrow R transition have a negative effect on the surface energy. For instance, the spin-spin exchange energy of about 15 meV¹²⁰ and the strain introduced to the HCC both favor the SC surface. However, the energy gain of both the emptying of the DB and the charge transfer outweighs these factors and stabilize the newly found atomic structure.

Nevertheless, the energy difference between the two structures depends sensitively on the exchange-correlation (XC) functional. Tab. 5.1 lists the surface energies for several XC functionals with respect to the K structure. While PBEsol calculations predict the lowest surface energy for the diamagnetic surface, PBE is incapable of finding a stable R geometry. The respective PBE surface energy of the R model obtained by the frozen PBEsol geometry surpasses the SC model's surface energy. The opposite is true for the LDA functional: Here, DFT calculations fail to identify spin-polarized states, while a diamagnetic step edge minimizes the surface energy.

Strongly localized electrons with weak interaction—as found in the DBs of the step-edge atoms—sensitively depend on the methods applied. DFT often fails to stabilize such delicate features due to its

Model	Surface energy (meV)			
	LDA	PBE	PBEsol	HSE
SC	N/A [†]	-36 [‡]	-26	-419*
R	-114	+191*	-137	-457*

Table 5.1: Surface energies (per (1×6) surface unit cell) of the SC and R model with respect to the K model using different XC functionals. *The energies refer to calculations based on the frozen PBEsol structure. [†]LDA fails to converge to a spin-polarized electronic structure. [‡]Earlier calculations resulted in slightly lower energies of -41 meV¹³ and -44 meV¹²⁰.

Element	Lattice parameter (Å)			
	Experiment	LDA	PBE	PBEsol
Si	5.431 [†] (0.00%)	5.402 (-0.53%)	5.468 (+0.68%)	5.436 (0.09%)
Au	4.078 [†] (0.00%)	4.063 (-0.38%)	4.173 (+2.32%)	4.099 (0.52%)

Table 5.2: Experimental lattice parameters of Si and Au bulk compared to the DFT lattice parameters calculated within LDA, PBE, and PBEsol. In the parentheses, the relative deviation from the experimental value is given. [†] The experimental values were measured at room temperature and taken from Ref. [195].

spurious, intrinsic self-interaction¹⁹³. Regarding strong localization, hybrid functionals improve upon semi-local calculations in many cases. Here, the HSE functional is utilized to verify the most stable surface configuration. A portion of 11% exact Hartree-Fock exchange was found to well describe Si DBs¹⁹⁴ and was used in earlier calculations for Si(553)-Au¹⁴⁶. With HSE, both the R and SC surface are 0.4 eV more stable than the K surface. In fact, all functionals agree that the K model is energetically less favorable at 0 K, but to a smaller degree. But more importantly, the diamagnetic surface structure stabilizes the ground state, in agreement with PBEsol.

A detailed analysis of the Si and Au bulk lattice parameters shows why PBE fails to identify the R structure. Tab. 5.2 gives an overview of the experimental and calculated Si and Au bulk lattice parameters. In general, LDA is known to underestimate lattice parameters, while PBE overestimates them¹⁹⁰. PBEsol improves upon both functionals in terms of bond length accuracy with a slight tendency for overestimation. Typically, small deviations are unproblematic in most cases as long as the relative error is of similar size for the elements of a compound. However, the deviation for the Au bulk lattice parameter is significant within PBE compared to the experimental value. While the relative error for Si is in the per mille range, the Au lattice parameter deviates by a little more than 2.3%. These differences generate additional strain on the Au chains of Si(553)-Au. The electron affinity of the Au dimers delicately depends on the degree of dimerization, which in turn is affected by the strain. Conor *et al.* explain in detail the correlation between additional charge and the degree of dimerization¹⁹². Since the SC→R transition involves a charge transfer from the step edge to the Au chain, the energy balance is put in favor of the SC surface for PBE. A similar behavior is known from the In/Si(111) system, where the LT phase can only be modeled satisfactorily within LDA¹⁹⁶.

Therefore, total-energy calculations support a rehybridized, diamagnetic over a spin-polarized surface structure at LT. Deviations within the PBE functional are explained by an inadequate description of Au by this functional.

5.3 Comparison with the Experiment

The previous section showed that great care has to be taken regarding the computational parameters. This is all the more important since there is no guarantee that structural optimization algorithms used in combination with DFT find the correct ground state. In this section, the R model is validated against some of the available experimental data. More specifically, the calculated band structure is first put into comparison with a measured ARPES spectrum. Moreover, simulated STM images at various tunneling biases are compared with the measured STM images. The same methods are applied to the SC model, and further conclusions are drawn regarding the validity of the R and SC models.

5.3.1 Calculated Band Structures and ARPES

The different charge distribution between the R and SC models is also noticeable in the band structure, as illustrated in Fig. 5.4. The most characteristic bands of the SC surface are the spin-polarized bands 0.1 eV below and 0.2 eV above the valence band maximum. They result from the antiferromagnetic ordering of every third step-edge atom. Each of these bands is associated with one of the two half-occupied step-edge atoms within a (1×6) surface cell. The affiliations are inverted when switching the spin channel. Upon rehybridization, the occupied one of the two bands is also emptied due to the associated charge transfer. Therefore, only a single unoccupied band is visible for the R structure. This empty band extends through the entire BZ and shifts minimally to higher energies. Additionally, the highly dispersive Au bands are more strongly populated and are now entirely below the empty Si step-edge band throughout the BZ.

For comparison, the ARPES spectrum from Ref. [10] is placed behind the band structure in Fig. 5.4(b) and (d). The low-lying Au bands of the R structure agree slightly better with the dispersive bands seen in ARPES. However, the differences are too small to conclude the correct structural model. The same holds for the nondispersing unoccupied band 0.62 eV above E_F that is observed in 2PPE¹⁴⁶. Considering the general band-gap underestimation of DFT, this band can be associated with the unoccupied step-edge band seen for both the R and the SC model. In contrast, an additional occupied step-edge band, about 0.1 eV below the valence band maximum, is only seen for the SC model. This band, which is a signature of spin polarization, has not been detected experimentally. The absence of this band is a strong indication that a rehybridized, diamagnetic step edge characterizes the ground state at LT.

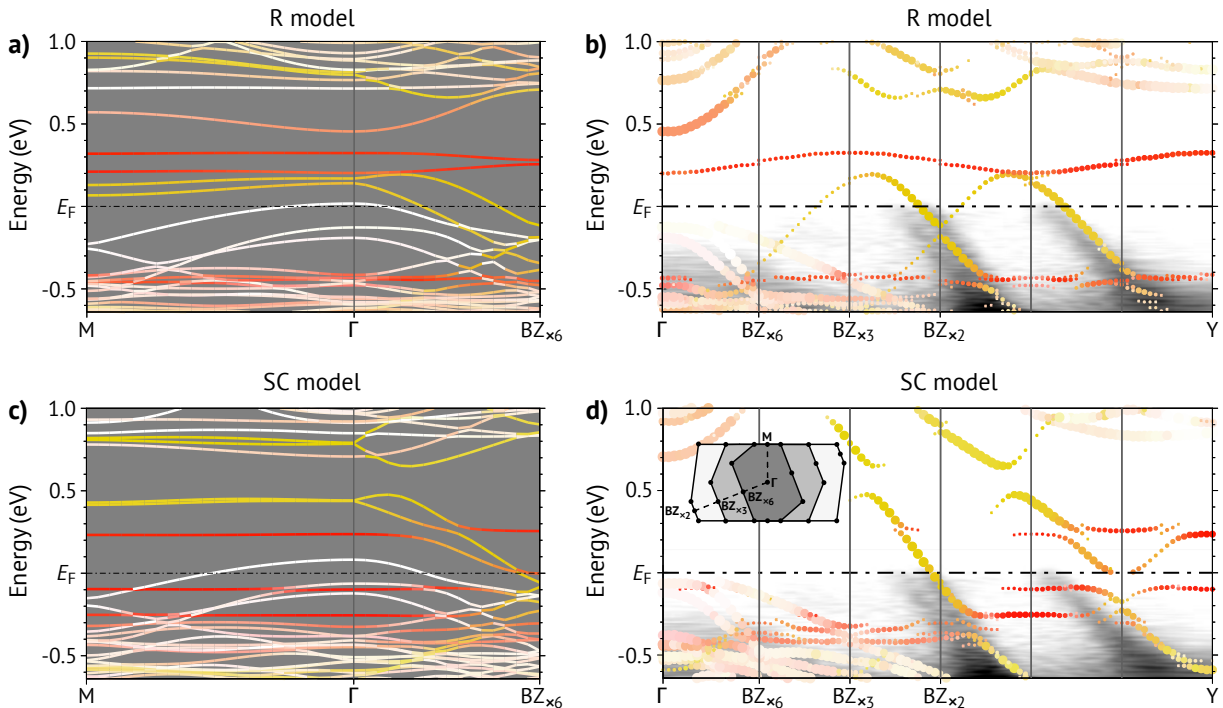


Figure 5.4: Calculated band structure (within a (1×6) unit cell, PBEsol) of Si(553)-Au for the (a) R and (c) SC model. The unfolded band structures (according to Ref. [178]) within a primitive (1×1) surface unit cell are shown in (b) and (d), respectively. The point size in the latter two indicates the $\times 1$ character of the individual state. These are compared with the ARPES data from Ref. [10] shown in the background. The colors indicate the localization at Si step-edge (red) and Au atoms (yellow). The inset in (d) depicts the BZ of the $\times 2$, $\times 3$, and $\times 6$ surface unit cell. The image is adapted and taken from Ref. [188].

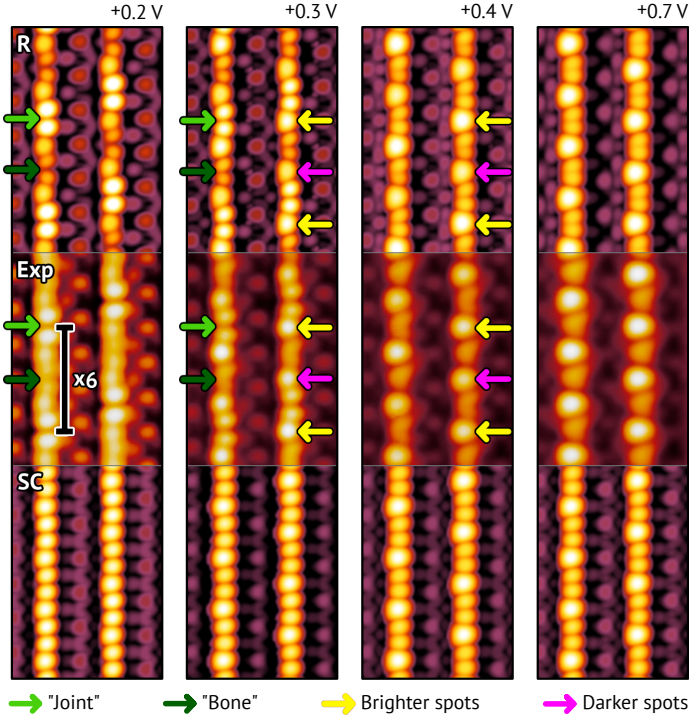


Figure 5.5: Comparison of experimental and simulated (PBEsol) empty-state STM images at different tunneling biases. The simulated STM images of the R and the SC model are shown above and below the measured data in Ref. [121]. Colored arrows mark distinctive features seen in the experiment. The image is adapted and taken from Ref. [188].

5.3.2 Simulated and Experimental STM

The comparison between simulated and experimental STM images is a useful approach to verify the accuracy of atomic structures. STM cannot directly resolve surface atoms but instead probes the electronic states of these. In many cases, however, these are very pronounced and help to distinguish between surface geometries. Here, the Tersoff-Hamann model is used to simulate STM images¹⁹⁷.

Fig. 5.5 depicts experimental LT STM data and the corresponding simulated STM images of the R and SC models. Parallel aligned rows of bright protrusions alternate with dark trenches in these images. These two types of rows correspond to the Si step edge and the Au chain, respectively. For the latter, the associated dark trenches exhibit a $\times 2$ periodicity irrespective of the applied voltage. In addition, the step edge's bright protrusions feature a $\times 3$ periodicity at the highest probed voltage of +0.7 V. The situation is different for biases closer to the Fermi energy, where STM data reveal a $\times 6$ periodic structure at the step edge. This structure resembles “bones” connected to brighter “joints” (see labels in Fig. 5.5). Aulbach *et al.* explain these features by a parity breaking of the step edge caused by the accumulated charge of the Au dimers¹²¹. As the charge interacts with its surrounding, filling the localized DBs of nearby step-edge atoms is penalized, as schematically illustrated in Fig. 5.3(b). As a consequence, the respective states are pushed to higher energies, resulting in an electronic structure of $\times 6$ periodicity. This effect is supposed to intensify with increasing dimerization. Consequently, it should be more prominent in the simulated STM images of the R structure compared to the SC structure.

Both surface structures adequately model the $\times 2$ periodic features for all biases. The same applies to the $\times 3$ periodicity of the step edge at a tunneling bias of +0.7 V. However, as predicted, the $\times 6$ periodic

features are missing in the STM images of the SC model due to the low dimerization of its Au chains. In contrast, the R model reproduces the bone and joint structure in good agreement with the experiment. For intermediate tunneling biases, the simulated STM image of the R surface corresponds roughly to a superposition of the high- and low-voltage structures: While the bones and joints are still visible, the bright protrusions of the Si step-edge atoms with empty DB become visible. However, these alternate with bright and dark intensity. This is, in fact, what experimental STM images of intermediate bias show. Again, the R model reproduces most of the experimental results, while the SC model fails to map these distinctive experimental observations.

In summary, the present study shows that the LT ground state of the ideal Si(553)-Au surface is indeed diamagnetic: Instead of a spin-polarized step edge, all DBs of the step-edge atoms either host spin-paired electrons or are empty¹⁸⁸. This was shown by total-energy calculations, which—with one exception, but due to artificial stress—prefer the R model energetically. Also, comparing the calculated band structures with the ARPES data demonstrates that the R model slightly improves the experimental reproducibility. The excellent agreement between the simulated and experimental STM images is even more evident for the R model. All evidence together univocally suggests that the R model best describes the LT structure of Si(553)-Au.

However, the existence of unpaired electrons should not be ruled out completely. Aulbach *et al.* demonstrate¹⁰³ that point defects in the form of adsorbates can dope the Si(775)-Au surface in such a way that unpaired electrons are likely to form at the step edge. The shallow PES of Si(553)-Au makes it also a promising candidate for creating surface spins by nanostructure engineering¹⁸⁸.

5.4 Transferability of the Rehybridized Model to Si(557)-Au

The Si(553)-Au surface is not the only Si(hhk)-Au surface for which a potential spin-polarized surface structure was predicted. Similarly, every second step-edge atom of the Si(557)-Au surface supposedly host unpaired electrons¹³. Regarding the instability of unpaired electrons in silicon atoms, the question arises whether a diamagnetic, rehybridized structure would better describe the ground state for this surface, too.

Indeed, DFT calculations within PBEsol can stabilize a surface structure with a rehybridized step edge. Compared to Crain *et al.*'s nonmagnetic surface structure with fractional-filled DBs¹⁰, the total energy improves by 43 meV per rehybridized Si step-edge atom. This is slightly lower than the energy gain of 68 meV in the case of the Si(553)-Au surface and is related to the smaller distance of the rehybridized atoms accompanied by a larger distortion and strain on the HCC.

However, the smaller spacing of the rehybridized or spin-polarized step-edge atoms also gives rise to a larger spin-spin exchange energy of 56 meV compared to 13 meV for Si(553)-Au. The energy penalty of the distorted HCC in combination with the larger magnetic exchange tilts the energy scale towards the spin-polarized model. For Si(557)-Au, a surface structure exhibiting an antiferromagnetic ordering cannot be ruled out.

Therefore, rehybridized step-edge atoms do not always replace spin-polarized atoms but should always be considered as a possibility. The subtle interplay of the various energy terms must be reassessed for each surface. This is especially true with regard to the other vicinal Si(hhk) surfaces exhibiting metallic atomic wires other than Au, which have partially not been studied in such depth.

*It is nice to know that the computer understands the problem.
But I would like to understand it too.*

Eugene Wigner

6

Phase Transition of Si(553)-Au

In the previous two chapters, it was demonstrated that the Krawiec (K) model and the newly developed rehybridized (R) model well explain the high-temperature and low-temperature phase of Si(553)-Au, respectively. However, the mechanism that drives the phase transition remains unclear. The measured onsets of the phase transition make this particularly evident: Temperatures in the range of 65 K to 250 K were reported, depending on the measurement method and samples^{112,124}. Furthermore, the measured transition temperature depends sensitively on the defect concentration for many measuring methods^{116,113}. Upon heating, the phase transition is characterized in particular by the disappearance of the $\times 3$ periodicity at the step edge and a sudden jump in conductivity^{113,124}. Further heating of the surface also causes a suppression of the $\times 2$ periodicity¹²⁴. A detailed overview is given in chapter 3.3.3.

In section 6.1, a transition scenario is proposed and analyzed in terms of total-energy calculations. As a next step, *ab initio* molecular dynamics (AIMD) simulations are performed in section 6.2 to better understand the phase transition. In the last section, the derived transition model is compared with available experimental data. The results are published in Ref. [198].

6.1 A Transition Scenario Analyzed by Total-Energy Calculations

According to Ref. [124], the onset of the phase transition is revealed by a sharp increase in surface conductivity at 65 K. The authors suggest that this rapid change originates in a charge transfer from the Au chain to the step edge. Since the rehybridized (R) model describes the LT surface geometry, this is equivalent to a transition from the R to the spin-chain (SC) model. While the step-edge atoms of the former model have a dangling bond (DB) electron configuration of (2,2,0), the spin-polarized surface configuration is (2,2,1). As described in the previous chapter, the charge transfer is associated with an $sp^3 \rightarrow sp^2 + p_z$ rehybridization, which transforms the respective step-edge atom from a trigonal-planar to a trigonal-pyramidal geometry.

The charge transfer mentioned above does not require a *global* R \rightarrow SC transition. Instead, *local* transitions are more likely, i.e., single step-edge atoms with empty DBs are doped with unpaired electrons from the Au chain. Here, (2,2,0₁) denotes the charge configuration of the locally doped R surface.

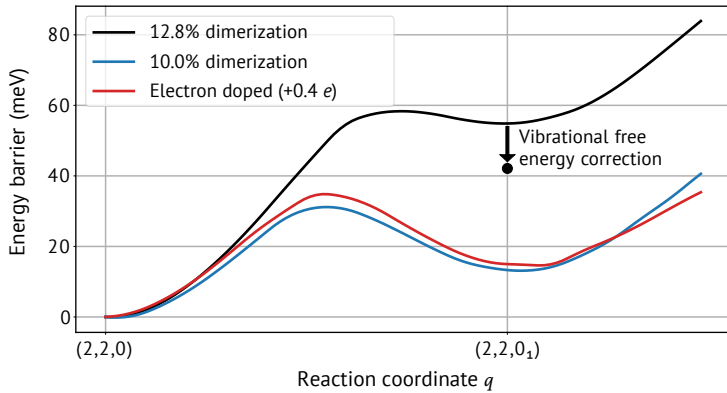


Figure 6.1: Calculated PES for the $(2,2,0)$ to $(2,2,0_1)$ transition for an Au dimerization of 12.8% (black) as calculated by AIMD simulations at 100 K. The PES for a reduced dimerization of 10% (blue) and a 0.4 electron-doped (1×6) supercell (red) is shown for comparison (see text in chapter 6.2.2). Additionally, the vibrational free-energy correction at 100 K at the local minimum of $(2,2,0_1)$ is marked. The image is adapted and taken from Ref. [198].

6.1.1 Potential Energy Surface

In order to investigate the probability of the $(2,2,0) \rightarrow (2,2,0_1)$ transition, the total energy along the reaction path is determined within a (1×6) supercell. All calculation parameters are identical to those on page 56. Due to the six step-edge atoms of the supercell, the $(2,2,0_1)$ configuration translates here to a concrete electron occupation of $(2,2,0,2,2,1)$. Locally doped step-edge atoms thus are separated by 15.8 Å. Comparative calculations with bigger supercells show that larger distances have only an insignificant influence on the total energy.

At temperatures such as 100 K, no significant changes of the Au dimer strength occur, as would be apparent, e.g., by changing intensities of the $\times 2$ reflexes in LEED. In contrast, only small changes related to the Debye-Waller effect are observed¹²⁴. Therefore, the Au chain dimerization (cf. Eq. 4.3) seems to be fixed at its average value of 12.8% at 100 K, as determined by AIMD calculations (see next section). The corresponding PES exhibits a global and a local minimum for the $(2,2,0)$ and $(2,2,0_1)$ charge configuration, as shown in Fig. 6.1. The energy difference between both states amounts to 55 meV, while the energy barrier separating the two states is 58 meV. However, the available thermal energy at 65 K is only 6 meV. Thus, an isolated $(2,2,0) \rightarrow (2,2,0_1)$ transition cannot explain the onset of the phase transition at this temperature.

6.1.2 Vibrational Free-Energy Correction

At finite temperature, entropy effects may alter the energy difference and barrier in favor of the local $(2,2,0_1)$ state. The free energy $F(V, T)$ accounts for the vibrational and electronic entropy, and its minimum determines the ground state at every temperature⁷³. Within the adiabatic approximation, F is given by¹⁹⁹

$$F(V, T) = F_{\text{el}}(V, T) + F_{\text{vib}}(V, T), \quad (6.1)$$

where $F_{\text{el}} = E_{\text{tot}} - TS_{\text{el}}$. Here, the internal energy E_{tot} is approximated by the zero-temperature DFT value. The electronic entropy contribution is given by

$$S_{\text{el}} = k_{\text{B}} \int dE n_{\text{F}} [f \ln f + (1-f) \ln(1-f)]. \quad (6.2)$$

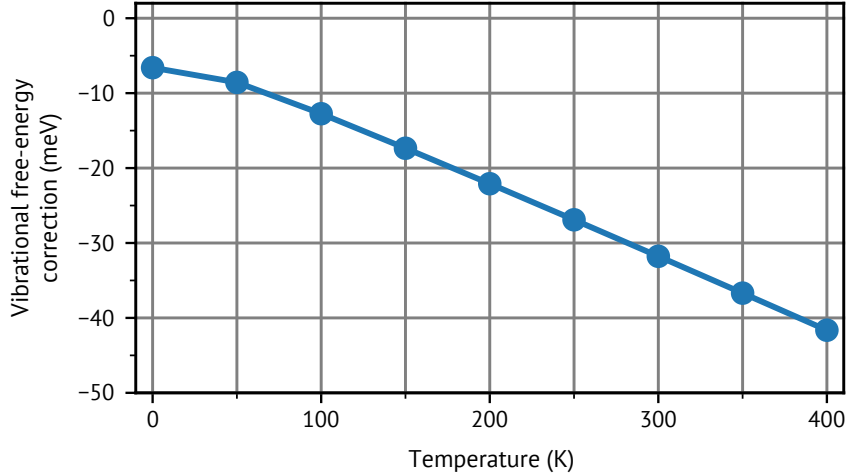


Figure 6.2: Vibrational free-energy correction of $(2,2,0_1)$ subtracted by the correction of $(2,2,0)$ for several temperatures. The negative energies indicate that $(2,2,0_1)$ gets more stable with rising temperature.

In this context, n_F and f denote the electronic density of states (DOS) and the Fermi distribution function, respectively. The vibrational contribution to the free energy F_{vib} simplifies within the harmonic approximation to

$$F_{\text{vib}} = \frac{\Omega}{8\pi^3} \int d^3k \sum_i \left[\frac{1}{2} \hbar\omega_i(\mathbf{k}) + k_B T \ln \left(1 - \exp \left(-\frac{\hbar\omega_i(\mathbf{k})}{k_B T} \right) \right) \right]. \quad (6.3)$$

Here, Ω is the supercell volume, and $\omega_i(\mathbf{k})$ are the phonon frequencies. These can be calculated within the frozen-phonon approximation by neglecting the volume and temperature dependence of the phonon frequencies and by assuming $F_{\text{el}}(V, T) \propto E_{\text{tot}}(T = 0)$. Due to the relatively large supercell, the phonon modes are calculated only at the Γ -point, i.e., only for $\mathbf{k} = 0$, which is assumed to represent the whole BZ well. Eq. 6.3 then further simplifies to

$$F_{\text{vib}} = \sum_i \left[\frac{1}{2} \hbar\omega_i(0) + k_B T \ln \left(1 - \exp \left(-\frac{\hbar\omega_i(0)}{k_B T} \right) \right) \right]. \quad (6.4)$$

In general, the vibrational contribution F_{vib} dominates the free-energy corrections. Phonons are well-defined only if restoring forces counteract small atomic displacements, i.e., the system is in a global or local minimum. Thus, the vibrational contribution is explicitly calculated only for the exact $(2,2,0)$ and $(2,2,0_1)$ configurations.

Fig. 6.2 illustrates the vibrational free-energy corrections of $(2,2,0_1)$ versus $(2,2,0)$ for different temperatures. Indeed, entropy effects further reduce the energy difference between $(2,2,0)$ and $(2,2,0_1)$ with increasing temperature. A black dot and arrow in Fig. 6.1 indicate the lowered energy difference. However, the difference is still far too large to explain the observed onset of the phase transition in a temperature range between 50 K and 100 K.

6.1.3 Band Modifications

A sudden increase in surface conductivity at 65 K caused by a self-doped step edge should be reflected in the band structure by shifting bands. Fig. 6.3 depicts several band structures calculated along the reaction

Reaction coordinate q	$S_{1/2}$		S_3		Total $(m^*/m_e)^{-1}$
	$(m_{\uparrow}^*/m_e)^{-1}$	$(m_{\downarrow}^*/m_e)^{-1}$	$(m_{\uparrow}^*/m_e)^{-1}$	$(m_{\downarrow}^*/m_e)^{-1}$	
0.0	-0.63	-0.63	-0.78	-0.78	-2.80
0.1	-0.63	-0.63	-0.80	-0.80	-2.85
0.2	-0.67	-0.67	-0.86	-0.86	-3.05
0.3	-0.77	-0.77	-1.05	-1.05	-3.59
0.4	-1.07	-1.07	-1.54	-1.54	-4.64
0.5	-0.35	-0.36	-2.18	-2.17	-5.09
0.55	n.a.	0.05	-8.29	-0.98	-8.22
0.6	0.88	0.19	-5.65	-0.68	-5.26
0.7	8.40	0.22	2.66	-0.64	10.03
0.8	3.39	0.22	2.59	-0.63	5.60
0.9	0.87	0.22	1.85	-0.47	2.46
1.0	1.45	0.19	1.60	-0.77	2.47

Table 6.1: The inverse effective masses of the $S_{1/2}$ and S_3 bands along the reaction path from (2,2,0) ($q = 0.0$) to (2,2,0₁) ($q = 1.0$). The masses were extracted from the band structure shown in Fig. 6.3 and normalized to the free electron mass m_e .

path from the (2,2,0) ground state ($q = 0.0$) to the (2,2,0₁) excited state ($q = 1.0$). The band structure is shown separately for both spin channels. Note again that the system is spin-polarized.

As discussed in section 5.1.2, the perfectly rehybridized surface has an unoccupied band about 0.3 eV above the Fermi energy. This band has a $\times 3$ periodicity and is assigned to the empty DBs of the two rehybridized step-edge atoms in the (1 \times 6) unit cell. As one rehybridized step-edge atom moves out of the planar sp^2 configuration, the band splits into two separate bands. The band associated with the transitioning step-edge atom thereby shifts to lower energies. Halfway along the reaction path, a spin splitting occurs: Starting at $q = 0.55$, the Si state is pushed below the Fermi energy in one of the two spin channels. In the other spin channel, the band moves back to higher energies and approaches the other Si state.

The shifting Si state also affects the Au bands, as seen in Fig. 6.3. Strong hybridizations of the Si and Au states lead to anticrossings. As a consequence, an increased DOS of the $S_{1/2}$ and S_3 bands at the Fermi energy is observed. At $q = 0.5$ an increase of 90% was calculated. The same applies to the (2,2,0₁) excited state, where the DOS is still 40% higher compared to the (2,2,0) ground state. The normalized DOS along the reaction path is illustrated in Fig. 6.4.

On the other hand, the hybridization also affects the Au bands' effective curvature at the Fermi energy and, therefore, the effective masses of the majority charge carriers. The inverse effective mass is given by

$$\frac{1}{m^*} = \frac{1}{S_F} \int_{FS} \frac{1}{\hbar^2} \frac{\partial^2 E(k)}{\partial k^2} dS_k, \quad (6.5)$$

where S_F is the Fermi surface (FS) area. Because of the quasi-1D character of the Au bands, the FS is also nearly 1D. Tab. 6.1 lists the inverse effective mass for each band and spin channel along the reaction path. The majority charge carriers change from holes to electrons along the reaction path. For configurations in between, the absolute total inverse mass increases significantly.

According to ballistic transport, the conductivity is proportional to both the inverse effective mass and the DOS at the Fermi energy. Thus, the changes of both quantities suggest that self-doping of the step edge by the Au reservoir can indeed explain the observed increase in conductivity.

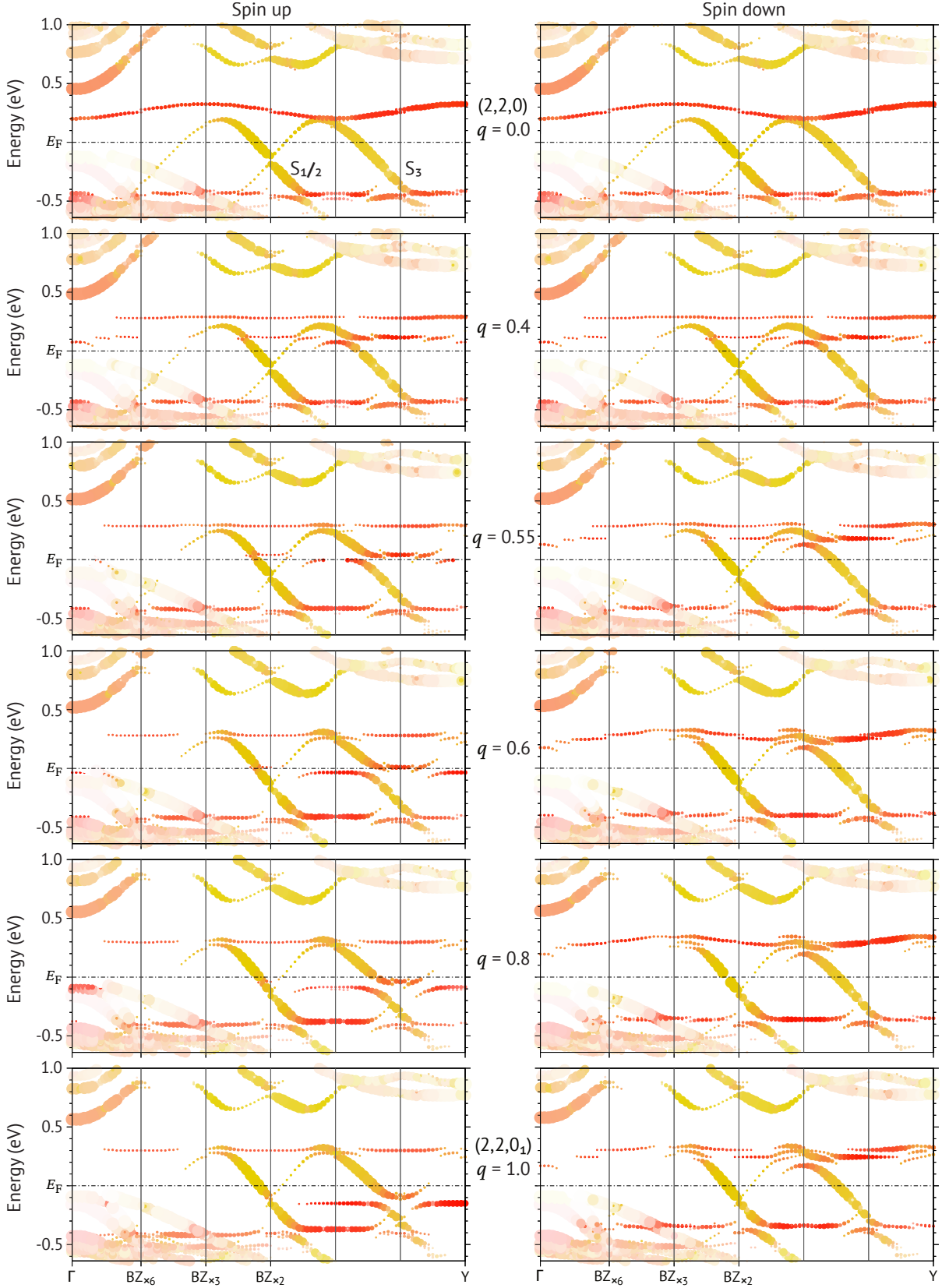


Figure 6.3: Surface bands in the direction parallel to the Au wires calculated along the reaction path from $(2,2,0)$ ($q = 0.0$) to $(2,2,0_1)$ ($q = 1.0$). The band structure is unfolded into the (1×1) BZ following the procedure described in Ref. [178]. The point size indicates the $\times 1$ character of each state, while the colors denote the localization at Si step-edge (red) and Au (yellow) atoms. The image is adapted and taken from Ref. [198].

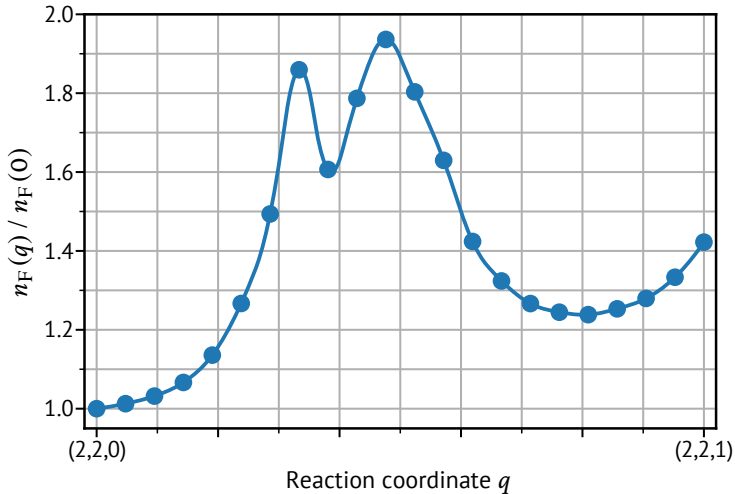


Figure 6.4: Relative change of the density of states n_F of the conductive $S_{1/2}$ and S_3 bands at the Fermi energy along the reaction path compared to the (2,2,0) ground state.

6.2 Ab Initio Molecular Dynamics Simulation

In the previous section, total-energy calculations showed that the thermal energy at 65 K would not suffice to drive an isolated $sp^2 + p_z \rightarrow sp^3$ transition efficiently. On the other hand, the band modifications associated with this transition can explain the increase in conductivity seen in 4PP transport measurements¹²⁴. Here, AIMD simulations are employed to investigate the phase transition in more detail. AIMD is a powerful computational method, implicitly accounting for numerous coordinated movements of various atoms.

6.2.1 Methodology

The AIMD calculations were performed within a (1×6) surface unit cell. A reduced k -point mesh of $2 \times 3 \times 1$ was used to sample the BZ, and the PBEsol functional was used to account for the XC effects. Temperatures of 50 K, 100 K, 150 K, 200 K, 300 K, and 400 K were simulated, where the system is coupled to a Nosé-Hoover thermostat⁵⁶. The R model was used as the initial configuration, although other models were tested as well.

The time step was chosen according to the highest and lowest vibrational mode: On the one hand, the time step must be small enough to model the fastest atomic movements correctly. On the other hand, the total simulation time should be a multiple of the lowest mode's period time. According to frozen-phonon calculations, the highest and lowest phonon mode within the R, SC, and K model have a period time of 63 fs and 5.9 ps. Therefore, a time step of 10 fs and a simulation time of at least 65 ps were chosen.

The first 3000 time steps were discarded (not counting to the total simulation time) to ensure thermal equilibrium. Additionally, the velocity distribution was compared with the Maxwell-Boltzmann distribution at the respective temperature (see appendix A.1).

6.2.2 Structural Analysis of the Step Edge and Au Chain

At first, the time-resolved charge occupation of the step-edge atoms was investigated in detail. For this purpose, the vertical positions of these atoms were evaluated and compared with the known R, SC, and K

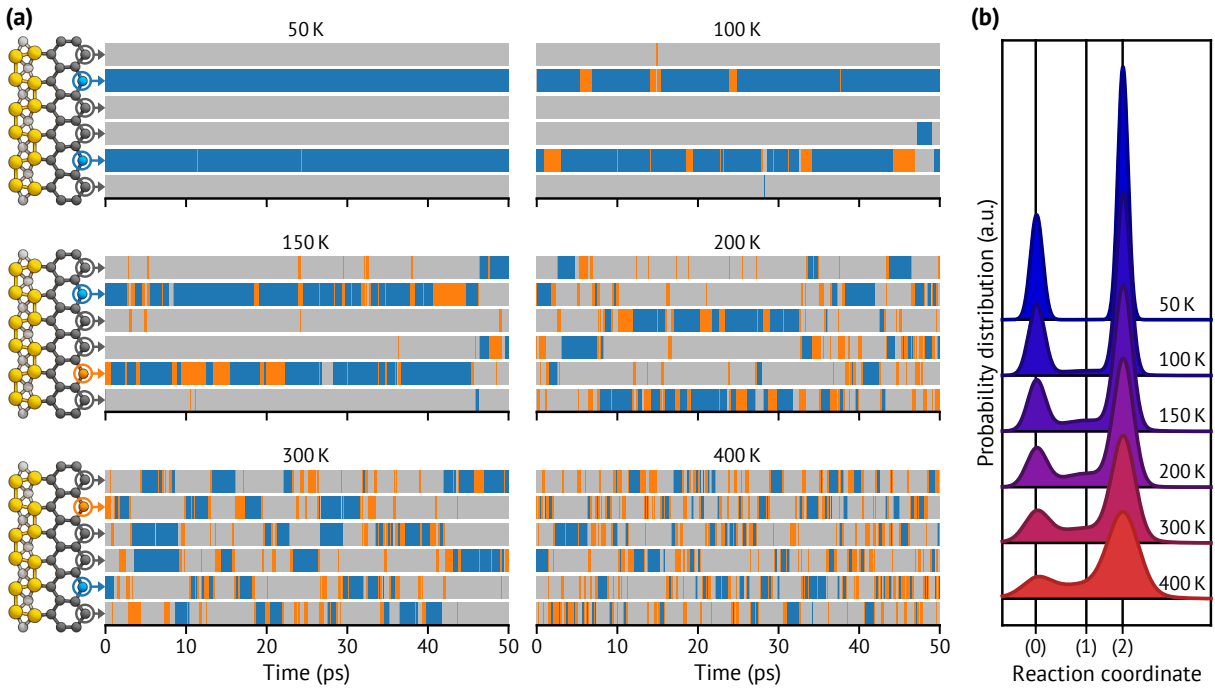


Figure 6.5: (a) Projection of the step-edge atoms' vertical positions on the corresponding charge occupation of the associated DBs, as calculated by AIMD. The colors indicate an empty (blue), singly occupied (orange), and doubly occupied (gray) DB. The atomic structures on the left illustrate the configuration at $t = 0$, respectively. (b) Distribution of the step-edge atoms' vertical positions. Equilibrium positions of Si atoms with empty (0), singly (1), and doubly (2) occupied DBs are indicated.

structures. With the aid of the projected magnetization density, the charge occupation of the step-edge atoms was derived for each time step. It is discriminated between empty (0), singly (1), and doubly (2) occupied DBs. A more detailed description of the procedure is given in appendix A.2.

In Fig. 6.5(a), the time evolution of the step-edge atoms' charge occupation is illustrated. The AIMD calculations performed here are very robust with respect to the initial structure: At 50 K, the system briefly relaxes to the R structure—*independent* of the initial atomic configuration. Only on two occasions, the step edge assumes short-lived (2,2,0₁) configurations. This is in agreement with the results of the previous chapter, *i.e.*, the R model with a charge configuration of (2,2,0) corresponds to the LT phase of Si(553)-Au.

At 100 K, the fluctuations appear more frequent and persist for longer times. Occasionally, also the step-edge atoms with doubly occupied DBs change their charge state. Despite the strong vertical vibrations of the step-edge atoms, the (2,2,0) configuration is still the most dominant structural motif at 100 K. However, the vertical vibrations amplify at higher temperatures, rendering the (2,2,0) configuration increasingly unlikely. At 300 K, the step-edge atoms are indistinguishable due to the increasing disorder.

This behavior is also reflected in the distribution of the vertical positions, shown in Fig. 6.5(b). At 50 K, the distribution is bimodal, *i.e.*, it exhibits two cluster points associated with the positions of step-edge atoms with filled and empty DBs. At 100 K, a third cluster point appears in between that corresponds to step-edge atoms with singly occupied DB. In the beginning, this cluster point is very weak but grows in magnitude with increasing temperature. It is related to the onset of the volatile (2,2,0₁) transition, as shown in Fig. 6.1. Furthermore, all three cluster points broaden with rising temperature, reflecting the increasing vertical vibrations of the step-edge atoms. A closer analysis of the cluster points and the total distribution function is given in appendix A.2.

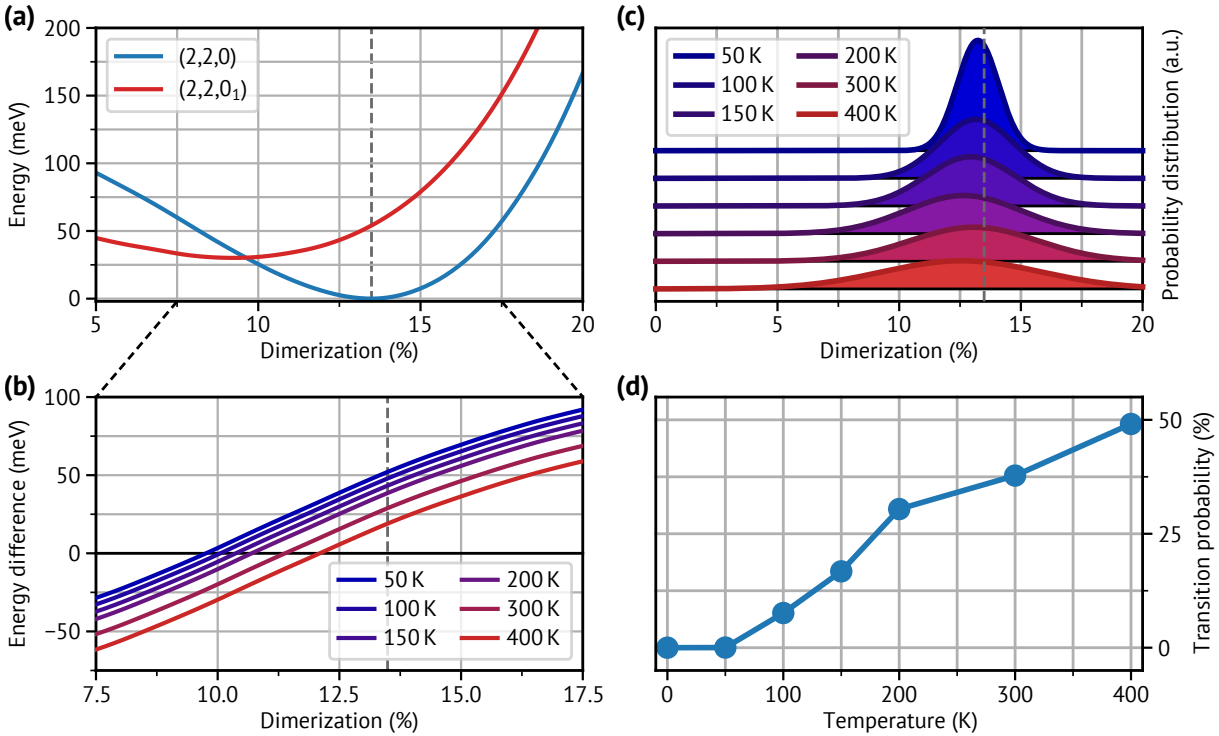


Figure 6.6: (a) PES for the $(2,2,0)$ (blue) and $(2,2,0_1)$ (red) configuration at 0 K with respect to the Au dimerization including zero-point energy corrections. (b) Energy difference of the $(2,2,0)$ versus the $(2,2,0_1)$ configuration considering the vibrational free-energy corrections at several temperatures. (c) Thermal distribution of the Au dimerization with respect to the AIMD temperature. The gray dashed line in (a)–(c) indicates the dimerization at which the surface obtains its global minimum at 0 K. (d) Transition probability to the $(2,2,0_1)$ excited state derived from the energy difference and dimerization distribution shown in (b) and (c). Parts of the image are adapted and taken from Ref. [198].

The AIMD simulations performed here clearly point towards a second-order phase transition that is of the order-disorder type. Its critical temperature lies between 50 K and 100 K. A description of the phase transition by solitons and antisolitons, i.e., nondissipative structural alterations moving back and forth the step edge, as proposed in [150], oversimplifies the actual surface dynamics.

Why is a phase transition observed in AIMD calculations at such low temperatures, while total-energy calculations indicate a much higher transition temperature? In order to answer this question, the Au chain is examined more thoroughly. In contrast to the SC model, the Au chain of the R model is considerably dimerized. This is due to the charge transfer from the step edge to the Au chain, causing a stronger binding of the Au dimers (cf. Refs. [142, 188] and section 5.1.2). In turn, a weakly dimerized Au chain has a lower electronegativity and thus favors the $\text{Au} \rightarrow \text{Si}$ charge transfer required for the $(2,2,0) \rightarrow (2,2,0_1)$ transition. The relation between dimerization and charge is demonstrated in Fig. 6.1: Lowering the dimerization from 12.8% (the average dimerization at 100 K) to 10% lowers the energy barrier in the same way as a heavily doped surface with 0.4 electrons per (1×6) surface unit cell.

The influence of the dimerization on the total energy of the $(2,2,0)$ and $(2,2,0_1)$ configuration is shown in Fig. 6.6(a). The $(2,2,0_1)$ configuration becomes more favorable for smaller dimerizations, while it becomes less favorable for larger ones. The impact of the vibrational free-energy corrections on the energy difference is shown in Fig. 6.6(b) for different temperatures. It is assumed here that the free-energy correction is not heavily influenced by the constrained change in dimerization.

In the AIMD simulations, a small reduction of the average dimerization with increasing temperature is observed, as shown in Fig. 6.6(c). This is mainly caused by the asymmetric shape of the potential (see Fig. 6.6(a)) and by the charge fluctuations between the step edge and Au chain. Although the average dimerization at 400 K is still above 12%, the dimerization distribution at 50 K already shows that dimerizations below 10% are occasionally reached. The dimerization distribution broadens as the temperature rises. As a consequence, the probability for even smaller dimerizations increases, and the energy barrier separating both charge configurations is reduced for brief periods of time. For more details regarding the time-resolved atomic displacements of the Au atoms, see Fig. A.4 and the accompanying text.

Under the assumption of thermodynamic equilibrium between (2,2,0) and (2,2,0₁) surface domains, the surface can be treated as a two-state system. The Boltzmann distribution then gives the transition probability to the excited state

$$p_{(2,2,0_1)}(T) = \int P(d) \frac{\exp\left(-\frac{E_{\text{dif}}(d)}{k_B T}\right)}{1 + \exp\left(-\frac{E_{\text{dif}}(d)}{k_B T}\right)} dd, \quad (6.6)$$

which is depicted in Fig. 6.6(d). It depends nonlinearly on the energy difference $E_{\text{dif}}(d)$ between the ground and excited state (see also Fig. 6.6(b)), which in turn depends on the dimerization d . As a result, the transition probability must be averaged by the normalized dimerization distribution $P(d)$, which is shown in Fig. 6.6(c). The increase for temperatures above 50 K is consistent with the AIMD results and explains why the phase transition occurs at such low temperatures. As suggested by Edler *et al.*, self-doping of the step edge can indeed explain the observed onset of the phase transition at 65 K. This self-doping is supported by dynamic modifications of the chemical potential of the Au chain, especially at LTs.

6.2.3 Transient Magnetic States

As the occurrence of the short-lived (2,2,0₁) state increases, both the charge and the number of unpaired electrons at the step edge increase, as well. Fig. 6.7(a) gives an overview of the average number of total and unpaired electrons per step-edge atom. As expected, the number of (unpaired) electrons increases with rising temperature, where the transitions also become more frequent.

In the past, an antiferromagnetic surface configuration was proposed for the Si(553)-Au surface^{13,120}. Here, adjacent spins could exhibit a magnetic order as well. This order would be short-lived as thermal fluctuations tend to destroy the spin states soon after. The time-averaged total magnitude of the magnetization $M_{\text{av}}(T) = \frac{1}{N} \sum_i^N |M(t_i, T)|$ obtained by AIMD is a useful parameter for investigating spin correlation. In Fig. 6.7(b), $M_{\text{av}}(T)$ is compared to the number of step-edge atoms with a singly occupied DB. Three scenarios assuming collinear spins are investigated here for these step-edge atoms: a random orientation of the spins, a ferromagnetic, and an antiferromagnetic spin configuration. For a single spin per (1 × 6) surface unit cell, these three configurations do not differ. For more spins, the ferromagnetic and antiferromagnetic configuration give an upper and lower limit on the total magnetization, while an uncorrelated configuration lies in between.

$M_{\text{av}}(T)$ matches very well with an antiferromagnetic spin alignment. Although the spin states are very short-lived, they still adapt to the spins in their nearer surrounding. However, this state must be distinguished from the SC model, in which the magnetic order is long-lived—at least at low temperatures—and has a fixed ×3 periodicity. It should further be noted that the supercell used here is relatively small.

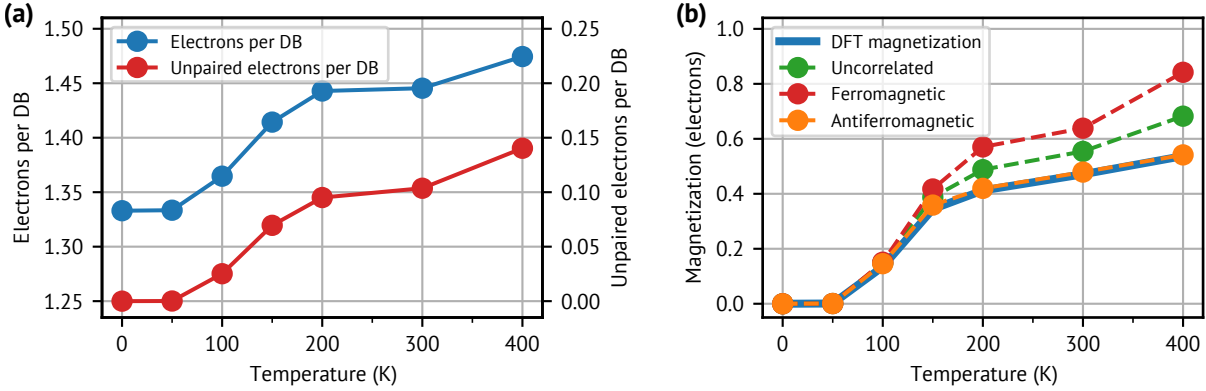


Figure 6.7: (a) Calculated average number of (unpaired) electrons per DB. (b) Total average magnetization as calculated by DFT (blue) compared to an uncorrelated (green), ferromagnetic (red), and antiferromagnetic (orange) scenario of the unpaired electrons that occur in the AIMD simulation (see text).

The finite size is also the reason for the finite magnetization in the case of an antiferromagnetic order. Nevertheless, these results are noteworthy, especially in the light of possible spin-stabilizing defects like Si vacancies, as discussed in Ref. [103] in the case of the Si(775)-Au surface.

6.3 Comparison with Experimental Results

The second-order phase transition appears in the experiment in different ways. Here, the results from the last section are compared with the results of two experiments: temperature-dependent Raman spectroscopy and SPA-LEED measurements.

6.3.1 Raman Spectroscopy

Raman spectroscopy is a common experimental method to study the vibrational modes of solids. It can thus be considered the experimental counterpart of phonon calculations. By subtracting a bulk reference spectrum, the Raman spectrum is restricted to surface modes, making it a versatile tool for surface analysis.

In the Raman spectra measured at different temperatures by J. Plaickner from the *Leibniz-Institut für Analytische Wissenschaften -ISAS-*, two modes of the Raman spectra shown in Fig. 6.8(a) exhibit a particularly high temperature dependence: The first is a high-frequency mode at 415 cm^{-1} , which is only visible above 100 K and grows in intensity with rising temperature. The second is a low-frequency mode at 41 cm^{-1} , which is redshifted for high temperatures. Both modes show gradual rather than abrupt changes. This is in good agreement with an order-disorder phase transition predicted by the AIMD simulations.

The frozen-phonon calculations discussed in section 6.1.2 help in identifying these two phonon modes. In the calculated phonon spectrum of the (2,2,0) ground state, the 41 cm^{-1} phonon mode is localized at the Au chain, as illustrated in Fig. 6.8(d). The atomic movement associated with this mode periodically alters the dimerization of the Au chain. Due to its low frequency, this mode becomes activated already at LT and thus supports the $(2,2,0) \rightarrow (2,2,0_1)$ transition by transient changes of the Au chain's electron affinity.

The softening of this phonon mode is analyzed by a projection of its eigenvector on the AIMD atomic velocities and subsequent Fourier transformation. A main peak analysis of the resulting frequency spectrum reveals a redshift of this phonon mode with rising temperature, in good agreement with the Raman

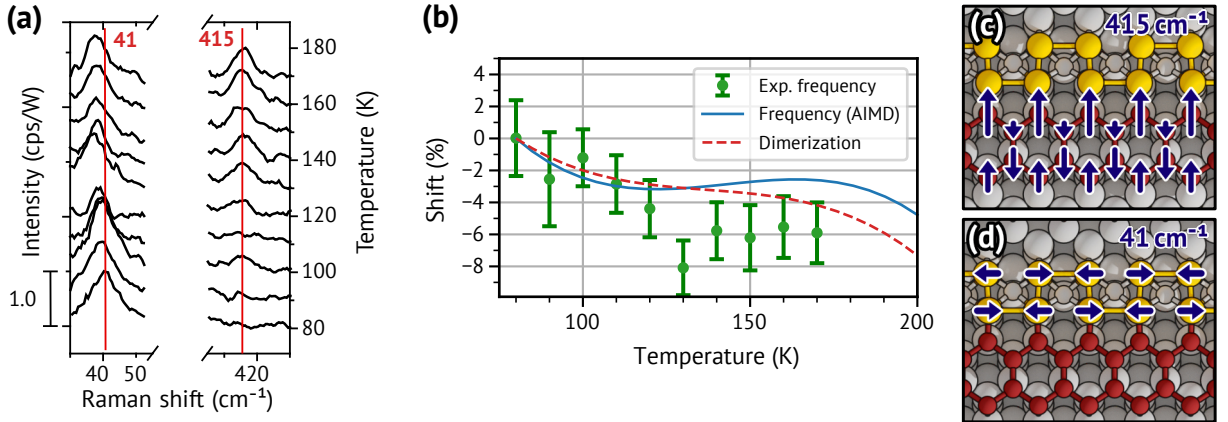


Figure 6.8: (a) Section of temperature-dependent Raman spectra highlighting two Raman modes at 415 cm^{-1} and 41 cm^{-1} located at the step edge and Au chain as illustrated in (c) and (d), respectively. The blue arrows indicate the atomic movement associated with the mode. (b) The measured redshift of the 41 cm^{-1} mode compared to the calculated redshift and relative change in dimerization. Parts of the image are adapted and taken from Ref. [198].

measurement, as depicted in Fig. 6.8(b). Similar to the frequency, the dimerization of the Au chain also decreases. Indeed, the softening of the phonon mode is tightly related to the reduction of the dimer strength, which in turn originates in the charge transfer to the step edge that drives the phase transition.

Fig. 6.8(c) depicts the high-frequency mode at 415 cm^{-1} , which is identified as a transversal shear mode along the HCC for both the (2,2,1) (SC model) and (2,2,2) (K model) surface configuration. In contrast, this mode is missing for the (2,2,0) ground state due to the strong disruption of the HCC by the $sp^2 + p_z$ -hybridized step-edge atoms. As the (2,2,0) configuration gets washed out by the step-edge fluctuations, this phonon mode can form. This explains why this mode is missing in the Raman spectra below 100 K.

6.3.2 SPA-LEED

The changes in the SPA-LEED pattern caused by the order-disorder phase transition were extensively discussed in chapter 3.3.3. Here, the temperature-dependent intensities of the $\times 3$ and $\times 2$ reflexes measured by two different groups (cf. Refs. [124, 151]) are examined more closely. The intensity changes in the experiment can be compared to the intensity changes obtained by the AIMD simulations.

The scattering intensity is proportional to the squared structure factor, i.e., $I \propto |F_{hkl}|^2$. The Miller indices hkl specify the associated reciprocal lattice vector \mathbf{G}_{hkl} of the respective reflex. For a supercell with N atoms, the structure factor is given by²⁵

$$F_{hkl} = \sum_i^N f_i(\mathbf{G}_{hkl}) \langle \exp(i\mathbf{G}_{hkl} \cdot \mathbf{r}_i(t)) \rangle, \quad (6.7)$$

where $\langle \dots \rangle$ indicates an averaging over time. The time-resolved positions $\mathbf{r}_i(t)$ of the atoms are directly derived from AIMD and implicitly incorporate changes related to the Debye-Waller effect¹⁴⁹. In addition, f_i denotes the atomic form factor of the i -th atom. The latter was calculated according to Ref. [200] for each element by

$$f_i(\mathbf{q}) = \sum_{j=1}^4 a_j \exp\left(-b_j \left(\frac{\mathbf{q}}{4\pi}\right)^2\right) + c, \quad (6.8)$$

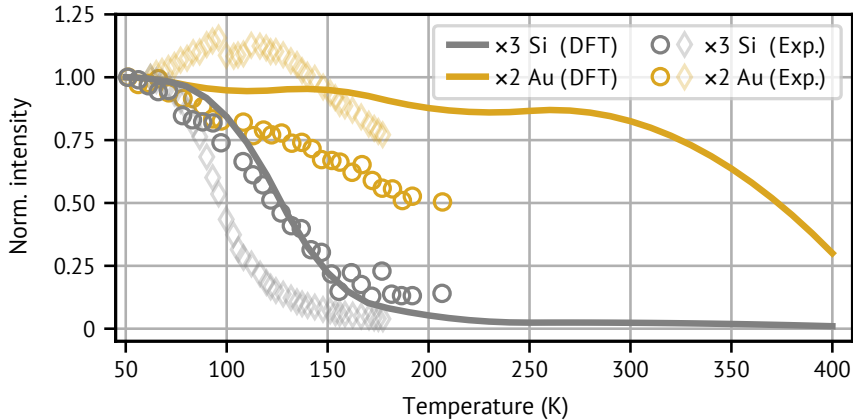


Figure 6.9: Experimental intensities of the $\times 3$ (gray) and $\times 2$ (gold) SPA-LEED patterns of Si(553)-Au grown on a low-doped¹²⁴ (circles) and a high-doped¹⁵¹ (diamonds) Si substrate compared to the calculated intensities from AIMD (lines, see text). The intensities are normalized to the value at 50 K. The image is adapted and taken from Ref. [198].

assuming an atomic form factor independent of the bonding geometry. The fitting coefficients a_j , b_j , and c for these functions are tabulated in Ref. [200].

Both experimental results show significant deviations from each other, as illustrated in Fig. 6.9. The differences are most likely due to the different substrate doping: While a lowly n-doped substrate ($> 1000 \Omega \text{ cm}$) was used in Ref. [124], a highly n-doped substrate ($\approx 0.01 \Omega \text{ cm}$) was utilized in Ref. [151].

In the case of the $\times 3$ reflex, both the measured and the simulated intensities start to fade below 100 K. The calculated quenching caused by the order-disorder transition excellently reproduces the data of the low-doped surface. In contrast, the high-doped surface exhibits a much faster drop in intensity. This scenario is supported by our DFT calculations: A low-doped substrate has a higher resemblance to the undoped Si substrate of the supercell. In contrast, it was previously shown that a high-doped surface exhibits a significantly lower transition barrier (see red line in Fig. 6.1). Therefore, the transition temperature is lowered, as is observed here.

Similarly, the $\times 2$ reflexes of the low-doped surface lose intensity with increasing temperature—but more slowly than the $\times 3$ reflexes. This attenuation is less pronounced for the simulated intensity of the $\times 2$ reflexes. However, this is to be expected since the limited size of the supercell affects the Au atoms more strongly. The Au atoms forming the chain are directly bonded and strongly correlated. While the AIMD calculations find a broadening of the dimerization distribution, they cannot correctly account for disorder arising from dimerization phase shifts¹⁹⁸, as discussed in appendix A.2 and shown in Fig. A.4.

Surprisingly, the intensity of the $\times 2$ reflexes of the highly doped surface initially increases up to 100 K, where it exhibits a small discontinuity. Only at higher temperatures, the intensity decreases rapidly and falls below its original level starting at 150 K. The reason for this behavior is unknown.

The order-disorder phase transition observed for the Si(553)-Au surface is associated with local charge transfers from the Au chain to the step edge accompanied by a rehybridization of the respective step-edge atoms. Thermally excited vibrations of the Au atoms periodically alter the electron affinity of the Au chain and thus facilitate the electron doping. This novel mechanism can also be expected to be relevant beyond the family of Au-stabilized Si surfaces¹⁹⁸. At higher temperatures, the order of the Au chain is also quenched.

Before I came here I was confused about this subject. Having listened to this lecture I am still confused. But on a higher level.

Enrico Fermi

7

Conclusion and Outlook

The present dissertation has addressed the electronic, structural, and thermodynamic properties of Si(553)-Au and, to some extent, Si(557)-Au. The family of Si(hhk)-Au surfaces exhibits several intriguing structural and electronic properties: For instance, the surface structure, the electronic bands, and the electronic transport of the Si(553)-Au surface are subject to thermal alterations. These seem to occur independently, as they exhibit individual transition temperatures and characteristics. Furthermore, intrinsic surface magnetism was proposed for the Si(553)-Au and Si(557)-Au surface. These properties have been investigated here to a large extent.

After a brief introduction in chapter 1, a theoretical description of 1D systems is presented in chapter 2. Furthermore, the Nosé-Hoover thermostat is explained, which is one of the essential building blocks for AIMD simulations. Chapter 3 then summarizes all results of Si(553)-Au and Si(557)-Au published so far.

Atomic structure models of Si(553)-Au and Si(557)-Au, in good agreement with the experiments at room temperature, were known at an early stage. Oxidation is the first modification to occur when the surfaces are introduced to the environment. Based on these structural models, the influence of molecular oxygen on the surface conductivity at room temperature was investigated in chapter 4. First, a potential energy surface (PES) was calculated for one and two O₂ molecules adsorbed on these surfaces. Based on these PESs, the most favored adsorption sites were determined. On both surfaces, dissociative adsorption of molecular oxygen occurs. However, the adsorption sites differ: While O mainly binds to the honeycomb chain (HCC) on Si(553)-Au, positions near the Si adatoms are preferred for Si(557)-Au. The different adsorption sites can explain why the $\times 2$ reflexes in LEED for Si(557)-Au decrease strongly with increasing oxygen dose, whereas hardly any changes in the diffraction pattern are detected for Si(553)-Au.

Afterward, the influence on the band structure was investigated. Similar to the LEED diffraction patterns, the band modifications of both surfaces differ significantly. For Si(557)-Au, the inverse effective mass of the conduction band associated with the conductivity along the Au chain decreases. Another adsorption site even interrupts a conduction channel. Although this adsorption site is not the most stable, it is still thermally occupied to some extent. This agrees with the measured decrease of conductivity along the chains with rising oxygen dose. For Si(553)-Au, this effect is much smaller and is in accordance with

the calculated band structure. Perpendicular to the chain direction, almost no influence on the surface conductivity is detected for both surfaces.

According to plasmon theory, the lower and upper limit of the electron-hole continuum and the plasmon loss spectrum have a fixed relationship for quasi-1D systems. Therefore, the band structure of the clean surface was utilized to determine the lower limit of the electron-hole continuum in section 4.2. By measuring the plasmon loss spectrum by Edler *et al.*, the upper limit was derived, and information about the electronic excitation spectrum was deduced. This new method was tested for the first time on the clean Si(557)-Au and Si(775)-Au and on the oxidized Si(557)-Au surface. It was found that the upper limit of the electron-hole continuum is in good agreement with the calculated empty bands. However, smaller band gaps are integrated over and, therefore, cannot be resolved.

At around 100 K, a phase transition occurs at the Si(553)-Au surface. Concerning the atomic structure, this is manifested by an additional $\times 3$ periodicity, as seen in STM and LEED. In the past, LT models with $\times 3$ periodic features were proposed. One of these models is characterized by a step edge at which every third Si atom is spin-polarized. This spin-chain model, however, has only limited compatibility with the experiment. Therefore, a new structural model for Si(553)-Au was developed and introduced in chapter 5. This model is characterized by a rehybridized step edge, resulting in diamagnetic $sp^2 + p_z$ -bonded instead of spin-polarized step-edge atoms. This diamagnetic atomic structure minimizes the total energy in LDA, PBEsol, and HSE calculations. In the case of the PBE method, however, the rehybridized model cannot be stabilized. This was attributed to a poor description of the Au lattice parameter by the PBE functional.

In addition, the consistency of the calculated band structure with ARPES measurements is improved. The biggest difference compared to the spin-polarized model is the absence of one of the occupied bands, which could not be observed in the experiment. Also, the simulated STM images of the rehybridized structure better match with the experimental STM images. Although both models reproduce the pattern above a tunneling voltage of +0.7 V equally well, only the rehybridized model displays the $\times 6$ periodic pattern at lower voltages. These can be attributed to a parity breaking caused by the interaction of the more strongly dimerized Au chain with the step edge. Overall, the rehybridized model is confirmed both by DFT total-energy calculations and by comparison with experimental data.

In chapter 6, the mechanism driving the phase transition on the Si(553)-Au surface was investigated. Thereby, a transition scenario involving a charge transfer from the Au chain to the step edge accompanied by a local $sp^2 + p_z \rightarrow sp^3$ rehybridization was examined. In this process, the empty DB of the corresponding step-edge atom is filled with an unpaired electron. On the one hand, band structure changes caused by this transition can well explain the rapid increase in conductivity at 65 K, as observed in a 4PP experiment. On the other hand, total-energy calculations show that the thermal energy at 65 K cannot sufficiently drive this transition. The inclusion of vibrational free-energy corrections lowers the energy barrier to some extent. Nevertheless, the energy barrier remains impassable at 65 K.

Therefore, AIMD simulations were used in the following to investigate the phase transition in more detail. Projections of the step-edge atoms' vertical positions on their charge configurations show indeed that charge fluctuations already occur for temperatures below 100 K. A low-frequency Au mode plays a vital role in this process: This mode is sufficiently occupied even at low temperatures and causes a periodic change in the Au dimerization. As a consequence, the electron affinity of the Au chain is lowered for short periods of time, in which the charge transfer to the step edge is facilitated. This explains the observed

self-doping of the DBs even at low temperatures and identifies the phase transition as an order-disorder type. The unpaired electrons of the short-lived states seem to prefer an antiferromagnetic arrangement.

The AIMD simulations also reproduce the attenuation of the $\times 3$ reflexes in SPA-LEED spectra with increasing temperature. The agreement with the $\times 2$ Au reflexes is not as good. However, this can be attributed to the high correlation of the Au atoms and the limited size of the supercell in chain direction. In addition, two modes with strong temperature dependence are visible in the Raman spectra of Si(553)-Au. The first mode shows a slight redshift with increasing temperature and can be identified with the Au dimerization mode. A similar redshift is also visible in AIMD, caused by a decreased dimer strength due to the charge transfer. The second mode is localized at the step edge and appears at temperatures above 100 K. Frozen-phonon calculations show that the rehybridized step-edge atoms of the low-temperature phase strongly disturb the step edge. As a consequence, this mode exists only at higher temperatures.

The order-disorder phase transition is thus explained by a self-doping of the step edge by the Au chain. A low-frequency vibrational Au mode facilitates the phase transition. It is in good agreement with the experimental findings and can reproduce the 4PP, Raman spectroscopy, and LEED measurements.

A still open question regarding the Si(553)-Au surface is the nature of its defects. Although the influence of oxygen and hydrogen has already been investigated in this dissertation and other papers^{142,192}, less is known about the intrinsic defects. In a study involving STM, Kang *et al.* suggested that the intrinsic defects are partially dissociated water molecules¹¹⁵. A verification of this model by DFT calculations is still awaited. As the defects are known to shift the quenching of the $\times 3$ structure in their immediate vicinity to higher temperatures¹¹³, further investigations are essential. Although it can be assumed that charge-doping by the adsorbates plays an important role, the exact mechanism remains unknown.

Also, the influence of other foreign adsorbates on the Si(553)-Au surface would be interesting with respect to nanoengineering and the stabilization of spin states, as already proposed in Ref. [103]. Up to now, the influence of In²⁰¹, C70²⁰², and several organic molecules^{203–205} were investigated. However, research focusing on stabilizing the spin states at the step edges is missing on a larger scale.

Finally, the temperature-dependent SPA-LEED measurement of Hafke in Refs. [150, 151] shows an increase of the $\times 2$ reflex intensity with increasing temperature within a small temperature range. In his dissertation, Hafke also describes a simultaneous decrease of the corresponding FWHM, which is highly unusual. In addition, both the intensity and the FWHM of the $\times 2$ reflexes show a small discontinuity. These results can be observed both when cooling and heating the surface and are reported to be reproducible. A closer investigation of this unusual behavior would therefore be desirable.

With regard to the systems investigated here, it becomes apparent that the challenges of miniaturization, i.e., shrinking electronic components towards the atomic limit, are not solely of technological character. Instead, details of the atomic structure and the resulting quantum mechanical 1D and 2D properties become prominent. In particular, these systems are highly sensitive to impurities such as oxygen, which significantly impact their electronic transport properties. In addition, wires in the atomic limit are in a complex interplay with their substrate: In the case of Si(557)-Au, this is manifested by the creation of silicon spin chains. For Si(553)-Au surfaces, short-lived surface states due to transient doping arise. As a result, phase transitions emerge, which fundamentally change the thermal properties of such wires, as well. These physical effects will therefore come increasingly into focus with advancing miniaturization.

A

Molecular Dynamics Simulations

A.1 Velocity Distribution

In *ab initio* molecular dynamics simulations, the Nosé-Hoover thermostat regulates the simulated temperature by coupling the system to a virtual heat bath. This heat bath conforms to a Maxwell-Boltzmann distribution. In general, the Maxwell-Boltzmann distribution well describes the velocity distribution of particles in the high-temperature range. Therefore, great care has to be taken when simulating temperatures as low as 50 K. In Fig. A.1, the velocity distributions obtained by the AIMD simulations are compared to the Maxwell-Boltzmann distribution. For all temperatures, the calculated velocities conform very closely to the theoretical distributions, which are plotted for the respective set temperature. In addition, a good agreement between the calculated and the theoretical distribution also indicates a converged system with respect to the initial unphysical velocity distribution.

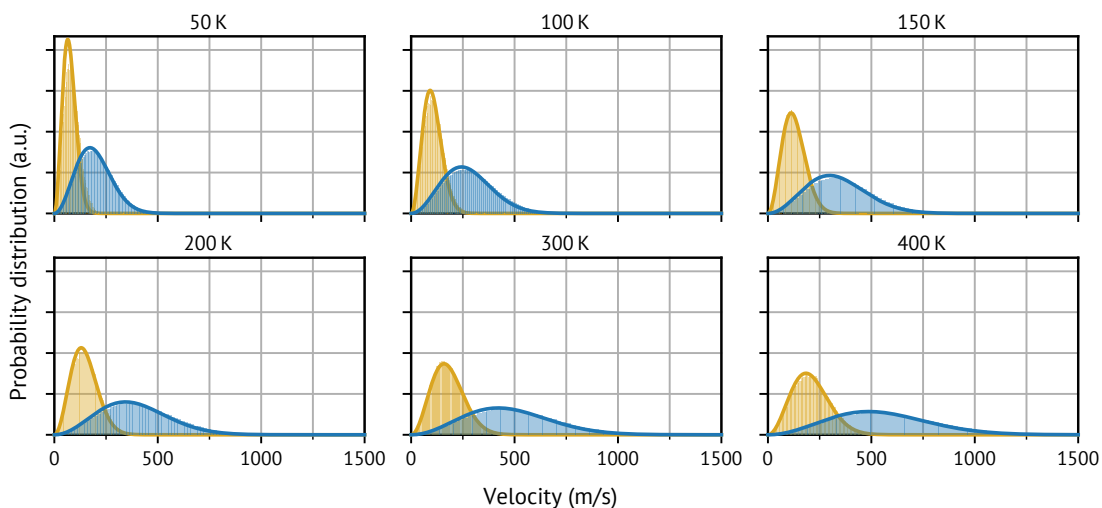


Figure A.1: The AIMD simulation's velocity distribution of the Si (blue patches) and Au (gold patches) atoms for several temperatures. The Maxwell-Boltzmann distribution of the respective temperature is given by blue and golden solid lines.

A.2 Structural Details

The distributions of the step-edge atoms' vertical positions exhibit three cluster points, as illustrated in Fig. A.2. These cluster points correspond to the different bonding geometries associated with an empty (0), singly (1), and doubly (2) occupied dangling bond. However, the distribution is bimodal at 50 K, as the spin-polarized state is accessible only at higher temperatures. As demonstrated in Fig. A.2, the total distribution is well described by three Gaussian distribution functions centered at the equilibrium positions of the step-edge atoms associated with the three charge states.

Fig. A.3 shows the corresponding time-resolved vertical position as well as the projected magnetization of each of the six step-edge atoms in a (1×6) surface unit cell. The latter is obtained by the projection of the magnetization density onto the atomic orbitals of the respective step-edge atom. A step-edge atom is considered to host an unpaired electron if its magnetic projection is at least half the value known from the SC model. Otherwise, it is assumed to host two or zero additional electrons, depending on whether the vertical position is above or below the equilibrium position of the singly occupied state. Fig. 6.5 displays the associated projection onto the charge states with respect to time and temperature.

In Fig. A.4, the deviations of the Au chain to a perfect equidistant chain is illustrated. For all six Au atoms of each of the two Au strands, the relative displacement with respect to the underlying Si bulk lattice parameter is shown in chain direction. The total relative displacement of an Au dimer pair corresponds to their dimerization, according to Eq. 4.3. With rising temperature, the amplitude of the Au oscillations increase. At two points—one time at 300 K and one time at 400 K, see Fig. A.4—there is a phase shift of 180° at the Au chain. This phase shift is characterized by a move of the dimer arrangement by one bulk lattice site a_0 along the Au chain. Due to the strong correlation of the Au atoms paired with a relatively small supercell along the chain direction, such phase shifts are considered to be suppressed in the simulation. In reality, these phase shifts are expected to occur more frequently and also at lower temperatures.

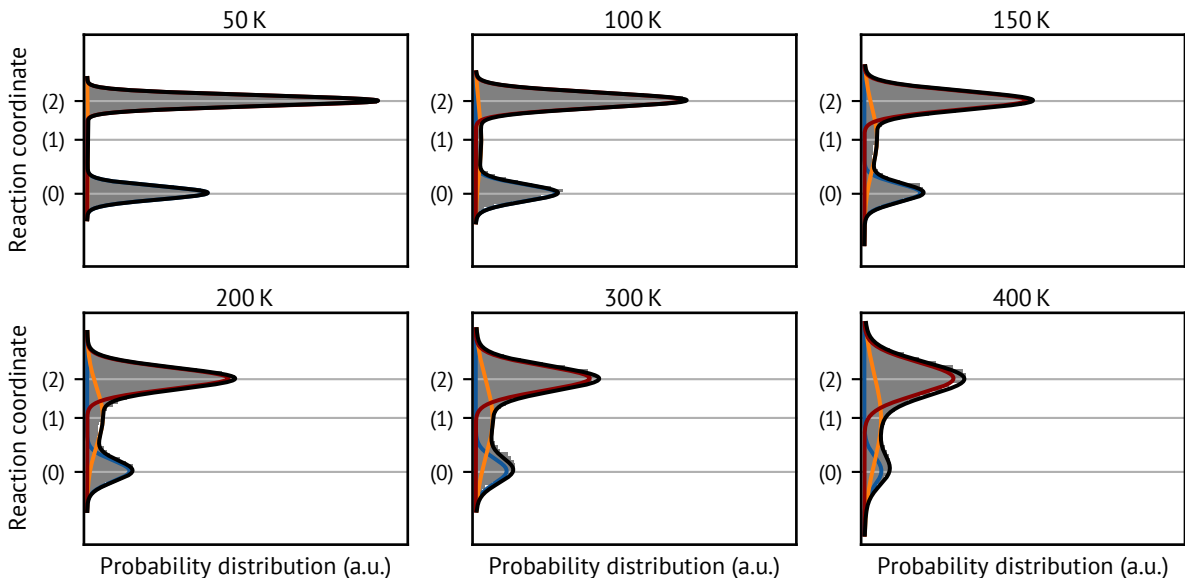


Figure A.2: Distribution of the step-edge atoms' vertical positions (gray bars) calculated by AIMD for several temperatures. The equilibrium positions of step-edge atoms with empty (0), singly (1), and doubly (2) occupied DBs are indicated. The distribution is well fitted by a function (black line) consisting of three Gaussians centered at the respective equilibrium positions.

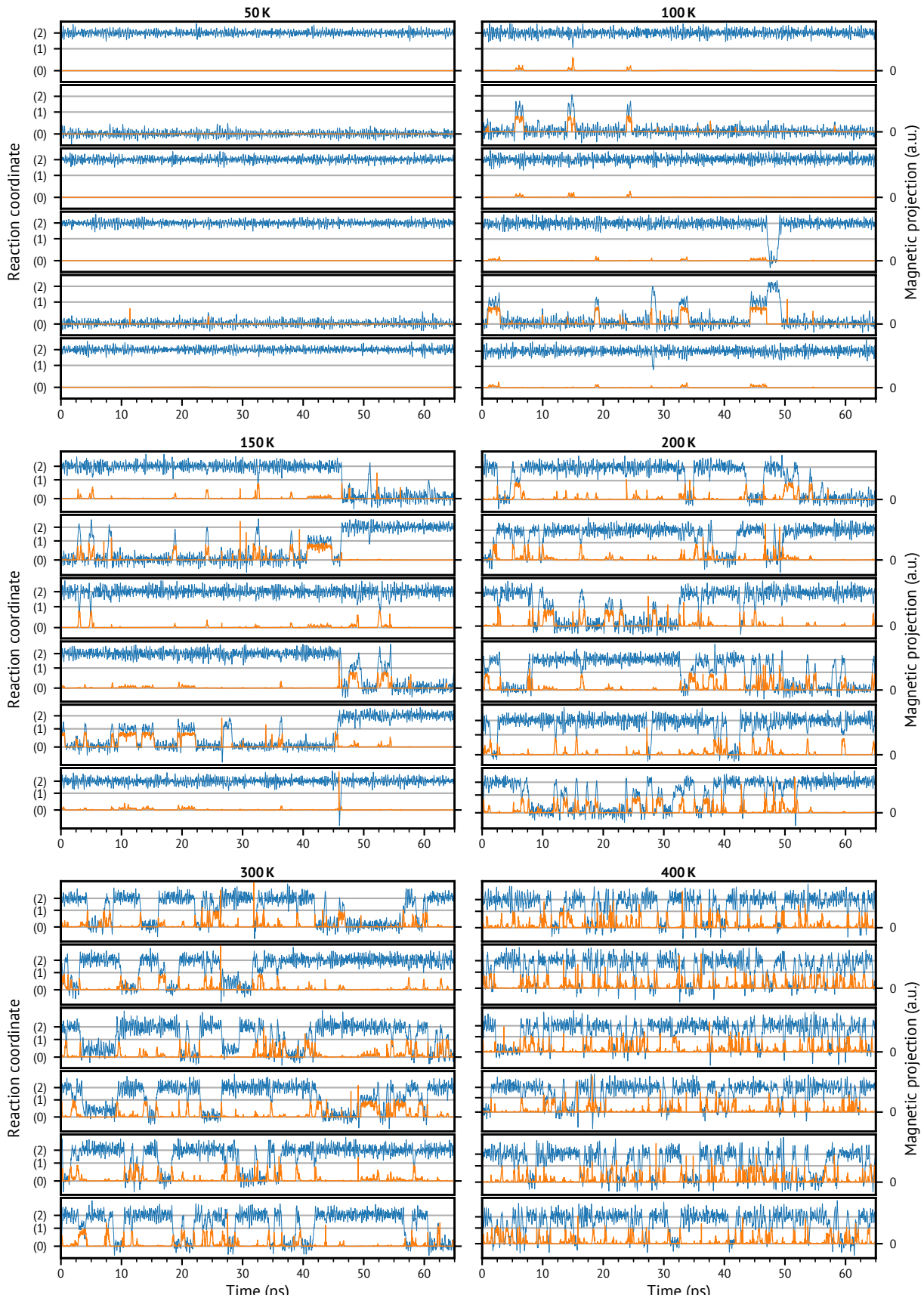


Figure A.3: Position along the $sp^3 \rightarrow sp^2 + p_z$ reaction coordinate (associated with the charge filling (0), (1) and (2), blue) and magnetization (orange) of each of the six step-edge atoms for several temperatures from 50 K to 400 K.

A Molecular Dynamics Simulations

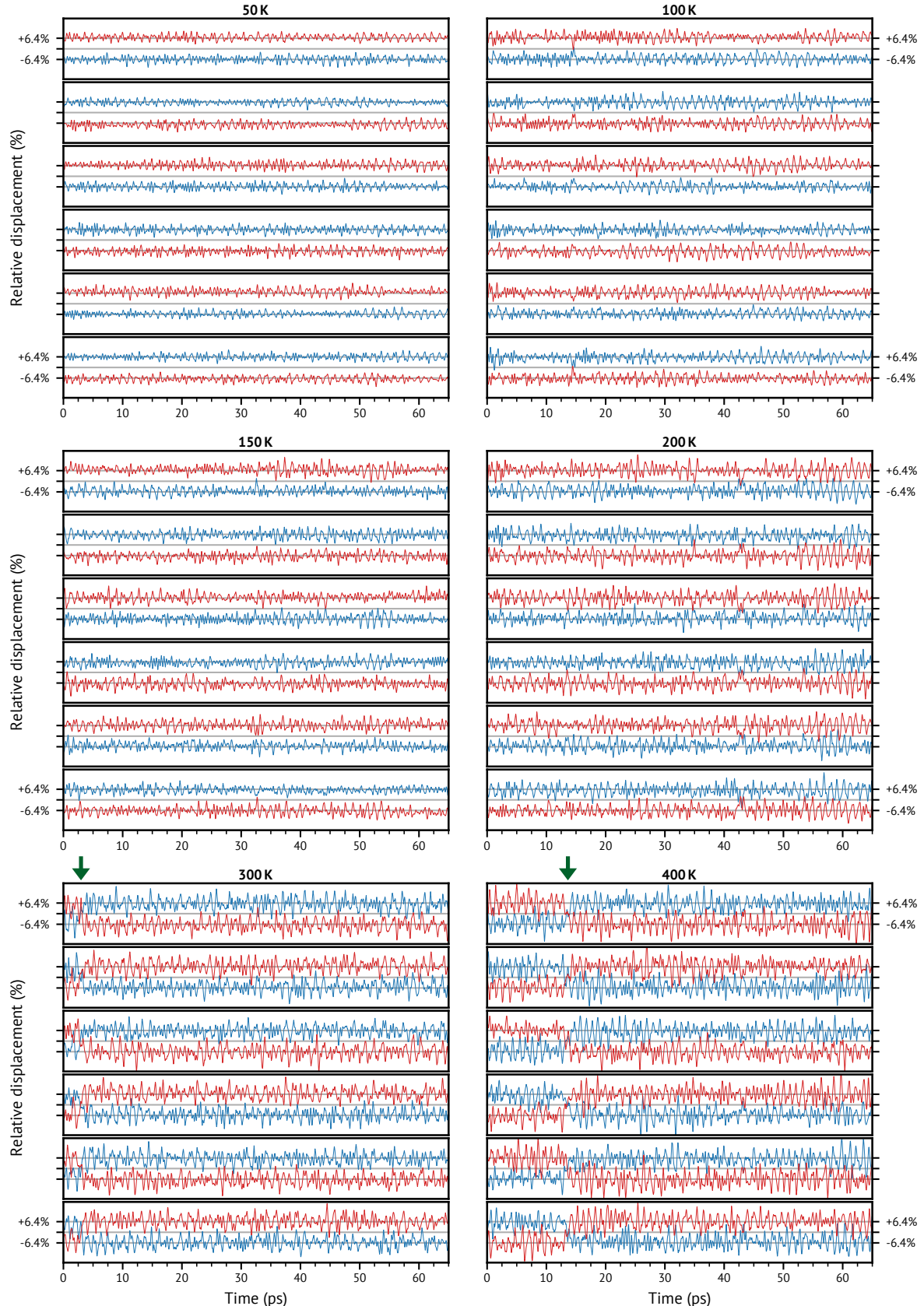


Figure A.4: Relative displacement of the six Au atoms per left (blue) and right (red) Au strand in the (1×6) surface unit cell with respect to the underlying Si bulk lattice constant a_0 for several temperatures. A displacement of 0% corresponds to an equidistant Au chain with no dimerization. Green arrows indicate oscillations that lead to a phase shift of 180° within the Au chain.

Bibliography

1. E. Abbott. *Flatland: A Romance of Many Dimensions* (1885). (Cit. on p. 1).
2. A. Einstein. Die Grundlage der allgemeinen Relativitätstheorie. *Ann. Phys.* **354**, 769–822 (1916). doi: 10.1002/andp.19163540702 (cit. on p. 1).
3. M. v. Laue. Kritische Bemerkungen zu den Deutungen der Photogramme von Friedrich und Knipping. *Physikalische Zeitschrift* **10**, 555–600 (1913) (cit. on p. 1).
4. C. B. Duke. The birth and evolution of surface science: Child of the union of science and technology. *Proceedings of the National Academy of Sciences* **100**, 3858–3864 (2003). doi: 10.1073/pnas.0730358100 (cit. on p. 1).
5. D. P. DiVincenzo & E. J. Mele. Self-consistent effective-mass theory for intralayer screening in graphite intercalation compounds. *Phys. Rev. B* **29**, 1685–1694 (1984). doi: 10.1103/physrevb.29.1685 (cit. on p. 1).
6. K. S. Novoselov, A. K. Geim, S. V. Morozov, D. Jiang, *et al.* Electric Field Effect in Atomically Thin Carbon Films. *Science* **306**, 666–669 (2004). doi: 10.1126/science.1102896 (cit. on p. 1).
7. S. Tomonaga. Remarks on Bloch's Method of Sound Waves applied to Many-Fermion Problems. *Prog. Theor. Phys.* **5**, 544–569 (1950). doi: 10.1143/ptp/5.4.544 (cit. on pp. 1, 7, 17, 35).
8. J. M. Luttinger. An Exactly Soluble Model of a Many-Fermion System. *J. Math. Phys.* **4**, 1154–1162 (1963). doi: 10.1063/1.1704046 (cit. on pp. 1, 7, 17, 35).
9. R. E. Peierls. *Quantum Theory of Solids* (London, 1955). doi: 10.1093/acprof:oso/9780198507819.001.0001. (Cit. on pp. 1, 8, 17).
10. J. N. Crain, J. L. McChesney, F. Zheng, M. C. Gallagher, *et al.* Chains of gold atoms with tailored electronic states. *Phys. Rev. B* **69**, 125401 (2004). doi: 10.1103/PhysRevB.69.125401 (cit. on pp. 2, 18–23, 25, 26, 28, 29, 32–34, 38, 52, 53, 55, 56, 60, 62).
11. P. Segovia, D. Purde, M. Hengsberger & Y. Baer. Observation of spin and charge collective modes in one-dimensional metallic chains. *Nature* **402**, 504–507 (1999). doi: 10.1038/990052 (cit. on pp. 2, 19, 21, 32–34).
12. R. Losio, K. N. Altmann, A. Kirakosian, J.-L. Lin, *et al.* Band Splitting for Si(557)-Au: Is It Spin-Charge Separation? *Phys. Rev. Lett.* **86**, 4632–4635 (2001). doi: 10.1103/PhysRevLett.86.4632 (cit. on pp. 2, 32–34).
13. S. C. Erwin & F. J. Himpsel. Intrinsic magnetism at silicon surfaces. *Nat. Commun.* **1**, 58 (2010). doi: 10.1038/ncomms1056 (cit. on pp. 2, 23, 24, 28, 30, 32, 34, 55, 58, 62, 71).
14. D. Serrate, P. Ferriani, Y. Yoshida, S.-W. Hla, *et al.* Imaging and manipulating the spin direction of individual atoms. *Nat. Nanotechnol.* **5**, 350–353 (2010). doi: 10.1038/nnano.2010.64 (cit. on p. 2).
15. G. D. Mahan. Spin Shift Register from a One-Dimensional Atomic Chain. *Phys. Rev. Lett.* **102**, 016801 (2009). doi: 10.1103/PhysRevLett.102.016801 (cit. on p. 2).
16. H. Okino, I. Matsuda, S. Yamazaki, R. Hobara & S. Hasegawa. Transport in defective quasi-one-dimensional arrays of chains of gold atoms on a vicinal silicon surface. *Phys. Rev. B* **76**, 035424 (2007). doi: 10.1103/PhysRevB.76.035424 (cit. on pp. 2, 22, 27, 28, 30, 34, 35, 38, 63).
17. I. Cutrass. 'Better Yield on 5nm than 7nm': TSMC Update on Defect Rates for N5. <https://www.anandtech.com/show/16028/better-yield-on-5nm-than-7nm-tsmc-update-on-defect-rates-for-n5>. Accessed: 2021-01-15 (cit. on p. 2).
18. T. Lichtenstein, J. Aulbach, J. Schäfer, R. Claessen, *et al.* Two-dimensional crossover and strong coupling of plasmon excitations in arrays of one-dimensional atomic wires. *Phys. Rev. B* **93**, 161408(R) (2016). doi: 10.1103/PhysRevB.93.161408 (cit. on pp. 2, 26, 28, 30, 33).
19. L. D. Landau. The Theory of a Fermi Liquid. *Sov. Phys. JETP* **3**, 920 (1956) (cit. on p. 3).
20. L. D. Landau. Oscillations in a Fermi Liquid. *Sov. Phys. JETP* **5**, 101 (1957) (cit. on p. 3).

21. L. D. Landau. On the conservation laws for weak interactions. *Nucl. Phys.* **3**, 127–131 (1957). doi: 10.1016/0029-5582 (57)90061-5 (cit. on pp. 3, 5).
22. L. D. Landau. On the Theory of the Fermi Liquid. *Sov. Phys. JETP* **8**, 70 (1958) (cit. on p. 3).
23. T. Giamarchi. *Quantum Physics in One Dimension* (Clarendon, Oxford, 2007). doi: 10.1093/acprof:oso/9780198525004.001.0001. (Cit. on pp. 3–7).
24. J. Voit. One-dimensional Fermi liquids. *Rep. Prog. Phys.* **58**, 977–1116 (1995). doi: 10.1088/0034-4885/58/9/002 (cit. on pp. 3, 5).
25. N. Ashcroft & N. Mermin. *Solid State Physics* (Saunders College Publishing, Fort Worth, 1976). doi: 10.1002/piuz.19780090109. (Cit. on pp. 3, 26, 73).
26. R. M. Martin, L. Reining & D. M. Ceperley. *Interacting Electrons: Theory and Computational Approaches* (Cambridge University Press, Cambridge, 2016). doi: 10.1017/CBO9781139050807. (Cit. on pp. 4, 5).
27. J. Lindhard. On the Properties of a Gas of Charged Particles (Kgl. Danske Videnskab. Selskab, København, 1954). (Cit. on p. 6).
28. J. Voit. A brief introduction to Luttinger liquids. *AIP Conf. Proc.* **544**, 309–318 (2000). doi: 10.1063/1.1342524 (cit. on p. 7).
29. S. Hasegawa. Quasi-one-dimensional metals on semiconductor surfaces with defects. *J. Phys. Condens. Matter* **22**, 084026 (2010). doi: 10.1088/0953-8984/22/8/084026 (cit. on pp. 7, 21).
30. D. Sénéchal. An Introduction to Bosonization. in *Theoretical Methods for Strongly Correlated Electrons* (Springer, New York, 2004), pp. 139–186. doi: 10.1007/0-387-21717-7_4 (cit. on p. 7).
31. J.-P. Pouget. The Peierls instability and charge density wave in one-dimensional electronic conductors. *Comptes Rendus Physique* **17**, 332–356 (2016). doi: 10.1016/j.crhy.2015.11.008 (cit. on p. 8).
32. A. W. Overhauser. Exchange and Correlation Instabilities of Simple Metals. *Phys. Rev.* **167**, 691–698 (1968). doi: 10.1103/PhysRev.167.691 (cit. on p. 8).
33. J. Friedel. Phase Changes and Electron Phonon Couplings in Perfect Crystals. Modulated Structures. An Introduction. in *Electron-Phonon Interactions and Phase Transitions* (ed T. Riste) (Springer, Boston, MA, 1977), pp. 1–49. doi: 10.1007/978-1-4615-8921-1 (cit. on p. 8).
34. Low-Dimensional Electronic Properties of Molybdenum Bronzes and Oxides (ed C. Schlenker) (Springer, Dordrecht, 1989). doi: 10.1007/978-94-009-0447-7. (Cit. on p. 8).
35. Low-Dimensional Conductors and Superconductors (eds D. Jérôme & L. G. Caron) (Springer, Boston, MA, 1987). doi: 10.1007/978-1-4899-3611-0. (Cit. on p. 8).
36. P. C. Snijders & H. H. Weitering. Colloquium: Electronic instabilities in self-assembled atom wires. *Rev. Mod. Phys.* **82**, 307–329 (2010). doi: 10.1103/RevModPhys.82.307 (cit. on pp. 8, 21, 30, 34).
37. S. Murakami, N. Nagaosa & S.-C. Zhang. Spin-Hall Insulator. *Phys. Rev. Lett.* **93**, 156804 (2004). doi: 10.1103/PhysRevLett.93.156804 (cit. on p. 8).
38. C. L. Kane & E. J. Mele. Z_2 Topological Order and the Quantum Spin Hall Effect. *Phys. Rev. Lett.* **95**, 146802 (2005). doi: 10.1103/PhysRevLett.95.146802 (cit. on p. 8).
39. B. A. Bernevig & S.-C. Zhang. Quantum Spin Hall Effect. *Phys. Rev. Lett.* **96**, 106802 (2006). doi: 10.1103/PhysRevLett.96.106802 (cit. on p. 8).
40. M. König, S. Wiedmann, C. Brüne, A. Roth, *et al.* Quantum Spin Hall Insulator State in HgTe Quantum Wells. *Science* **318**, 766–770 (2007). doi: 10.1126/science.1148047 (cit. on p. 8).
41. L. Dudy, J. Aulbach, T. Wagner, J. Schafer & R. Claessen. One-dimensional quantum matter: Gold-induced nanowires on semiconductor surfaces. *J. Phys. Condens. Matter* **29**, 433001 (2017). doi: 10.1088/1361-648X/aa852a (cit. on pp. 8, 21).
42. P. C. Hohenberg. Existence of Long-Range Order in One and Two Dimensions. *Phys. Rev.* **158**, 383–386 (1967). doi: 10.1103/PhysRev.158.383 (cit. on p. 9).
43. N. D. Mermin & H. Wagner. Absence of Ferromagnetism or Antiferromagnetism in One- or Two-Dimensional Isotropic Heisenberg Models. *Phys. Rev. Lett.* **17**, 1133–1136 (1966). doi: 10.1103/PhysRevLett.17.1133 (cit. on pp. 9, 11).

44. W. Nolting & A. Ramakanth. Quantum Theory of Magnetism (Springer, Berlin, Heidelberg, 2009). doi: 10.1007/978-3-540-85416-6. (Cit. on p. 9).
45. N. N. Bogoliubov. Quasimittelwerte in Problemen der statistischen Mechanik. *Physik. Abhandl. Sowjetunion* **6**, 113 (1962) (cit. on p. 9).
46. D. J. Thouless. Long-Range Order in One-Dimensional Ising Systems. *Phys. Rev.* **187**, 732–733 (1969). doi: 10.1103/PhysRev.187.732 (cit. on p. 13).
47. D. K. Ghosh. Nonexistence of Magnetic Ordering in the One- and Two-Dimensional Hubbard Model. *Phys. Rev. Lett.* **27**, 1584–1587 (1971). doi: 10.1103/PhysRevLett.27.1584 (cit. on p. 13).
48. P. Hohenberg & W. Kohn. Inhomogeneous Electron Gas. *Phys. Rev.* **136**, B864 (1964). doi: 10.1103/PhysRev.136.B864 (cit. on p. 14).
49. W. Kohn & J. Sham. Self-Consistent Equations Including Exchange and Correlation Effects. *Phys. Rev.* **140**, A1133 (1965). doi: 10.1103/PhysRev.140.A1133 (cit. on p. 14).
50. W. Kohn. Nobel Lecture: Electronic structure of matter—wave functions and density functionals. *Reviews of Modern Physics* **71**, 1253–1266 (1999). doi: 10.1103/revmodphys.71.1253 (cit. on p. 14).
51. W. Nolting. Theoretical Physics 8 - Statistical Physics (Springer, Cham, 2018). doi: 10.1007/978-3-319-73827-7. (Cit. on pp. 14, 16).
52. L. Woodcock. Isothermal molecular dynamics calculations for liquid salts. *Chem. Phys. Lett.* **10**, 257–261 (1971). doi: [https://doi.org/10.1016/0009-2614\(71\)80281-6](https://doi.org/10.1016/0009-2614(71)80281-6) (cit. on p. 14).
53. H. C. Andersen. Molecular dynamics simulations at constant pressure and/or temperature. *J. Chem. Phys.* **72**, 2384–2393 (1980). doi: 10.1063/1.439486 (cit. on p. 14).
54. S. Nosé. A molecular dynamics method for simulations in the canonical ensemble. *Mol. Phys.* **52**, 255–268 (1984). doi: 10.1080/00268978400101201 (cit. on pp. 14, 16).
55. S. Nosé. A unified formulation of the constant temperature molecular dynamics methods. *J. Chem. Phys.* **81**, 511–519 (1984). doi: 10.1063/1.447334 (cit. on p. 14).
56. W. G. Hoover. Canonical dynamics: Equilibrium phase-space distributions. *Phys. Rev. A* **31**, 1695–1697 (1985). doi: 10.1103/PhysRevA.31.1695 (cit. on pp. 16, 68).
57. M. Born & R. Oppenheimer. Zur Quantentheorie der Moleküle. *Ann. Phys.* **389**, 457–484 (1927). doi: 10.1002/andp.19273892002 (cit. on p. 16).
58. J. Liouville. Sur la Théorie de la Variation des constantes arbitraires. *Journ. de Math.* **3**, 342–349 (1838) (cit. on p. 16).
59. G. J. Martyna, M. L. Klein & M. Tuckerman. Nosé–Hoover chains: The canonical ensemble via continuous dynamics. *J. Chem. Phys.* **97**, 2635–2643 (1992). doi: 10.1063/1.463940 (cit. on p. 16).
60. M. Levinshtein, S. Rumyantsev & M. Shur. Semiconductor Parameters Vol. 1, pp. 1–2 (World Scientific, River Edge, NJ, 1996). doi: 10.1142/2046-vol1. (Cit. on p. 17).
61. F. Lutgens, E. Tarbuck & D. Tasa. Essentials of Geology (Prentice Hall, Upper Saddle River, NJ, 2017). (Cit. on p. 17).
62. R. E. Schlier & H. E. Farnsworth. Structure and Adsorption Characteristics of Clean Surfaces of Germanium and Silicon. *J. Chem. Phys.* **30**, 917–926 (1959). doi: 10.1063/1.1730126 (cit. on p. 17).
63. P. Krüger & J. Pollmann. Dimer Reconstruction of Diamond, Si, and Ge (001) Surfaces. *Phys. Rev. Lett.* **74**, 1155–1158 (1995). doi: 10.1103/PhysRevLett.74.1155 (cit. on pp. 18, 55).
64. M. Rohrmüller, W. G. Schmidt & U. Gerstmann. Electron paramagnetic resonance calculations for hydrogenated Si surfaces. *Phys. Rev. B* **95**, 125310 (2017). doi: 10.1103/PhysRevB.95.125310 (cit. on p. 18).
65. K. Yoo & H. H. Weitering. Electrical conductance of reconstructed silicon surfaces. *Phys. Rev. B* **65**, 115424 (2002). doi: 10.1103/PhysRevB.65.115424 (cit. on p. 18).
66. K. Takayanagi, Y. Tanishiro, M. Takahashi & S. Takahashi. Structural analysis of Si(111)-7×7 by UHV-transmission electron diffraction and microscopy. *J. Vac. Sci. Technol.* **3**, 1502–1506 (1985). doi: 10.1116/1.573160 (cit. on pp. 18, 24).

BIBLIOGRAPHY

67. M. Smeu, H. Guo, W. Ji & R. A. Wolkow. Electronic properties of Si(111)-7 \times 7 and related reconstructions: Density functional theory calculations. *Phys. Rev. B* **85**, 195315 (2012). doi: 10.1103/PhysRevB.85.195315 (cit. on p. 18).

68. C. Blumenstein, J. Schäfer, S. Mietke, S. Meyer, *et al.* Atomically controlled quantum chains hosting a Tomonaga–Luttinger liquid. *Nat. Phys.* **7**, 776–780 (2011). doi: 10.1038/nphys2051 (cit. on p. 18).

69. K. Nakatsuji & F. Komori. Debate over dispersion direction in a Tomonaga–Luttinger-liquid system. *Nat. Phys.* **8**, 174 (2012). doi: 10.1038/nphys2240 (cit. on p. 18).

70. F. J. Himpsel, K. N. Altmann, R. Bennewitz, J. N. Crain, *et al.* One-dimensional electronic states at surfaces. *J. Phys. Condens. Matter* **13**, 11097–11113 (2001). doi: 10.1088/0953-8984/13/49/301 (cit. on p. 18).

71. J. Lander & J. Morrison. Surface reactions of silicon with aluminum and with indium. *Surf. Sci.* **2**, 553–565 (1964). doi: 10.1016/0039-6028(64)90099-8 (cit. on p. 18).

72. S. Chandola, K. Hinrichs, M. Gensch, N. Eßer, *et al.* Structure of Si(111)-In Nanowires Determined from the Mid-infrared Optical Response. *Phys. Rev. Lett.* **102**, 226805 (2009). doi: 10.1103/PhysRevLett.102.226805 (cit. on p. 18).

73. S. Wippermann & W. G. Schmidt. Entropy Explains Metal-Insulator Transition of the Si(111)-In Nanowire Array. *Phys. Rev. Lett.* **105**, 126102 (2010). doi: 10.1103/PhysRevLett.105.126102 (cit. on pp. 18, 64).

74. T. Frigge, B. Hafke, T. Witte, B. Krenzer, *et al.* Optically excited structural transition in atomic wires on surfaces at the quantum limit. *Nature* **544**, 207–211 (2017). doi: 10.1038/nature21432 (cit. on p. 18).

75. C. W. Nicholson, A. Lücke, W. G. Schmidt, M. Puppin, *et al.* Beyond the molecular movie: Dynamics of bands and bonds during a photoinduced phase transition. *Science* **362**, 821–825 (2018). doi: 10.1126/science.aar4183 (cit. on p. 18).

76. H. E. Bishop & J. C. Rivière. Segregation of gold to the silicon (111) surface observed by Auger emission spectroscopy and by LEED. *J. Phys. D Appl. Phys.* **2**, 1635–1642 (1969). doi: 10.1088/0022-3727/2/12/302 (cit. on pp. 18, 19).

77. H. Lipson & K. E. Singer. Disorder in a film of gold deposited on silicon: investigation by low-energy electron diffraction. *J. Phys. C* **7**, 12–14 (1974). doi: 10.1088/0022-3719/7/1/010 (cit. on pp. 18, 19).

78. G. L. Lay & J. Faurie. AES study of the very first stages of condensation of gold films on silicon (111) surfaces. *Surf. Sci.* **69**, 295–300 (1977). doi: 10.1016/0039-6028(77)90174-1 (cit. on pp. 18, 19).

79. S. C. Erwin. Self-Doping of Gold Chains on Silicon: A New Structural Model for Si(111)–(5 \times 2)–Au. *Phys. Rev. Lett.* **91**, 206101 (2003). doi: 10.1103/PhysRevLett.91.206101 (cit. on pp. 18, 19).

80. S. G. Kwon & M. H. Kang. Identification of the Au Coverage and Structure of the Au/Si(111)-(5 \times 2) Surface. *Phys. Rev. Lett.* **113**, 086101 (2014). doi: 10.1103/PhysRevLett.113.086101 (cit. on pp. 18, 19, 21, 56).

81. J. Kuntze, A. Mugarza & J. E. Ortega. Ag-induced zero- and one-dimensional nanostructures on vicinal Si(111). *Appl. Phys. Lett.* **81**, 2463–2465 (2002). doi: 10.1063/1.1509857 (cit. on p. 18).

82. J. N. Crain, M. C. Gallagher, J. L. McChesney, M. Bissen & F. J. Himpsel. Doping of a surface band on Si(111) $\sqrt{3} \times \sqrt{3}$ –Ag. *Phys. Rev. B* **72**, 045312 (2005). doi: 10.1103/PhysRevB.72.045312 (cit. on p. 18).

83. U. Krieg, C. Brand, C. Tegenkamp & H. Pfñür. One-dimensional collective excitations in Ag atomic wires grown on Si(557). *J. Phys. Condens. Matter* **25**, 014013 (2012). doi: 10.1088/0953-8984/25/1/014013 (cit. on p. 18).

84. C. Tegenkamp, Z. Kallassy, H. Pfñür, H.-L. Günter, *et al.* Switching Between One and Two Dimensions: Conductivity of Pb-Induced Chain Structures on Si(557). *Phys. Rev. Lett.* **95**, 176804 (2005). doi: 10.1103/PhysRevLett.95.176804 (cit. on p. 18).

85. D. A. Ricci, T. Miller & T.-C. Chiang. Chemical Tuning of Metal-Semiconductor Interfaces. *Phys. Rev. Lett.* **93**, 136801 (2004). doi: 10.1103/PhysRevLett.93.136801 (cit. on p. 18).

86. D. Petrovykh, K. Altmann, J.-L. Lin, F. Himpsel & F. Leibsle. Single domain Ca-induced reconstruction on vicinal Si(111). *Surf. Sci.* **512**, 269–280 (2002). doi: 10.1016/S0039-6028(02)01693-X (cit. on p. 18).

87. A. Kirakosian, J. McChesney, R. Bennewitz, J. Crain, *et al.* One-dimensional Gd-induced chain structures on Si(111) surfaces. *Surf. Sci.* **498**, L109–L112 (2002). doi: 10.1016/S0039-6028(01)01806-4 (cit. on p. 18).

88. M. Dähne & M. Wanke. Metallic rare-earth silicide nanowires on silicon surfaces. *J. Phys. Condens. Matter* **25**, 14012–14021 (2013). doi: 10.1088/0953-8984/25/1/014012 (cit. on p. 18).

89. K. Holtgrewe, S. Appelfeller, M. Franz, M. Dähne & S. Sanna. Structure and one-dimensional metallicity of rare-earth silicide nanowires on Si(001). *Phys. Rev. B* **99**, 214104 (2019). doi: 10.1103/PhysRevB.99.214104 (cit. on p. 18).
90. J. Dabrowski & H. Müssig. Silicon Surfaces and Formation of Interfaces: Basic Science in the Industrial World (World Scientific, River Edge, N.J., 2000). doi: 10.1063/1.1420562. (Cit. on p. 18).
91. U. Memmert & M. L. Yu. Comparison between Si(100) and Si(111) in the reaction with oxygen at high temperatures. *Surf. Sci. Lett.* **245**, L185–L189 (1991). doi: 10.1016/0167-2584(91)90766-K (cit. on p. 18).
92. U. Memmert & M. L. Yu. Influence of the 7×7-1×1 phase transition on the sticking of oxygen on Si(111). *Chem. Phys. Lett.* **164**, 552–556 (1989). doi: 10.1016/0009-2614(89)85256-X (cit. on p. 18).
93. N. Stolwijk, B. Schuster, J. Hözl, H. Mehrer & W. Frank. Diffusion and solubility of gold in silicon. *Physica B+C* **116**, 335–342 (1983). doi: 10.1016/0378-4363(83)90271-1 (cit. on p. 19).
94. H. Okamoto & T. B. Massalski. The Au-Si (Gold-Silicon) system. *Bulletin of Alloy Phase Diagrams* **4**, 190–198 (1983). doi: 10.1007/bf02884878 (cit. on p. 19).
95. S. C. Erwin & H. H. Weitering. Theory of the “Honeycomb Chain-Channel” Reconstruction of M/Si(111)-(3×1). *Phys. Rev. Lett.* **81**, 2296–2299 (1998). doi: 10.1103/PhysRevLett.81.2296 (cit. on p. 19).
96. C. Battaglia, P. Aebi & S. C. Erwin. Stability and structure of atomic chains on Si(111). *Phys. Rev. B* **78**, 075409 (2008). doi: 10.1103/PhysRevB.78.075409 (cit. on p. 19).
97. L. Lottermoser, E. Landemark, D.-M. Smilgies, M. Nielsen, *et al.* New Bonding Configuration on Si(111) and Ge(111) Surfaces Induced by the Adsorption of Alkali Metals. *Phys. Rev. Lett.* **80**, 3980–3983 (1998). doi: 10.1103/PhysRevLett.80.3980 (cit. on p. 19).
98. C. Collazo-Davila, D. Grozea & L. D. Marks. Determination and Refinement of the Ag/Si(111)-(3×1) Surface Structure. *Phys. Rev. Lett.* **80**, 1678–1681 (1998). doi: 10.1103/PhysRevLett.80.1678 (cit. on p. 19).
99. A. A. Baski, J. Nogami & C. F. Quate. Si(111)-5×1-Au reconstruction as studied by scanning tunneling microscopy. *Phys. Rev. B* **41**, 10247–10249 (1990). doi: 10.1103/PhysRevB.41.10247 (cit. on p. 19).
100. J. D. O’Mahony, J. F. McGilp, C. F. J. Flipse, P. Weightman & F. M. Leibsle. Nucleation and evolution of the Au-induced 5×2 structure on vicinal Si(111). *Phys. Rev. B* **49**, 2527–2535 (1994). doi: 10.1103/PhysRevB.49.2527 (cit. on p. 19).
101. N. Osakabe, Y. Tanishiro, K. Yagi & G. Honjo. Reflection electron microscopy of clean and gold deposited (111) silicon surfaces. *Surf. Sci.* **97**, 393–408 (1980). doi: 10.1016/0039-6028(80)90675-5 (cit. on p. 19).
102. J. O’Mahony, C. Patterson, J. McGilp, F. Leibsle, *et al.* The Au-induced 5×2 reconstruction on Si(111). *Surf. Sci.* **277**, L57–L62 (1992). doi: 10.1016/0039-6028(92)90606-7 (cit. on p. 19).
103. J. Aulbach, S. C. Erwin, R. Claessen & J. Schäfer. Spin Chains and Electron Transfer at Stepped Silicon Surfaces. *Nano Lett.* **16**, 2698 (2016). doi: 10.1021/acs.nanolett.6b00354 (cit. on pp. 19, 22, 62, 72, 77).
104. Y. Okada & Y. Tokumaru. Precise determination of lattice parameter and thermal expansion coefficient of silicon between 300 and 1500 K. *J. Appl. Phys.* **56**, 314–320 (1984). doi: 10.1063/1.333965 (cit. on p. 19).
105. L. Pedri, L. Toppozini & M. C. Gallagher. Au-induced nanofaceting and the stoichiometry of the Si(775)-Au surface. *Surf. Sci.* **601**, 924–930 (2007). doi: 10.1016/j.susc.2006.11.031 (cit. on pp. 20, 21).
106. S. Riikonen & D. Sánchez-Portal. Structural models for Si(553)-Au atomic chain reconstruction. *Nanotechnology* **16**, S218 (2005). doi: 10.1088/0957-4484/16/5/015 (cit. on pp. 20, 23).
107. M. Krawiec. Spin-orbit splitting in the Si(335)-Au surface. *Surf. Sci.* **609**, 44–47 (2013). doi: 10.1016/j.susc.2012.1.0024 (cit. on p. 21).
108. C. Braun, C. Hogan, S. Chandola, N. Esser, *et al.* Si(775)-Au atomic chains: Geometry, optical properties, and spin order. *Phys. Rev. Materials* **1**, 055002 (2017). doi: 10.1103/PhysRevMaterials.1.055002 (cit. on pp. 21, 48, 52, 53).
109. S. C. Erwin & P. C. Snijders. Silicon spin chains at finite temperature: Dynamics of Si(553)-Au. *Phys. Rev. B* **87**, 235316 (2013). doi: 10.1103/PhysRevB.87.235316 (cit. on pp. 22, 28, 31).
110. J. N. Crain, A. Kirakosian, K. N. Altmann, C. Bromberger, *et al.* Fractional Band Filling in an Atomic Chain Structure. *Phys. Rev. Lett.* **90**, 176805 (2003). doi: 10.1103/PhysRevLett.90.176805 (cit. on pp. 21–23, 29, 34).

BIBLIOGRAPHY

111. I. Barke, F. Zheng, S. Bockenhauer, K. Sell, *et al.* Coverage-dependent faceting of Au chains on Si(557). *Phys. Rev. B* **79**, 155301 (2009). doi: 10.1103/PhysRevB.79.155301 (cit. on pp. 21–23).
112. J. R. Ahn, P. G. Kang, K. D. Ryang & H. W. Yeom. Coexistence of two different peierls distortions within an atomic scale wire: Si (553)-Au. *Phys. Rev. Lett.* **95**, 196402 (2005). doi: 10.1103/PhysRevLett.95.196402 (cit. on pp. 22, 23, 25, 26, 28–30, 63).
113. P. C. Snijders, S. Rogge & H. H. Weitering. Competing periodicities in fractionally filled one-dimensional bands. *Phys. Rev. Lett.* **96**, 076801 (2006). doi: 10.1103/PhysRevLett.96.076801 (cit. on pp. 22, 23, 26–31, 35, 36, 55, 63, 77).
114. K. D. Ryang, P. G. Kang, H. W. Yeom & S. Jeong. Structures and defects of atomic wires on Si(553)-Au: An STM and theoretical study. *Phys. Rev. B* **76**, 205325 (2007). doi: 10.1103/PhysRevB.76.205325 (cit. on pp. 22, 23).
115. P. G. Kang, J. S. Shin & H. W. Yeom. Point defects along metallic atomic wires on vicinal Si surfaces: Si(5 5 7)-Au and Si(5 5 3)-Au. *Surf. Sci.* **603**, 2588–2593 (2009). doi: 10.1016/j.susc.2009.06.012 (cit. on pp. 22, 35, 44, 77).
116. J. S. Shin, K.-D. Ryang & H. W. Yeom. Finite-length charge-density waves on terminated atomic wires. *Phys. Rev. B* **85**, 073401 (2012). doi: 10.1103/physrevb.85.073401 (cit. on p. 22).
117. J. Aulbach, J. Schäfer, S. C. Erwin, S. Meyer, *et al.* Evidence for Long-Range Spin Order Instead of a Peierls Transition in Si(553)-Au Chains. *Phys. Rev. Lett.* **111**, 137203 (2013). doi: 10.1103/PhysRevLett.111.137203 (cit. on pp. 22, 27, 29, 30).
118. S. Polei, P. C. Snijders, S. C. Erwin, F. J. Himpsel, *et al.* Structural Transition in Atomic Chains Driven by Transient Doping. *Phys. Rev. Lett.* **111**, 156801 (2013). doi: 10.1103/PhysRevLett.111.156801 (cit. on pp. 22, 23, 31).
119. S. Polei, P. C. Snijders, K. H. Meiwes-Broer & I. Barke. Current-Dependent Periodicities of Si(553)-Au. *Phys. Rev. B* **89**, 205420 (2014). doi: 10.1103/PhysRevB.89.205420 (cit. on pp. 22, 23, 31).
120. B. Hafke, T. Frigge, T. Witte, B. Krenzer, *et al.* Two-dimensional interaction of spin chains in the Si(553)-Au nanowire system. *Phys. Rev. B* **94**, 161403 (2016). doi: 10.1103/PhysRevB.94.161403 (cit. on pp. 22–24, 29, 55, 58, 71).
121. J. Aulbach, S. C. Erwin, J. Kemmer, M. Bode, *et al.* Parity breaking in a double atomic chain system. *Phys. Rev. B* **96**, 081406 (2017). doi: 10.1103/PhysRevB.96.081406 (cit. on pp. 22, 23, 29, 30, 61).
122. J. N. Crain & D. T. Pierce. End states in one-dimensional atom chains. *Science* **307**, 703–706 (2005). doi: 10.1126/science.1106911 (cit. on pp. 22, 27, 35).
123. J. N. Crain, M. D. Stiles, J. A. Stroscio & D. T. Pierce. Electronic effects in the length distribution of atom chains. *Phys. Rev. Lett.* **96**, 156801 (2006). doi: 10.1103/PhysRevLett.96.156801 (cit. on pp. 22, 27).
124. F. Edler, I. Miccoli, H. Pfnür & C. Tegenkamp. Charge-transfer transition in Au-induced quantum wires on Si(553). *Phys. Rev. B* **100**, 045419 (2019). doi: 10.1103/PhysRevB.100.045419 (cit. on pp. 22, 27, 28, 30, 31, 55, 63, 64, 68, 73, 74).
125. H. W. Yeom, K. S. Kim, J. Kim, S. W. Jung, *et al.* Direct observation of the spin polarization in Au atomic wires on Si(553). *New J. Phys.* **16**, 093030 (2014). doi: 10.1088/1367-2630/16/9/093030 (cit. on pp. 23, 26).
126. M. Krawiec. Structural model of the Au-induced Si(553) surface: Double Au rows. *Phys. Rev. B* **81**, 115436 (2010). doi: 10.1103/PhysRevB.81.115436 (cit. on pp. 23, 24, 30, 55, 56).
127. S. K. Ghose, I. K. Robinson, P. A. Bennett & F. J. Himpsel. Structure of double row quantum wires in Au/Si(5 5 3). *Surf. Sci.* **581**, 199–206 (2005). doi: 10.1016/j.susc.2005.02.053 (cit. on pp. 23, 55).
128. E. H. Do, S. G. Kwon, M. H. Kang & H. W. Yeom. Structural and electronic effects of adatoms on metallic atomic chains in Si(111)5 × 2-Au. *Sci. Rep.* **8**, 15537 (2018). doi: 10.1038/s41598-018-33703-5 (cit. on p. 23).
129. S. Riikonen & D. Sánchez-Portal. Ab initio study of the double row model of the Si(553)–Au reconstruction. *Surf. Sci.* **600**, 1201–1206 (2006). doi: 10.1016/j.susc.2005.12.043 (cit. on p. 23).
130. I. Song, J. S. Goh, S.-H. Lee, S. W. Jung, *et al.* Realization of a Strained Atomic Wire Superlattice. *ACS Nano* **9**, 10621–10627 (2015). doi: 10.1021/acsnano.5b04377 (cit. on p. 24).
131. S. Sanna, T. Lichtenstein, Z. Mamiyev, C. Tegenkamp & H. Pfnür. How One-Dimensional Are Atomic Gold Chains on a Substrate? *J. Phys. Chem. C* **122**, 25580–25588 (2018). doi: 10.1021/acs.jpcc.8b08600 (cit. on pp. 26, 28).
132. D. Sánchez-Portal, S. Riikonen & R. M. Martin. Role of Spin-Orbit Splitting and Dynamical Fluctuations in the Si(557)-Au Surface. *Phys. Rev. Lett.* **93**, 146803 (2004). doi: 10.1103/PhysRevLett.93.146803 (cit. on pp. 26, 34).

133. S. Riikonen & D. Sánchez-Portal. Systematic investigation of the structure of the Si(553)-Au surface from first principles. *Phys. Rev. B* **77**, 165418 (2008). doi: 10.1103/PhysRevB.77.165418 (cit. on p. 26).
134. I. Barke, F. Zheng, T. K. Rügheimer & F. J. Himpsel. Experimental evidence for spin-split bands in a one-dimensional chain structure. *Phys. Rev. Lett.* **97**, 226405 (2006). doi: 10.1103/PhysRevLett.97.226405 (cit. on pp. 26, 30, 34).
135. R. E. Peierls. *Bird of Passage: Recollections of a Physicist* (Princeton University Press, Princeton, NJ, 1985). doi: 10.1515/9781400854615. (Cit. on p. 26).
136. Y. A. Bychkov & E. I. Rashba. Properties of a 2D electron gas with lifted spectral degeneracy. *JETP Lett.* **39**, 78–81 (1984) (cit. on p. 26).
137. M. Krawiec, M. Kopciuszyński & R. Zdyb. Different spin textures in one-dimensional electronic bands on Si(553)-Au surface. *Appl. Surf. Sci.* **373**, 26–31 (2016). doi: 10.1016/j.apsusc.2015.09.219 (cit. on p. 26).
138. I. Song, D. H. Oh, H. C. Shin, S. J. Ahn, *et al.* Direct momentum-resolved observation of one-dimensional confinement of externally doped electrons within a single subnanometer-scale wire. *Nano Lett.* **15**, 281–288 (2015). doi: 10.1021/nl503558g (cit. on pp. 27, 28).
139. H. Okino, I. Matsuda, R. Hobara, S. Hasegawa, *et al.* Influence of defects on transport in quasi-one-dimensional arrays of chains of metal atoms on silicon. *Phys. Rev. B* **76**, 195418 (2007). doi: 10.1103/PhysRevB.76.195418 (cit. on pp. 27, 28, 35, 38).
140. C. E. Leal, I. C. da Cunha Lima, E. A. de Andrada e Silva & A. Troper. Electron mobility in quasi-one-dimensional conductors: A theoretical study. *Phys. Rev. B* **38**, 3525–3528 (1988). doi: 10.1103/PhysRevB.38.3525 (cit. on pp. 28, 31).
141. T. Lichtenstein, C. Tegenkamp & H. Pfnür. Lateral electronic screening in quasi-one-dimensional plasmons. *J. Phys. Condens. Matter* **28**, 354001 (2016). doi: 10.1088/0953-8984/28/35/354001 (cit. on pp. 28, 30).
142. Z. Mamiyev, S. Sanna, T. Lichtenstein, C. Tegenkamp & H. Pfnür. Extrinsic doping on the atomic scale: Tuning metallicity in atomic Au chains. *Phys. Rev. B* **98**, 245414 (2018). doi: 10.1103/PhysRevB.98.245414 (cit. on pp. 28, 70, 77).
143. F. Hötzl, N. Galde, S. Baur & A. Pucci. One-Dimensional Plasmonic Excitations in Gold-Induced Superstructures on Si(553): Impact of Gold Coverage and Silicon Step Edge Polarization. *J. Phys. Chem. C* **121**, 8120–8127 (2017). doi: 10.1021/acs.jpcc.6b11753 (cit. on pp. 28, 30).
144. P. Drude. Zur Elektronentheorie der Metalle. *Ann. Phys.* **306**, 566–613 (1900). doi: 10.1002/andp.19003060312 (cit. on pp. 28, 47).
145. P. C. Snijders, P. S. Johnson, N. P. Guisinger, S. C. Erwin & F. J. Himpsel. Spectroscopic evidence for spin-polarized edge states in graphitic Si nanowires. *New J. Phys.* **14**, 103004 (2012). doi: 10.1088/1367-2630/14/10/103004 (cit. on pp. 28–30).
146. K. Biedermann, S. Regensburger, T. Fauster, F. J. Himpsel & S. C. Erwin. Spin-split silicon states at step edges of Si(553)-Au. *Phys. Rev. B* **85**, 245413 (2012). doi: 10.1103/PhysRevB.85.245413 (cit. on pp. 29, 59, 60).
147. E. Madelung. Das elektrische Feld in Systemen von regelmäßig angeordneten Punktladungen. *Physikalische Zeitschrift* **19**, 524–533 (1919) (cit. on p. 29).
148. H. Okino, I. Matsuda, T. Tanikawa & S. Hasegawa. Formation of Facet Structures by Au Adsorption on Vicinal Si(111) Surfaces. *e-J. Surf. Sci. Nanotechnol.* **1**, 84–90 (2003). doi: 10.1380/ejssnt.2003.84 (cit. on p. 30).
149. I. Waller. Zur Frage der Einwirkung der Wärmebewegung auf die Interferenz von Röntgenstrahlen. *Zeitschrift für Physik* **17**, 398–408 (1923). doi: 10.1007/bf01328696 (cit. on pp. 31, 32, 73).
150. B. Hafke, C. Brand, T. Witte, B. Sothmann, *et al.* Thermally Induced Crossover from 2D to 1D Behavior in an Array of Atomic Wires: Silicon Dangling-Bond Solitons in Si(553)-Au. *Phys. Rev. Lett.* **124**, 016102 (2020). doi: 10.1103/PhysRevLett.124.016102 (cit. on pp. 31, 70, 77).
151. B. Hafke. Untersuchung und Manipulation der Dynamik des Soliton-induzierten Ordnungs-Unordnungs-Übergangs im Si(553)-Au Atomdrahtsystem. PhD thesis (Universität Duisburg-Essen, 2019). doi: 10.17185/duepublico/70700 (cit. on pp. 31, 73, 74, 77).
152. R. B. Potts. Some generalized order-disorder transformations. *Math. Proc. Cambridge Philos. Soc.* **48**, 106–109 (1952). doi: 10.1017/s0305004100027419 (cit. on p. 31).

BIBLIOGRAPHY

153. J. R. Ahn, H. W. Yeom, H. S. Yoon & I.-W. Lyo. Metal-Insulator Transition in Au Atomic Chains on Si with Two Proximal Bands. *Phys. Rev. Lett.* **91**, 196403 (2003). doi: 10.1103/PhysRevLett.91.196403 (cit. on pp. 32–34).
154. H. W. Yeom, J. R. Ahn, H. S. Yoon, I. W. Lyo, *et al.* Real-space investigation of the metal-insulator transition of Si(557)-Au. *Phys. Rev. B* **72**, 035323 (2005). doi: 10.1103/PhysRevB.72.035323 (cit. on pp. 32, 34).
155. M. Krawiec, T. Kwapiński & M. Jałochowski. Double nonequivalent chain structure on a vicinal Si(557)-Au surface. *Phys. Rev. B* **73**, 075415 (2006). doi: 10.1103/PhysRevB.73.075415 (cit. on p. 32).
156. I. K. Robinson, P. A. Bennett & F. J. Himpsel. Structure of Quantum Wires in Au/Si(557). *Phys. Rev. Lett.* **88**, 096104 (2002). doi: 10.1103/PhysRevLett.88.096104 (cit. on p. 32).
157. D. Sánchez-Portal, J. D. Gale, A. García & R. M. Martin. Two distinct metallic bands associated with monatomic Au wires on the Si(557)-Au surface. *Phys. Rev. B* **65**, 081401(R) (2002). doi: 10.1103/PhysRevB.65.081401 (cit. on pp. 32, 34).
158. J. Voit. Charge-spin separation and the spectral properties of Luttinger liquids. *Phys. Rev. B* **47**, 6740–6743 (1993). doi: 10.1103/PhysRevB.47.6740 (cit. on p. 33).
159. T. Nagao, S. Yaginuma, T. Inaoka & T. Sakurai. One-Dimensional Plasmon in an Atomic-Scale Metal Wire. *Phys. Rev. Lett.* **97**, 116802 (2006). doi: 10.1103/PhysRevLett.97.116802 (cit. on pp. 33, 34).
160. S. Riikonen & D. Sánchez-Portal. Interplay between electronic and atomic structures in the Si(557)-Au reconstruction from first principles. *Phys. Rev. B* **76**, 035410 (2007). doi: 10.1103/PhysRevB.76.035410 (cit. on p. 34).
161. H. Okino, R. Hobara, I. Matsuda, T. Kanagawa, *et al.* Nonmetallic transport of a quasi-one-dimensional metallic Si(557)-Ausurface. *Phys. Rev. B* **70**, 113404 (2004). doi: 10.1103/physrevb.70.113404 (cit. on p. 35).
162. J. N. Crain & F. J. Himpsel. Low-dimensional electronic states at silicon surfaces. *Appl. Phys. A* **82**, 431–438 (2006). doi: 10.1007/s00339-005-3365-3 (cit. on p. 35).
163. G. Lee, S.-Y. Yu, H. Shim, W. Lee & J.-Y. Koo. Roles of defects induced by hydrogen and oxygen on the structural phase transition of Si(111)4×1-In. *Phys. Rev. B* **80**, 075411 (2009). doi: 10.1103/physrevb.80.075411 (cit. on p. 35).
164. T. Shibusaki, N. Nagamura, T. Hirahara & H. Okino. Phase transition temperatures determined by different experimental methods: Si (111) 4×1-In surface with defects. *Phys. Rev. B* **81**, 035314 (2010). doi: 10.1103/PhysRevB.81.035314 (cit. on p. 35).
165. S.-W. Kim & J.-H. Cho. Origin of the metal-insulator transition of indium atom wires on Si(111). *Phys. Rev. B* **93**, 241408(R) (2016). doi: 10.1103/physrevb.93.241408 (cit. on p. 35).
166. H. W. Yeom, D. M. Oh, S. Wippermann & W. G. Schmidt. Impurity-Mediated Early Condensation of a Charge Density Wave in an Atomic Wire Array. *ACS Nano* **10**, 810–814 (2016). doi: 10.1021/acsnano.5b05925 (cit. on p. 35).
167. Z. Mamiyev, T. Lichtenstein, C. Tegenkamp, C. Braun, *et al.* Plasmon spectroscopy: Robust metallicity of Au wires on Si(557) upon oxidation. *Phys. Rev. Materials* **2**, 66002 (2018). doi: 10.1103/PhysRevMaterials.2.066002 (cit. on p. 36, 46, 49–51).
168. F. Edler, C. Braun, S. Neufeld, S. Sanna, *et al.* Tuning the conductivity along atomic chains by selective chemisorption. *Phys. Rev. B* **95**, 125409 (2017). doi: 10.1103/physrevb.95.125409 (cit. on pp. 36–39, 43, 45).
169. I. Miccoli, F. Edler, H. Pfnür & C. Tegenkamp. The 100th anniversary of the four-point probe technique: the role of probe geometries in isotropic and anisotropic systems. *J. Phys. Condens. Matter* **27**, 223201 (2015). doi: 10.1088/0953-8984/27/22/223201 (cit. on p. 38).
170. T. Kanagawa, R. Hobara, I. Matsuda, T. Tanikawa, *et al.* Anisotropy in Conductance of a Quasi-One-Dimensional Metallic Surface State Measured by a Square Micro-Four-Point Probe Method. *Phys. Rev. Lett.* **91**, 036805 (2003). doi: 10.1103/physrevlett.91.036805 (cit. on p. 38).
171. T. Tanikawa, I. Matsuda, T. Kanagawa & S. Hasegawa. Surface-State Electrical Conductivity at a Metal-Insulator Transition On Silicon. *Phys. Rev. Lett.* **93**, 016801 (2004). doi: 10.1103/physrevlett.93.016801 (cit. on p. 38).
172. F. Edler, I. Miccoli, S. Demuth, H. Pfnür, *et al.* Interwire coupling for In(4×1)/Si(111) probed by surface transport. *Phys. Rev. B* **92**, 085426 (2015). doi: 10.1103/physrevb.92.085426 (cit. on p. 39).
173. G. Kresse & J. Furthmüller. Efficient iterative schemes for *ab initio* total-energy calculations using a plane-wave basis set. *Phys. Rev.* **54**, 11169 (1996). doi: 10.1103/PhysRevB.54.11169 (cit. on p. 39).

174. P. E. Blöchl. Projector augmented-wave method. *Phys. Rev. B* **50**, 17953–17979 (1994). doi: 10.1103/PhysRevB.50.17953 (cit. on p. 39).

175. J. P. Perdew, K. Burke & M. Ernzerhof. Generalized Gradient Approximation Made Simple. *Phys. Rev. Lett.* **77**, 3865–3868 (1996). doi: 10.1103/PhysRevLett.77.3865 (cit. on p. 40).

176. Z. Mamiyev, M. Tzschoppe, C. Huck, A. Pucci & H. Pfür. Plasmon Standing Waves by Oxidation of Si(553)–Au. *J. Phys. Chem. C* **123**, 9400–9406 (2019). doi: 10.1021/acs.jpcc.9b01372 (cit. on p. 40).

177. C.-Y. Niu & J.-T. Wang. Adsorption and dissociation of oxygen molecules on Si(111)-(7×7) surface. *J. Chem. Phys.* **139**, 194709 (2013). doi: 10.1063/1.4832340 (cit. on pp. 40, 42).

178. P. V. C. Medeiros, S. Stafström & J. Björk. Effects of extrinsic and intrinsic perturbations on the electronic structure of graphene: Retaining an effective primitive cell band structure by band unfolding. *Phys. Rev. B* **89**, 041407 (2014). doi: 10.1103/PhysRevB.89.041407 (cit. on pp. 43, 60, 67).

179. J. P. Perdew. Density functional theory and the band gap problem. *Int. J. Quantum Chem.* **28**, 497–523 (1985). doi: 10.1002/qua.560280846 (cit. on p. 46).

180. T. Lichtenstein, Z. Mamiyev, C. Braun, S. Sanna, *et al.* Probing quasi-one-dimensional band structures by plasmon spectroscopy. *Phys. Rev. B* **97**, 165421 (2018). doi: 10.1103/PhysRevB.97.165421 (cit. on pp. 46–49, 53, 54).

181. S. Das Sarma & E. H. Hwang. Dynamical response of a one-dimensional quantum-wire electron system. *Phys. Rev. B* **54**, 1936–1946 (1996). doi: 10.1103/PhysRevB.54.1936 (cit. on pp. 46, 47).

182. R. K. Moudgil, V. Garg & K. N. Pathak. Confinement and correlation effects on plasmons in an atom-scale metallic wire. *J. Phys. Condens. Matter* **22**, 135003 (2010). doi: 10.1088/0953-8984/22/13/135003 (cit. on p. 46).

183. S. Das Sarma & W.-y. Lai. Screening and elementary excitations in narrow-channel semiconductor microstructures. *Phys. Rev. B* **32**, 1401–1404 (1985). doi: 10.1103/PhysRevB.32.1401 (cit. on p. 47).

184. Q. Li & S. Das Sarma. Plasmon excitations in one-dimensional lateral-quantum-wire superlattices. *Phys. Rev. B* **41**, 10268–10271 (1990). doi: 10.1103/PhysRevB.41.10268 (cit. on p. 47).

185. C. Braun. First Principles Investigation of Spin Ordering in Nanowires. MA thesis (Universität Paderborn, 2016) (cit. on p. 52).

186. J. Heyd, G. E. Scuseria & M. Ernzerhof. Hybrid functionals based on a screened Coulomb potential. *J. Chem. Phys.* **118**, 8207–8215 (2003). doi: 10.1063/1.1564060 (cit. on p. 53).

187. W. Voegeli, T. Takayama, T. Shirasawa, M. Abe, *et al.* Structure of the quasi-one-dimensional Si(553)-Au surface: Gold dimer row and silicon honeycomb chain. *Phys. Rev. B* **82**, 075426 (2010). doi: 10.1103/physrevb.82.075426 (cit. on pp. 55, 56).

188. C. Braun, U. Gerstmann & W. G. Schmidt. Spin pairing versus spin chains at Si(553)-Au surfaces. *Phys. Rev. B* **98**, 121402(R) (2018). doi: 10.1103/PhysRevB.98.121402 (cit. on pp. 55, 60–62, 70).

189. H. J. Monkhorst & J. D. Pack. Special points for Brillouin-zone integrations. *Phys. Rev. B* **13**, 5188–5192 (1976). doi: 10.1103/PhysRevB.13.5188 (cit. on p. 56).

190. J. P. Perdew, A. Ruzsinszky, G. I. Csonka, O. A. Vydrov, *et al.* Restoring the Density-Gradient Expansion for Exchange in Solids and Surfaces. *Phys. Rev. Lett.* **100**, 136406 (2008). doi: 10.1103/PhysRevLett.100.136406 (cit. on pp. 56, 59).

191. G.-X. Zhang, A. M. Reilly, A. Tkatchenko & M. Scheffler. Performance of various density-functional approximations for cohesive properties of 64 bulk solids. *New J. Phys.* **20**, 063020 (2018). doi: 10.1088/1367-2630/aac7f0 (cit. on p. 56).

192. C. Hogan, E. Speiser, S. Chandola, S. Suchkova, *et al.* Controlling the Local Electronic Properties of Si(553)-Au through Hydrogen Doping. *Phys. Rev. Lett.* **120**, 166801 (2018). doi: 10.1103/PhysRevLett.120.166801 (cit. on pp. 56, 57, 59, 77).

193. J. P. Perdew & A. Zunger. Self-interaction correction to density-functional approximations for many-electron systems. *Phys. Rev. B* **23**, 5048–5079 (1981). doi: 10.1103/PhysRevB.23.5048 (cit. on p. 59).

194. P. Broqvist, A. Alkauskas & A. Pasquarello. Defect levels of dangling bonds in silicon and germanium through hybrid functionals. *Phys. Rev. B* **78**, 075203 (2008). doi: 10.1103/PhysRevB.78.075203 (cit. on p. 59).

BIBLIOGRAPHY

195. V. Lubarda. On the effective lattice parameter of binary alloys. *Mech. Mater.* **35**, 53–68 (2003). doi: 10.1016/s0167-6636(02)00196-5 (cit. on p. 59).
196. A. A. Stekolnikov, K. Seino, F. Bechstedt, S. Wippermann, *et al.* Hexagon versus Trimer Formation in In Nanowires on Si(111): Energetics and Quantum Conductance. *Phys. Rev. Lett.* **98**, 026105 (2007). doi: 10.1103/PhysRevLett.98.026105 (cit. on p. 59).
197. J. Tersoff & D. R. Hamann. Theory and Application for the Scanning Tunneling Microscope. *Phys. Rev. Lett.* **50**, 1998–2001 (1983). doi: 10.1103/PhysRevLett.50.1998 (cit. on p. 61).
198. C. Braun, S. Neufeld, U. Gerstmann, S. Sanna, *et al.* Vibration-Driven Self-Doping of Dangling-Bond Wires on Si(553)-Au Surfaces. *Phys. Rev. Lett.* **124**, 146802 (2020). doi: 10.1103/PhysRevLett.124.146802 (cit. on pp. 63, 64, 67, 70, 73, 74).
199. W. G. Schmidt, S. Wippermann, S. Sanna, M. Babilon, *et al.* In-Si(111)(4×1)/(8×2) nanowires: Electron transport, entropy, and metal-insulator transition. *phys. stat. sol. (b)* **249**, 343–359 (2012). doi: 10.1002/pssb.201100457 (cit. on p. 64).
200. P. J. Brown, A. G. Fox, E. N. Maslen, M. A. O’Keefe & B. T. M. Willis. Intensity of diffracted intensities. in International Tables for Crystallography Volume C: Mathematical, physical and chemical tables (ed E. Prince) (Springer Netherlands, Dordrecht, 2004), pp. 554–595. doi: 10.1107/97809553602060000600 (cit. on pp. 73, 74).
201. J. R. Ahn, P. G. Kang, J. H. Byun & H. W. Yeom. Adsorbate-induced reconstruction of an array of atomic wires: Indium on the Si(553)-Au surface. *Phys. Rev. B* **77**, 035401 (2008). doi: 10.1103/PhysRevB.77.035401 (cit. on p. 77).
202. M. Tzschorpe, C. Huck, F. Hötzl & A. Pucci. C70 increases the plasmonic signal of gold-atom chains on Si(553). *Surf. Sci.* **678**, 32–37 (2018). doi: 10.1016/j.susc.2018.02.007 (cit. on p. 77).
203. S. Suchkova, C. Hogan, F. Bechstedt, E. Speiser & N. Esser. Selective adsorption of toluene-3,4-dithiol on Si(553)-Au surfaces. *Phys. Rev. B* **97**, 045417 (2018). doi: 10.1103/PhysRevB.97.045417 (cit. on p. 77).
204. M. Tzschorpe, C. Huck, F. Hötzl, B. Günther, *et al.* How adsorbates alter the metallic behavior of quasi-one-dimensional electron systems of the Si(553)-Au surface. *J. Phys. Condens. Matter* **31**, 195001 (2019). doi: 10.1088/1361-648X/ab0710 (cit. on p. 77).
205. C. Hogan, S. Suchkova, F. Bechstedt, E. Speiser, *et al.* Organic Molecule Adsorption on Stepped Si–Au Surfaces: Role of Functional Group on Geometry and Electronic Structure. *Phys. Status Solidi B* **256**, 1800653 (2019). doi: 10.1002/pssb.201800653 (cit. on p. 77).

List of Figures

2.1	The momentum distribution and spectral function for free and interacting electrons.	4
2.2	The nesting condition of Fermi surfaces and low-energetic e-h excitations in high-dimensional space and in 1D.	6
2.3	Band gap opening and CDW formation due to a Peierls instability.	8
3.1	Sidecut of the silicon crystal in the $[1\bar{1}0]$ plane showing the various $\text{Si}(hhk)$ surfaces.	20
3.2	Step-edge reconstructions and Au adsorption for step edges resulting from positive and negative cutting angles.	20
3.3	Atomic structures of $\text{Si}(335)\text{-Au}$ and $\text{Si}(775)\text{-Au}$ in top and side view.	21
3.4	Experimental STM and LEED images at several temperatures.	22
3.5	Historical development of the structural model of $\text{Si}(553)\text{-Au}$ in top and side view.	23
3.6	Structural model of the low-coverage wires of $\text{Si}(553)\text{-Au}$ in top and side view.	25
3.7	ARPES spectra of $\text{Si}(553)\text{-Au}$ at (b) 300 K and (c) 70 K.	25
3.8	Side and top view of the spin chain structure of $\text{Si}(557)\text{-Au}$	33
4.1	SPA-LEED patterns of $\text{Si}(553)\text{-Au}$ and $\text{Si}(557)\text{-Au}$ without and with an oxygen exposure of 20 L together with the structural models.	37
4.2	4PP setup used for transport measurements in square geometry and resulting $I\text{-}V$ curves together with the resistance obtained by the rotational square method.	38
4.3	Conductivity in the parallel and perpendicular direction with respect to the oxygen dose for $\text{Si}(553)\text{-Au}$ and $\text{Si}(557)\text{-Au}$	39
4.4	PES for the adsorption of O_2 molecules on $\text{Si}(557)\text{-Au}$ and $\text{Si}(553)\text{-Au}$	40
4.5	Atomic structure of the six most stable adsorption sites for a single O_2 molecule on $\text{Si}(557)\text{-Au}$	41
4.6	Atomic structure of the most stable adsorption sites for a single O_2 molecule on the $\text{Si}(553)\text{-Au}$ surface.	42
4.7	Atomic structure of the most stable adsorption sites for two O_2 molecules on $\text{Si}(557)\text{-Au}$	42
4.8	Band structures of clean and oxidized $\text{Si}(557)\text{-Au}$ and $\text{Si}(553)\text{-Au}$ surfaces.	43
4.9	The experimental and fitted resistivity of the $\text{Si}(557)\text{-Au}$ surface in the chain direction with respect to the oxygen dose.	45
4.10	Sample EEL spectra of $\text{Si}(335)\text{-Au}$ measured across and along the wires as well as the fitted plasmon dispersion compared with the e-h continuum within the confined NFEG model.	47
4.11	Plasmon dispersions of $\text{Si}(557)\text{-Au}$ and $\text{Si}(775)\text{-Au}$ with respect to k_{\parallel} compared to with the e-h continuum within the confined NFEG model.	48
4.12	EEL spectra of $\text{Si}(557)\text{-Au}$ with and without 7.5 L of oxygen together with a section of the surface bands along the wire direction with the overlayed derived dispersion of ω_+	49
4.13	Plasmon dispersion of the pristine and oxygen-adsorbed $\text{Si}(557)\text{-Au}$ surface for various O_2 doses.	50
4.14	Surface bands of two $\text{Si}(557)\text{-Au}$ surfaces as well as the upper limit of the e-h excitation continuum of the clean and oxidized surfaces.	51

4.15	Band structure of Si(775)-Au in the direction parallel to the wires for several set dimerizations.	52
4.16	Surface bands of Si(775)-Au shown with the upper limit of the e-h continuum ω_+	53
5.1	The Krawiec, spin-chain, and rehybridized model of Si(553)-Au.	56
5.2	Calculated surface energy and surface magnetization per (1×6) surface unit cell with respect to the reaction coordinate for PBEsol.	57
5.3	Electronic charge density difference between the SC and R surface and a schematic model for the parity breaking of the step edge.	58
5.4	Folded and unfolded band structure of Si(553)-Au for the R and SC model compared with ARPES data.	60
5.5	Comparison of experimental and simulated empty-state STM images of Si(553)-Au at different tunneling biases	61
6.1	Calculated PES for the $(2,2,0)$ to $(2,2,0_1)$ transition for two different dimerizations and an electron-doped surface.	64
6.2	Vibrational free-energy correction of $(2,2,0_1)$ subtracted by the correction of $(2,2,0)$ for several temperatures.	65
6.3	Surface bands in the direction parallel to the Au wires calculated along the reaction path from $(2,2,0)$ to $(2,2,0_1)$ for Si(553)-Au.	67
6.4	Relative change of the DOS of the $S_{1/2}$ and S_3 bands at the Fermi energy along the reaction path q compared to the $(2,2,0)$ ground state.	68
6.5	The temporal charge configuration according to the step-edge atoms' positions and the vertical distribution for several temperatures.	69
6.6	Influence of the dimerization on the energetic landscape and transition probability with changing temperature for Si(553)-Au.	70
6.7	Calculated average number of (unpaired) electrons per DB and the average magnetization compared to different magnetic configurations.	72
6.8	Section of temperature-dependent Raman spectra highlighting two Raman modes located at the step edge and the Au chain.	73
6.9	Experimental and simulated SPA-LEED patterns of Si(553)-Au side by side.	74
A.1	The AIMD simulation's velocity distribution compared to the Maxwell-Boltzmann distribution for several temperatures.	79
A.2	Distribution of the step-edge atoms' vertical positions calculated by AIMD for several temperatures.	80
A.3	Position along the reaction coordinate and magnetization of each of the six step-edge atoms for several temperatures from 50 K to 400 K.	81
A.4	Relative displacement of the twelve Au atoms with respect to the underlying Si bulk lattice constant for several temperatures.	82

List of Tables

3.1	The terrace width, Au coverage, and off-axis angle for several vicinal Si(111)-Au surfaces.	21
4.1	The energies and adsorption sites of the (meta-)stable configurations for a single O ₂ molecule on Si(553)-Au as well as a single and two O ₂ molecules on Si(557)-Au	41
5.1	Surface energies of the SC and R model with respect to the K model using different XC functionals.	58
5.2	Experimental lattice parameters of Si and Au bulk compared to the DFT lattice parameters calculated within LDA, PBE, and PBEsol.	59
6.1	The inverse effective masses of the $S_{1/2}$ and S_3 bands along the reaction path from (2,2,0) to (2,2,0 ₁).	66

LIST OF TABLES

List of Publications

Articles in Scientific Journals

C. Braun, S. Sanna & W. G. Schmidt. Liquid Crystal (8CB) Molecular Adsorption on Lithium Niobate Z-Cut Surfaces. *J. Phys. Chem. C* **119**, 9342 (2015). doi: 10.1021/acs.jpcc.5b00894

F. Edler, I. Miccoli, J. P. Stöckmann, H. Pfnür, C. Braun, S. Neufeld, S. Sanna, W. G. Schmidt & C. Tegenkamp. Tuning the conductivity along atomic chains by selective chemisorption. *Phys. Rev. B* **95**, 125409 (2017). doi: 10.1103/PhysRevB.95.125409

C. Braun, C. Hogan, S. Chandola, N. Esser, S. Sanna & W. G. Schmidt. Si(775)-Au atomic chains: Geometry, optical properties, and spin order. *Phys. Rev. Materials* **1**, 055002 (2017). doi: 10.1103/PhysRevMaterials.1.055002

T. Lichtenstein, Z. Mamiyev, C. Braun, S. Sanna, W. G. Schmidt, C. Tegenkamp & H. Pfnür. Probing quasi-one-dimensional band structures by plasmon spectroscopy. *Phys. Rev. B* **97**, 165421 (2018). doi: 10.1103/PhysRevB.97.165421

Z. Mamiyev, T. Lichtenstein, C. Tegenkamp, C. Braun, W. G. Schmidt, S. Sanna & H. Pfnür. Plasmon spectroscopy: Robust metallicity of Au wires on Si(557) upon oxidation. *Phys. Rev. Materials* **2**, 066002 (2018). doi: 10.1103/PhysRevMaterials.2.066002

C. Braun, U. Gerstmann & W. G. Schmidt. Spin pairing versus spin chains at Si(553)-Au surfaces. *Phys. Rev. B* **98**, 121402(R) (2018). doi: 10.1103/PhysRevB.98.121402

C. Braun, S. Neufeld, U. Gerstmann, S. Sanna, J. Plaickner, E. Speiser, N. Esser & W. G. Schmidt. Vibration-Driven Self-Doping of Dangling-Bond Wires on Si(553)-Au Surfaces. *Phys. Rev. Lett.* **124**, 146802 (2020). doi: 10.1103/PhysRevLett.124.146802

L. Meier, C. Braun, T. Hannappel & W. G. Schmidt. Band Alignment at $\text{Ga}_x\text{In}_{1-x}\text{P}/\text{Al}_y\text{In}_{1-y}\text{P}$ Alloy Interfaces from Hybrid Density Functional Theory Calculations. *Phys. Status Solidi B*, 146802 (2020). doi: 10.1002/pssb.202000463

J. Plaickner, E. Speiser, C. Braun, W. G. Schmidt, N. Esser & S. Sanna. Surface-localized phonon-modes at the Si(553)-Au nanowire system. *Submitted to Phys. Rev. B* (2021).

Other Scientific Publications

S. Sanna, U. Gerstmann, E. Rauls, Y. Li, M. Landmann, A. Riefer, M. Rohrmüller, N. J. Vollmers, M. Witte, R. Hölscher, A. Lücke, C. Braun, S. Neufeld, K. Holtgrewe & W.G. Schmidt. Surface Charge of Clean LiNbO_3 Z-Cut Surfaces. *High Performance Computing in Science and Engineering '14*. Springer, Cham, 163 (2015). doi: 10.1007/978-3-319-10810-0_12

A. Lücke, U. Gerstmann, S. Sanna, M. Landmann, A. Riefer, M. Rohrmüller, N. J. Vollmers, M. Witte, E. Rauls, R. Hölscher, C. Braun, S. Neufeld, K. Holtgrewe & W. G. Schmidt. Solving the Scattering Problem for the P3HT On-Chain Charge Transport. In: Nagel W., Kröner D., Resch M. (eds) *High Performance Computing in Science and Engineering '15*. Springer, Cham, 155 (2016). doi: 10.1007/978-3-319-24633-8_10

S. Sanna, C. Dues, U. Gerstmann, E. Rauls, D. Nozaki, A. Riefer, M. Landmann, M. Rohrmüller, N. J. Vollmers, R. Hölscher, A. Lücke, C. Braun, S. Neufeld, K. Holtgrewe & W. G. Schmidt. Submonolayer Rare Earth Silicide Thin Films on the Si(111) Surface. In: Nagel W., Kröner D., Resch M. (eds) *High Performance Computing in Science and Engineering '16*. Springer, Cham, 163 (2017). doi: 10.1007/978-3-319-47066-5_12

A. Lücke, T. Biktagirov, A. Riefer, M. Landmann, M. Rohrmüller, C. Braun, S. Neufeld, U. Gerstmann & W. G. Schmidt. Photo-Excited Surface Dynamics from Massively Parallel Constrained-DFT Calculations. In: Nagel W., Kröner D., Resch M. (eds) *High Performance Computing in Science and Engineering '17*. Springer, Cham, 157 (2018). doi: 10.1007/978-3-319-68394-2_9

T. Biktagirov, C. Braun, S. Neufeld, U. Gerstmann & W. G. Schmidt. Accurate and Efficient Spin-Spin Zero-Field Splitting Calculations for Extended Periodic Systems. In: Nagel W., Kröner D., Resch M. (eds) *High Performance Computing in Science and Engineering '18*. Springer, Cham, 131 (2019). doi: 10.1007/978-3-030-13325-2_8

Hiermit erkläre ich, Christian Braun, geboren am 20.02.1991 in Lemgo, dass ich die vorliegende Dissertation selbstständig und nur unter Verwendung der angegebenen Quellen und Hilfsmittel verfasst, alle Stellen der Arbeit, die wörtlich oder sinngemäß aus anderen Quellen übernommen worden sind, als solche kenntlich gemacht und diese Arbeit in gleicher oder ähnlicher Form noch keiner Prüfungsbehörde vorgelegt habe.

(Christian Braun)
Paderborn, 10.02.2021

